# ACCELERATOR PHYSICS AND INSTRUMENTATION

# COMPLETION OF THE S800 SPECTROGRAPH

A. Zeller, D. Bazin, S. Bricker, J. Caggiano, B. Davids, A. Dunn, J. DeKamp, B. Drewyor, P. Fighter, R. Fontus, R. Fox, D. Harris, H. Hilbert, P. Johnson, H. Laumer, L. Morris, W. Nurnberger, D. Pendell, J. Priller, D. Sanderson, D. Scott, B. Sherrill, M. Steiner, J. Stetson, D. Swan, R. Swanson, John Vincent, J. Wagner, R. Welton, J. Yurkon, B. Zhang and R. Zink

## Beamline

The last two dipoles were put in place and aligned. Then the last two triplets were installed and the cryogenic connections made for the remaining elements. Several nitrogen and helium leaks were discovered and either repaired or pumps installed to handle the loads. None of the remaining leaks are too big for the pumps to handle. Where necessary, additional vacuum breaks were placed to keep the leaks from affecting the adjacent elements. Power supplies were installed on the middle level of the fixed platform and connected to the magnets. The magnets were then aligned magnetically to the beam axis and the transfer functions of the individual magnets measured. Cryogenic Hall chips that were placed on one pole tip in each quad were calibrated and can be used to give an exact gradient setting.

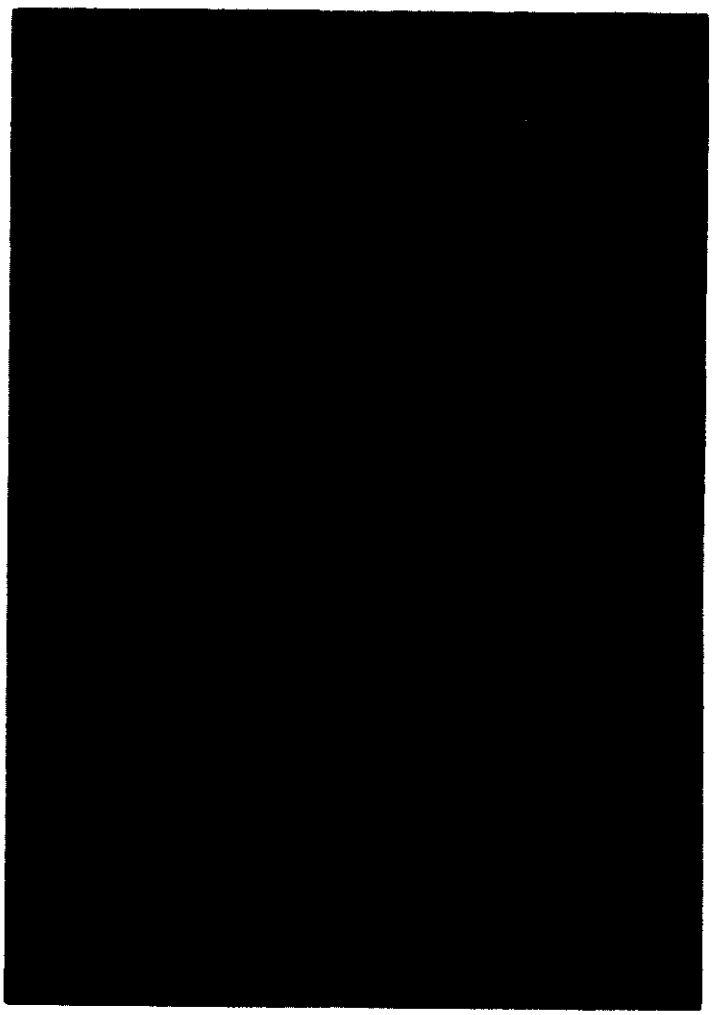

Figure 1: A section of the beamline going down the stairs is seen. This is at the middle level on the fixed platform and also shows the power supply area.

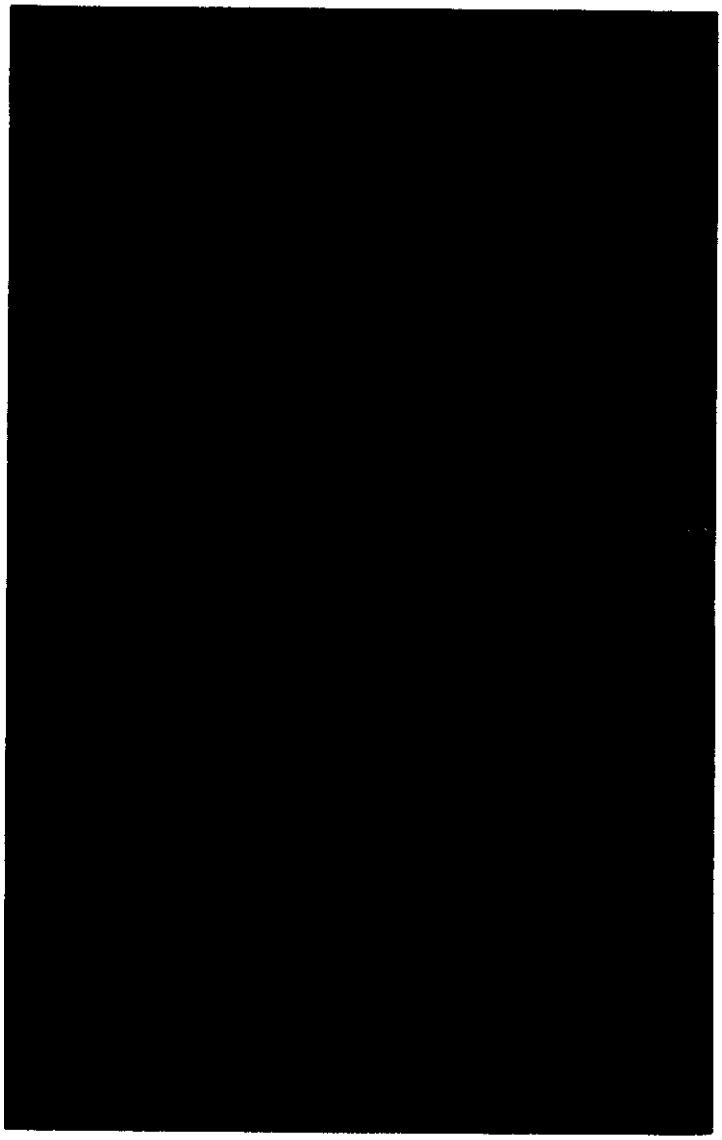

Figure 2: The Q1/Q2 doublet in place on the carriage.

The high resolution location target drive, the production target chamber and the intermediate image chamber were installed, along with the beam pipe. Vacuum systems were then added and the line placed under vacuum. A section of the beamline going down the stairs and the power supply area are shown in Fig. 1. The elements are filled with liquid helium once a day. The heat load, including losses in the transfer line during filling, is the equivalent of 23 l/hr of liquid helium. This is close to our estimate of 25 l/hr.

Initial beam tests were done with a blank off at the end of the last triplet in June. A scintillator was placed on the transparent blank off and beam tuned to it. The optics were compared with the TRANSPORT calculations and found to be in reasonable agreement.

**Spectrometer dipoles and quads**

The cryogenic connections to the carriage required more than four months of effort, but was completed without a single leak. The modification to the D2 bobbin to accommodate the helium leak

resulted in no helium leaking into the insulation vacuum. The added "bumpers", designed to prevent any hard contact between the nitrogen shield and the helium temperature surfaces, resulted in the heat load on the helium a factor of two less than D1's. The Q1/Q2 heat load was measured off-line and the total heat load (as determined from total helium consumption) for the entire system determined. The heat loads are shown in Table 1.

| Device | Heat load at 4 K (W) |
|---|---|
| D1 (good vacuum) | 12 |
| D2 | 5.5 |
| Q1/Q2 | 2 |
| Transfer lines | 78 |

Table 1. S800 Heat Loads

The largest load, the transfer lines, occurs mainly because it is necessary to have flexible lines so the spectrometer can be rotated. These lines are not as well shielded as the rest of the lines because it was necessary to keep the line diameter small enough so the minimum bending radius would allow the lines to fit on the carriage. Therefore, the space for superinsulation was greatly reduced.

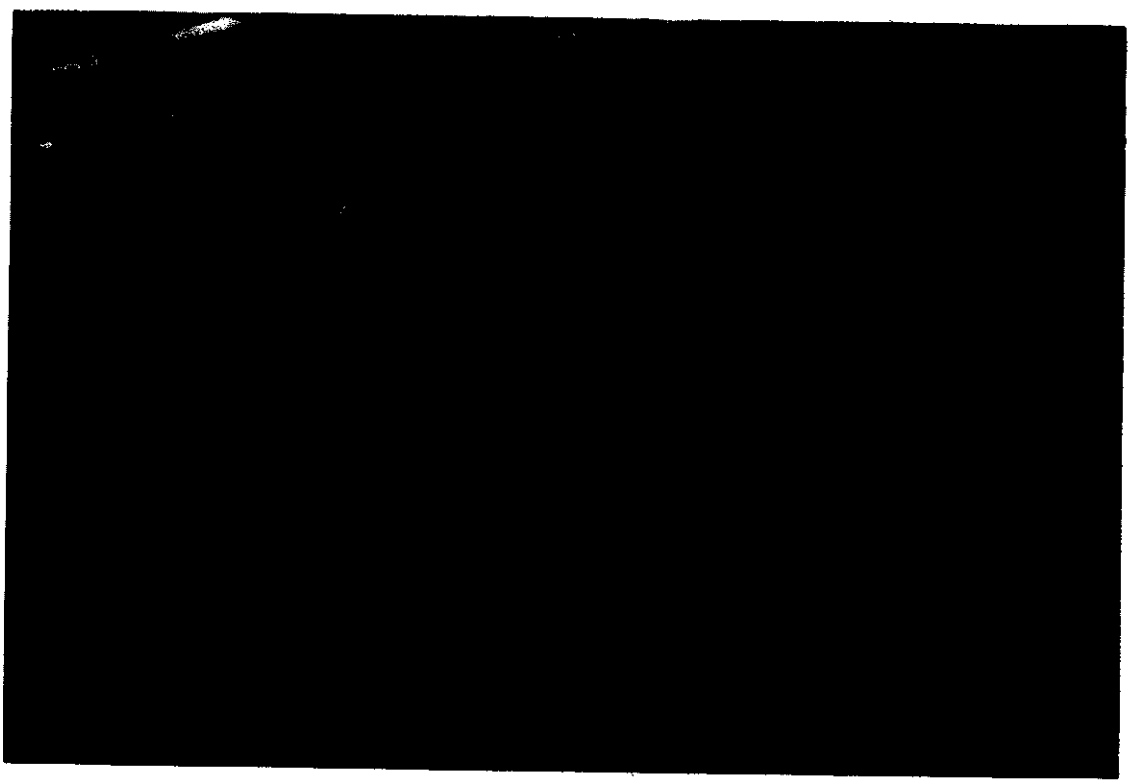

Figure 3: The radiation shielding being put in place around the focal plane detector.

Field mapping was then done on both dipoles. The mapper was used first in D1 then removed and installed in D2. During mapping, both dipoles were energized to the same central field. A more detailed description is given elsewhere in this Report.

The Q1/Q2 doublet, with its sextupole coils in Q2, was assembled and tested before installation on the carriage. The quadrupoles were trained up to their operating levels, and the sextupole was tested.

Detailed field maps were taken and the results are given in another Report. The cryostat is shown in place on the carriage in Fig. 2.

**Carriage and Vault**

The platforms around the dipoles was completed and the detector housing installed. The radiation shielding for the detector box was then put in place. This is shown in Fig. 3. The focal plane detector was tested prior to its installation in the box. Details are given in another Report. In order to accommodate the shielding around the detector box, a "hat" in the roof shielding was needed. This results in a step in the roof shielding. All of the shielding walls and the roof beams were completed and put in place prior to running beam to the focal plane. Air conditioning will be installed before next summer.

The complete spectrometer is shown in Fig. 4. The first spectrum was taken on September 7$^{th}$ and the first experiment started on October 6$^{th}$.

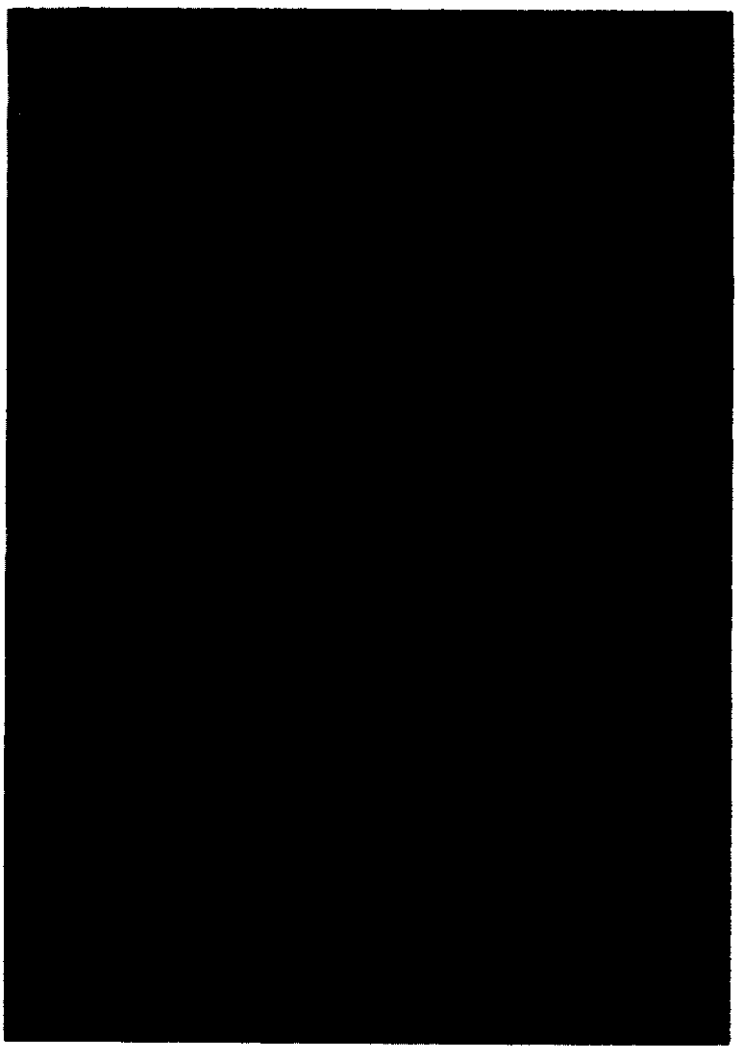

**Figure 4: The complete spectrometer, looking from the bottom of the vault.**

# MAGNETIC ELEMENTS FOR THE A1900

A. Zeller, J. DeKamp, F. Marti, D. Morrissey, B. Sherrill, J. Wagner, X. Wu, R. York and R. Zink

The magnetic elements for the A1900 spectrometer consists of four 45 degree dipoles and twenty-four quadrupoles. The quadrupoles are packaged as triplets and sixteen of them have embedded sextupole and octupole coils. The characteristics of the elements differ from those presented in the CCP "White Paper" (MSUCL-939).

## Dipoles

The gap in the dipole has been decreased to 9 cm rather than the 10 given in MSUCL-939 in an attempt to minimize the amount of return yoke required to keep the field uniformity at 0.1% over the whole dynamic range. This also reduces the current density in the coil package and, hence, the operating current. The final magnetic design was done with the 3D code TOSCA. The properties of the conductor, coil and magnet are listed in table 1.

Table 1. Properties of the A1900 dipoles.

| Conductor | |
|---|---|
| Bare wire size | 0.898 X 1.898 $mm^2$ |
| Cu/Sc ratio | 9:1 |
| Maximum operating current | 161.3 A |
| Critical current (2 T) | 500 A |
| Coil | |
| Number of turns | 600 (25 turns X 24 layers) |
| Current density | 6450 $A/cm^2$ |
| Maximum quench internal voltage | 413 V |
| Maximum quench temperature | 216 K |
| Magnet | |
| Gap | 9 cm |
| Stored energy | 0.53 MJ |
| Maximum central field | 2 T |

## Quadrupoles and multipoles

It was decided to construct the A1900 quadrupoles as larger versions of the successful S800 main quads (Q1 and Q2). The advantages of the cold iron quads over the cos(2 ) quads proposed in the White Paper are the lower fields on the coils, smaller current densities, and reduced helium consumption(lower current). As demonstrated by the construction of Q2 for the S800, multipoles may be added to the helium temperature bore tube. The disadvantages are a significantly increased cold mass and the requirements of several different magnet sizes. Because the pole tip field should be < 2.5 T, one single, large magnet design can not be used for those locations needing high gradients. Therefore, we now have five different designs. However, three of them differ only in length. The parameters for the five types of magnets are given in table 2.

The largest aperture quad, QD, is the same as the S800 Q2, only a little longer, and without the sextupole insert. The lengths were maximized to keep the pole tip field as low as possible and to keep the optical parameters of the system as large as possible. Table 3 lists the magnetic, wire and coil parameters for the quads and the multipoles.

The octupole is at a smaller radius than the sextupole, all of which are attached to the 4 K bore tube of the quadrupole. The self inductance of the multipoles is small, but there is a large mutual

inductance, similar to the S800 Q2 quadrupole. Conductor for the multipoles is surplus SSC outer wire. Conductor for the quadrupoles has been ordered.

Table 2. Parameters of the A1900 quadrupoles.

| Type | Number | Iron length | Effective length | Pole tip radius | Warm radius | Multipoles |
|---|---|---|---|---|---|---|
| QA | 4 | 0.65 m | 0.723 m | 13.3 cm | 10 cm | no |
| QB | 12 | 0.325 m | 0.40 m | 15.0 cm | 10 cm | yes(all) |
| QC | 4 | 0.715 m | 0.790 m | 15.0 cm | 10 cm | yes(all) |
| QD | 2 | 0.381 m | 0.486 m | 21.0 cm | 17 cm | no |
| QE | 2 | 0.625 m | 0.70 m | 15.0 cm | 11.6 cm | no |

Table 3. Magnetic, conductor and coil parameters for the A1900 quads and multipoles.

| Type | Max. required gradient (T/m) | Design gradient (T/m) | Induc-tance (H) | Stored energy (kJ) | Max. Current (A) | Turns | Wire diameter (mm) |
|---|---|---|---|---|---|---|---|
| QA | 18.7 | 19.4 | 39.1 | 118 | 77.5 | 1950 | 0.85 |
| QB | 13.6 | 15.8 | 41.5 | 78 | 61.3 | 2820 | 0.80 |
| QC | 14.4 | 15.8 | 41.3 | 154 | 86.4 | 2000 | 0.95 |
| QD | 11.0 | 12.2 | 4.85 | 372 | 414 | 870 | 1.35 |
| QE | 14.4 | 15.8 | 36.1 | 135 | 86.4 | 2000 | 0.95 |
| Sex-tupole | 1.23 $T/m^2$ | 1.58 $T/m^2$ | small | small | 37.5 | 270 | 0.648 |
| Octupole | 0.54 $T/m^3$ | 0.62 $T/m^3$ | small | small | 19.2 | 260 | 0.648 |

**Miscellaneous magnets**

To get the beam from the K1200 on axis at the A1900 target, the present quadrupole triplet in front of the A1200 will be modified. The new magnetic elements will be placed in a single cryostat and will consist of a dipole double and a quadrupole doublet. In order to get everything to fit in the available space, the quad doublet will be constructed of two half size quads. These are the present outer magnets in the A1200 triplets. The dipole doublets will be wound with more surplus SSC wire and operate at 40 A, giving sufficient deflection to put any beam presently run from the K1200 on axis at the entrance of the quad doublet.

# S800 SPECTROGRAPH DIPOLE MAPPING

J. A. Caggiano, D. Bazin, B. S. Davids, R. Fontus, D. Karnes, P. Johnson, B. Sherrill, and A. Zeller

## 1.0 INTRODUCTION

The S800 spectrograph dipole mapping campaign was completed successfully in May of 1996. Roughly 6 GBytes of data were taken at fields ranging from 0.25 Tesla to 1.6 Tesla. This campaign was part II of the entire spectrograph dipole mapping effort. Part I was described in last year's annual report[1], and consisted of debugging the mapping techniques with only the first spectrograph dipole present. Part II was the final mapping, with improved techniques and both dipoles present.

## 2.0 TECHNIQUE

### 2.1 Overview

The mapping methods have been described in previous annual reports [1] [2]. Five inductive coils pass through the magnetic field and the voltage induced on the coils is measured. The voltage is proportional to the first derivative of the field, so the field at any point is the time integral of the voltage.

The mapping algorithm moves the coils in a polar coordinate system, making 110° sweeps on an arc of fixed radius. After two sweeps at the same radius, the cart stops at a motor, which moves the coils 2.3 mm towards a smaller radius, then starts another lap at the new radius. This rastering procedure is repeated until the coils have reached their final radial position. The radial extent of the coil motion was 2.33-3.01 meters in the magnet steel coordinate system.

### 2.2 Data Acquisition (DAQ) hardware

The system consisted of 5 coils, one in the midplane, 3 above and one below. Five ADC's, one scaler board, and one motor-control board were present in the backplane of the computer to handle position, time, and voltage measurements and also to control the motion of the cart which carried the coils through the field[1].

The relative position of the cart was measured by reading a strip of fine teeth with an infrared transmissive sensor. This produces a square wave whose rising edges indicate the motion of the cart past one of the edges of the teeth. (The falling edges are not reliable due to the sensor design. This was checked by using both the rising and falling edges to determine the cart speed. Using the falling edges gave rise to an unrealistic and discontinuous cart speed. ) From the pitch of the teeth and measurement of the time between rising edges, it is possible to determine the position and speed of the cart at any time. The strip is a continuous, alternating string of 0.010 inch gaps and 0.020 inch teeth. The accuracy of the teeth is 0.002", which translates to a maximum field uncertainty of 3 Gauss.

The field maps are referenced to the magnet steel by mapping small, strong magnets (1x1x2cm, $B_{max}$ ~5 kilogauss) placed directly on the magnet steel edges. Using this technique, the field maps can be referenced to the steel within ~50$\mu$m in the azimuthal direction, for a maximum field uncertainty of 0.6 Gauss. It may be possible to remove the remaining positional uncertainty by comparing transfer maps

[1] The ADCs were AD1170 chips on a PC board, model no. AC5004, designed and built by Analog Devices. The scaler board was based on the AM9513 timer chip and was provided by Computer Boards, model no. CIO-CTR10. The PCX board used to control the motion of the stepper motors was provided by Oregon Micro Systems.

generated from field maps and those determined empirically with beam, though this technique has yet to be attempted.

All times were measured with the scaler board. The square waveform from the position sensor and the ADC "live" and "start" signals were suitable for use with the scaler channels. The waveforms acted as gates, and the board counted its internal clock pulses (f=1.0 MHz) while the gate was open. Test measurements of known waveforms indicated an accuracy of 1 $\mu$sec, which is also the precision of the technique as well. This relates to a maximum field uncertainty from time measurement of 0.01 Gauss. Figure 1 shows a timing diagram for the events of one field sample.

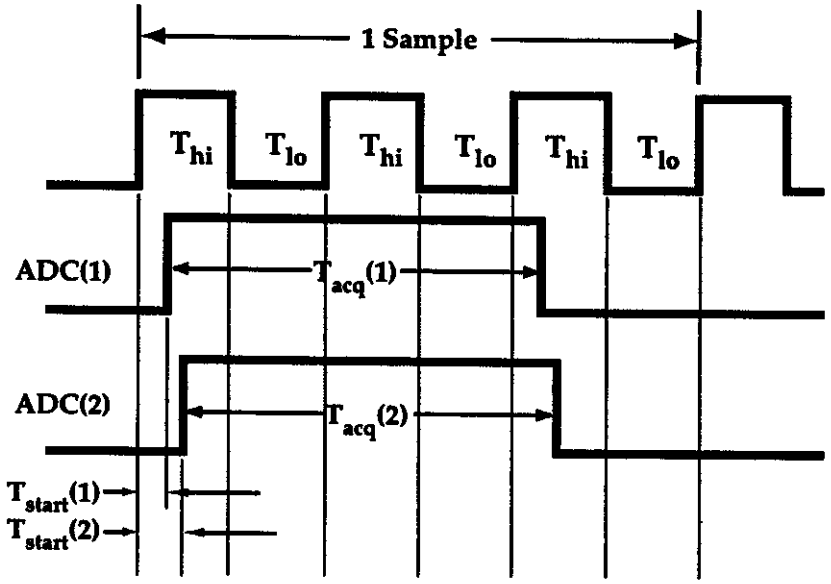


Figure 1: Timing diagram for the events of one sample. $T_{acq}(i)$ is the live time for the ith ADC. Only two of the five ADCs are shown. Typical start times for the ADCs are 300 microseconds for the first one, then $\sim 300 + 8 \cdot (i-1)$ microseconds for the ith ADC.

The ADCs are claimed to have 22-bit resolution, with the last two bits unusable. Hence, the data was collected in 20-bit mode. The post-processing software gives the user the option to truncate any number of least significant bits. The raw voltage signal was amplified using fairly standard operational amplifiers, with simple gain and offset trim circuits to enable full use of the ADC range during measurement.

The ADCs were subject to a noisy environment because they resided in a computer. This was partially remedied by the use of a non-standard, non-switching power supply for the computer (the highest frequency present in the supply is line frequency). However, hard drive and RAM access produce noisy transients on the input signal of roughly 0.2 Volts peak-to-peak. Since the ADC's integrate the input signal (essentially a voltage-to- frequency type converter), the noise was less noticeable. An integration (acquisition) time of 16.67 ms was used for high common mode rejection. Cooling the computer case to about 5° Celsius and internal shielding of the ADC boards reduces the noise by roughly a factor of two. Final output noise levels were $\sim$1 millivolt peak-to-peak for any DC input voltage.

### 2.3 DAQ Software

The acquisition software was written in Pascal on an IBM compatible computer. The program controlled the motion of the coils in both the radial and azimuthal directions through the field. Event timing and data collection was also controlled in this manner.

| N | $T_s$ | $T_{hi}$ | $T_{lo}$ | $T_{hi}$ | $T_{lo}$ | $T_{hi}$ | $T_{lo}$ | $T_{acq}(1)$ | $T_{acq}(2)$ | $T_{acq}(3)$ | $T_{acq}(4)$ | $T_{acq}(5)$ | $V_{hi}$ | $V_{mid}$ | $V_{lo}$ | etc |
|---|---|---|---|---|---|---|---|---|---|---|---|---|---|---|---|---|
| 0 | 304 | 4144 | 3286 | 4469 | 3535 | 4757 | 3614 | 17002 | 16991 | 16974 | 17011 | 16997 | 7 | 251 | 96 | ... |
| 3 | 304 | 4763 | 3429 | 4560 | 3365 | 4519 | 3560 | 17000 | 16965 | 16981 | 17001 | 16998 | 7 | 251 | 148 | ... |
| 6 | 305 | 4806 | 3779 | 4771 | 3518 | 4590 | 3335 | 16968 | 16986 | 16998 | 17002 | 16970 | 7 | 251 | 212 | ... |

Table 1: Sample portion of raw data file. N is the tooth number. $T_s$ is the time it takes the first ADC to start, $T_{hi}$ is the time spent while the position waveform is at +5Vdc, $T_{lo}$ is the time spent while the waveform is at 0Vdc (see Figure 1), $T_{acq}$(i) is the acquisition (live) time for the ith ADC (all times are in microseconds). $V_{hi}$, $V_{mid}$, $V_{lo}$ are the three bytes of raw data collected from the ADC's. Raw voltage data is only shown for one ADC.

The data collection was broken up into samples that were three periods long on the positioning strip (2.3mm). This allowed sampling on a regularly spaced polar coordinate grid, making data manipulation easier. A sample of data consisted of a tooth count, start time for the 1st ADC, acquisition times for all five ADCs, timing measurements for each portion of the waveform, and the raw ADC data (3 bytes). Table 1 shows a sample portion of a raw data file.

One unforseen aspect of the cart riding vertically was that the cart bounced as it passed through the field. In some instances, the cart was too fast for the acquisition time, and the acquisition didn't end until after the next sample was supposed to begin. This type of event was marked in the data file by setting all the times equal to 10 microseconds, an unrealistic event time. The algorithm for handling this type of event was to skip one sample and start at the next one. This was corrected in post-processing software by making a third order interpolation over the missing data point in both voltage and times.

### 2.4 Field Calibration Measurements

A F. W. Bell gaussmeter with a 2", uniaxial hall probe was used to measure the field where the coils started their motion. A probe holder was designed to measure the fields at all of the radii where the sweeps were performed. The measurements were made at 2.54 cm intervals along the starting angle of the coils, and at the 5 different coil locations. A polynomial fit is applied to the data, and the field is then calculated at the starting point for each coil. Figure 2 shows a set of hall probe measurements for D2 at 1.6 Tesla.

The absolute magnitude of the fields was measured with an NMR probe. The probe was placed at a known position (r,$\theta$) in the map, and the field was measured in the planes of the 5 coils. The NMR measurements are accurate to better than 0.1 Gauss. Figure 3 shows the NMR values as a function of current for each of the dipoles.

Once the dead-time corrections are applied and the data is integrated along the angle, the uncalibrated field for one coil, F(r,$\theta$), is known at the calibration points. The scaling factor, S, for F(r,$\theta$) is then

$$S = \frac{B_{nmr}(r_{nmr}, \theta_{nmr}) - B_{hall}(r_{nmr}, \theta_{start})}{F(r_{nmr}, \theta_{nmr}) - F(r_{nmr}, \theta_{start})}.$$

The calibrated fields are given by

$$B(r, \theta) = B_{hall}(r, \theta_{start}) - F(r, \theta_{start}) + S \cdot F(r, \theta).$$

### 2.5 Post-Processing Software

#### 2.5.1 Overview

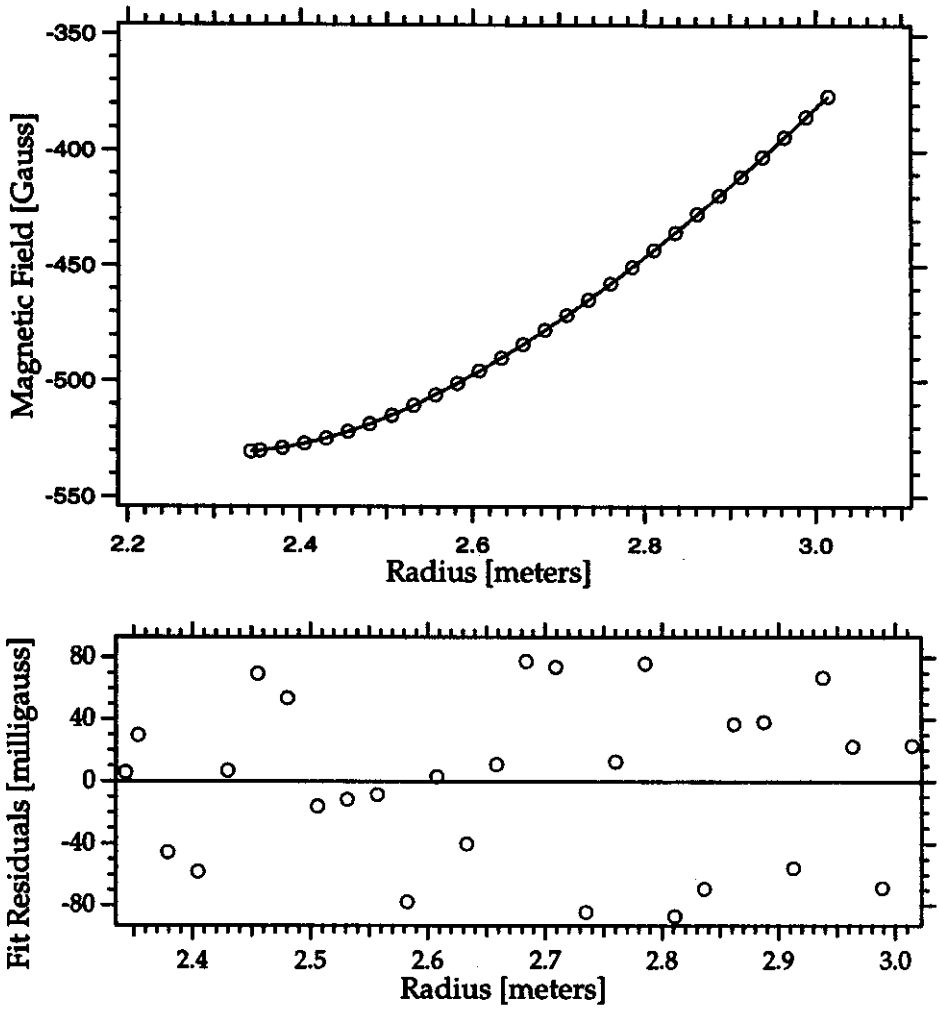


Figure 2: Hall probe data for the midplane coil position for D2 at 1.6 Tesla. The line through the data is a 5th order polynomial fit. Note that the fit residuals are all less than 0.1 Gauss.

The post-processing software was written in VAX Fortran to read a raw data file and convert it to a meaningful B(r,$\theta$,z) and B(x,y,z) map. The raw data is integrated to obtain field values at each sample position in space. This includes accounting for dead time in the ADCs and bad sample events. The program automatically calibrates the field measurements and properly positions the maps with respect to the magnet steel based on field and position calibration measurements. The program interpolates the data from a grid in cylindrical coordinates to a grid in cartesian coordinates.

### 2.5.2 Dead-Time Correction

In the primary mapping campaign, the position measurement resolution was only 2.3 mm. When comparing two identical sweeps through the magnet, it was noted that the field differences were large in portions of the map where the cart acceleration was the high (as large as 0.5 m/s$^2$). In addition, the errors were largest when there were large differences in acceleration between two passes. Since the voltage integral, $\int V dt$, is independent of acceleration and velocity, it was thought that the error was due to insufficient position resolution. The position resolution was increased by a factor of three for the secondary mapping campaign, from 2.3 mm to 0.76 mm.

A measurement of the dead time is easily extracted from the timing diagram. The unmeasured

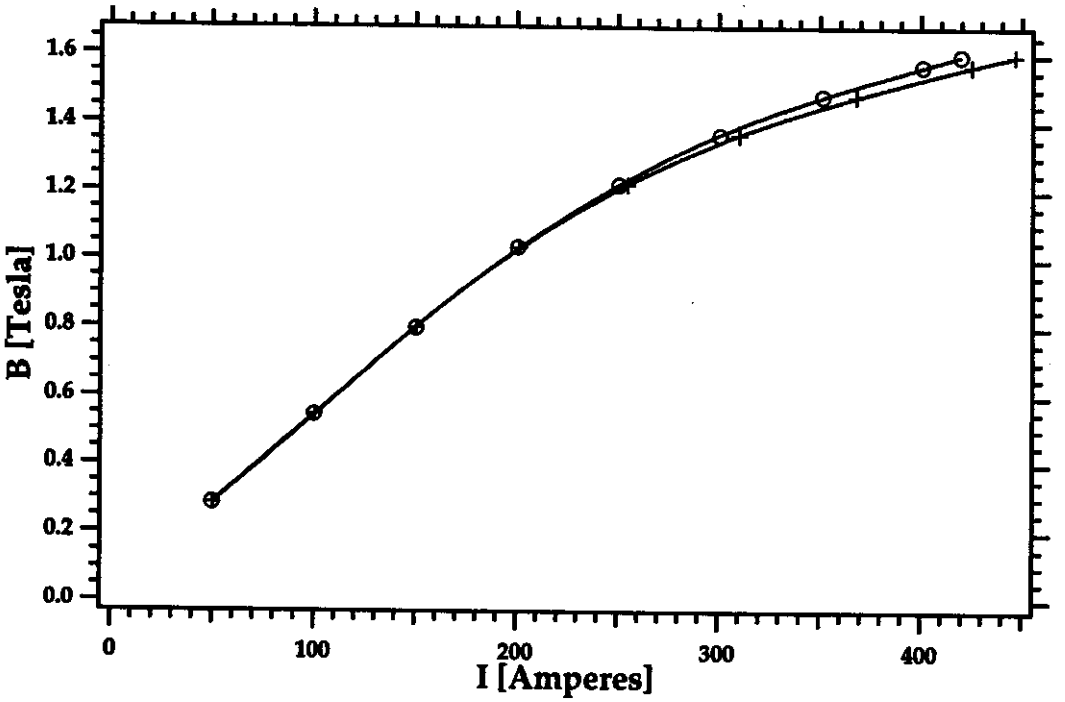


Figure 3: Excitation function for both D1(+) and D2(○), based on NMR measurements. Lines through data are 5th order polynomial fits.

voltage is more difficult to ascertain. Using the improved position resolution, a 2nd order interpolation in voltage was made over the dead region. This voltage was multiplied with the dead time and added to the sample at that point in space to arrive at the corrected field value. The field differences between passes have been reduced from ~ 50 Gauss to less than 10 Gauss using the improved position resolution. Note that the correction would be unnecessary if there were no dead-time, or if the speed of the coils was constant.

### 2.5.3 Output

The user has several analysis options including filtering, smoothing, interpolation methods[2], and output file format. The output file consists of historic data such as time and date the file was created, and the analysis options the user chooses. The field grid is specified by starting and ending cartesian coordinates, the grid pitch, and number of points. The output files are zero-suppressed and in binary format to conserve storage space.

## 3.0 RESULTS

D1 was mapped first (with D1 and D2 both at the same field value), then the mapper plate was disassembled and removed from D1 and inserted into D2. D2 was then mapped, again with D1 and D2 at the same field values. Figure 4 shows a sample of both fields mapped at B=1.58 Tesla. The magnets were mapped in round-the-clock fashion to facilitate timely spectrograph completion. All of the maps have been processed to look for errors, and final analysis is ongoing.

Most errors that were present in the previous mapping campaign have been reduced to tolerable levels. As mentioned previously, improved position and time measurement has reduced dead-time errors from ~ 50 Gauss to less than 10 Gauss. In addition, using fitting techniques[2], the errors can be reduced

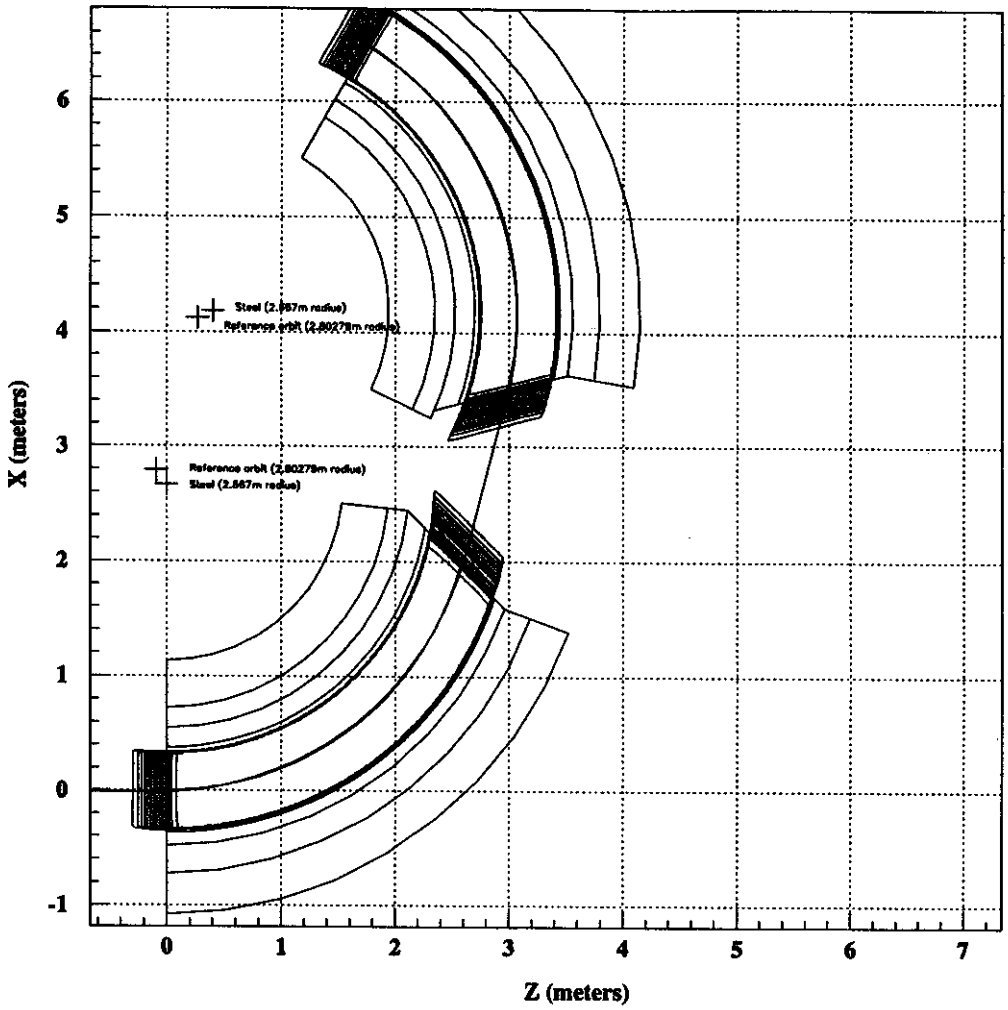


Figure 4: Magnetic field data for D1 and D2 at B=1.58 Tesla, 300 Gauss contours. The magnet steel outlines are shown for reference. The reference trajectory is drawn through the centers of the magnets. The physical center of the beam pipe is also drawn. The corresponding centers of these arcs are drawn as well.

to $\leq$1 Gauss. At this level, absolute position with respect to the magnet steel becomes the dominant uncertainty.

## 4.0 ACKNOWLEDGEMENTS

The authors would like to thank the many assistants who made the round-the-clock mapping effort possible. For Part I they were Mathias Steiner, Luke Chen, Njema Frazier, Sally Gaff, Damian Handzy, John Kelley, Jon Kruse, Raman Pfaff, Shigeru Yokoyama, and Bo Zhang. Don Anthony, Amy Balint, Luke Chen, Jim Brown, Marcus Chromik, Heiko Scheit and Bo Zhang helped in part II.

## References

1. J. Caggiano et al., "Automated Data Acquisition System for S800 Dipole Magnetic Field Mapping",1995 NSCL Annual Report.
2. J. Caggiano et al., "Data Analysis Techniques for S800 Dipole Magnetic Field Maps",1995 NSCL Annual Report.

# MAGNETIC FIELD MAPPING OF THE S800 Q1 AND Q2

B. Zhang, S. Bricker, J. DeKamp, P. Johnson, B. Sherrill, A. Zeller, R. Zink

The two superconducting quadrupoles, for use in S800, have been constructed and mapped [1]. A sextupole, which is within one of the quadrupoles, has been mounted on the helium vessel bore tube. All the elements are assembled into the same cryostat. The mapped results, obtained with a three axis Hall probe, are compared to 3-dimensional calculations over the entire range of operation.

The Q1, Q2 and sextupole magnets are mapped by using a quadrupole mapper. A z-axis step of 1 cm requires 180 revolutions in order adequately measure the length of the Q1, Q2 and sextupole magnets and fringe fields. A one degree map takes 43 hours to complete, with the mapping process requiring minimal operator supervision. Maps for different sets of currents have been done. On two poles of the Q1 and Q2 magnets a cryogenic Hall Generator was calibrated with the mapper gaussmeter at a known radius with a calibrated power supply. Each quadrupole has its own calibration of gradient versus current (by reference to the cryogenic Hall generator). The sextupole was mapped when the Q1 and Q2 magnets were on or off.

The measured and TOSCA calculations of the effective lengths of Q1 and Q2 have been compared. The effective lengths of Q1 and Q2 decrease when the magnetic fields increase like beamline quads [2], the Q1 effective length differs by less a 1 % from the TOSCA calculations. For Q2 the effective length has a 2 % difference at low field, but gives close agreement at high currents. Figure 1 and Figure 2 show the harmonic content at the center and end of Q1 and Q2 at a radius of 8.8 cm. Note that only N=6 and 10 terms are theoretically allowed, and the rest of the terms must result from construction errors, and/or mapper errors. The N=6 terms at center of the magnets differ in sign and magnitude from those terms at end of the magnets. This is due to the coil return at the ends which introduces significant higher order multipoles in the magnetic field.

The measured and TOSCA calculations of the multipole components of Q1 have been compared. Fig. 3 shows the various multipole components as a function of z. The field inside the Q1 magnet is dominated by straight section of the coils, producing an almost pure quadrupole field. Near the ends of the Q1 magnet, the higher order multipole fields increase greatly in strength. When the currents of the Q1 and Q2 magnets change, the sextupole, octupole and decapole components remain almost constant. However, the dodecapole components are strongly current dependant and are much larger at the ends of the magnets than at their centers. We also mapped Q2 with the sextupole magnet on and off. During mapping process, the field interaction between Q1 and Q2 has been measured. The field at the center of each magnet is independent of the other throughout the whole dynamic range.

The contribution to the magnetic field uncertainties from the mapping apparatus have been studied. The major error source likely comes from mapper/magnet misalignment. When we installed the mapper into the Q1/Q2 doublet, alignment was done using as optical transit. However, mapper/magnet alignment was extremely difficult and the difference between centers of less than $\pm$ 0.0127 cm could not be achieved. This error produces 0.1 % systematic error. Also, the Hall probe is temperature dependent with a temperature coefficient of $\pm$ 0.02%/C [3]. Once the mapper achieved thermal equilibrium in the bore of the doublet it changed little during mapping process. Therefore the relative contributions are very small, this does, however, limit the absolute field calibration of the magnets to $\pm$ 0.04%.

Two superconducting quadrupoles and the sextupole for the S800 spectrometer have been con-

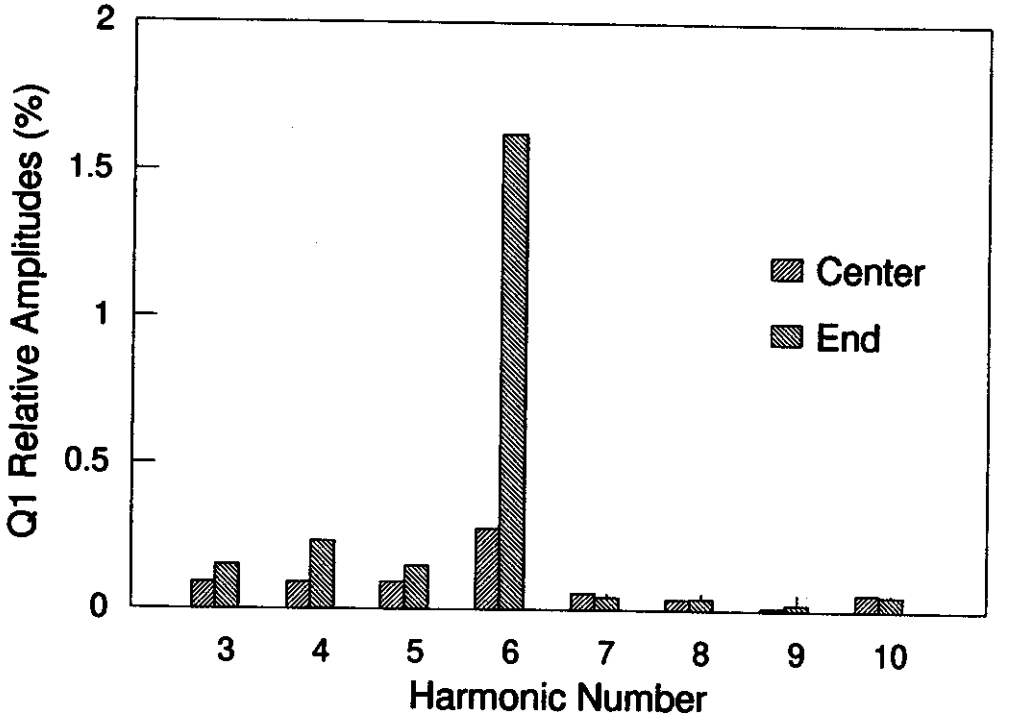


Figure 1: Fourier analysis of the radial component of the field at the center and end of Q1 at I = 45 A.

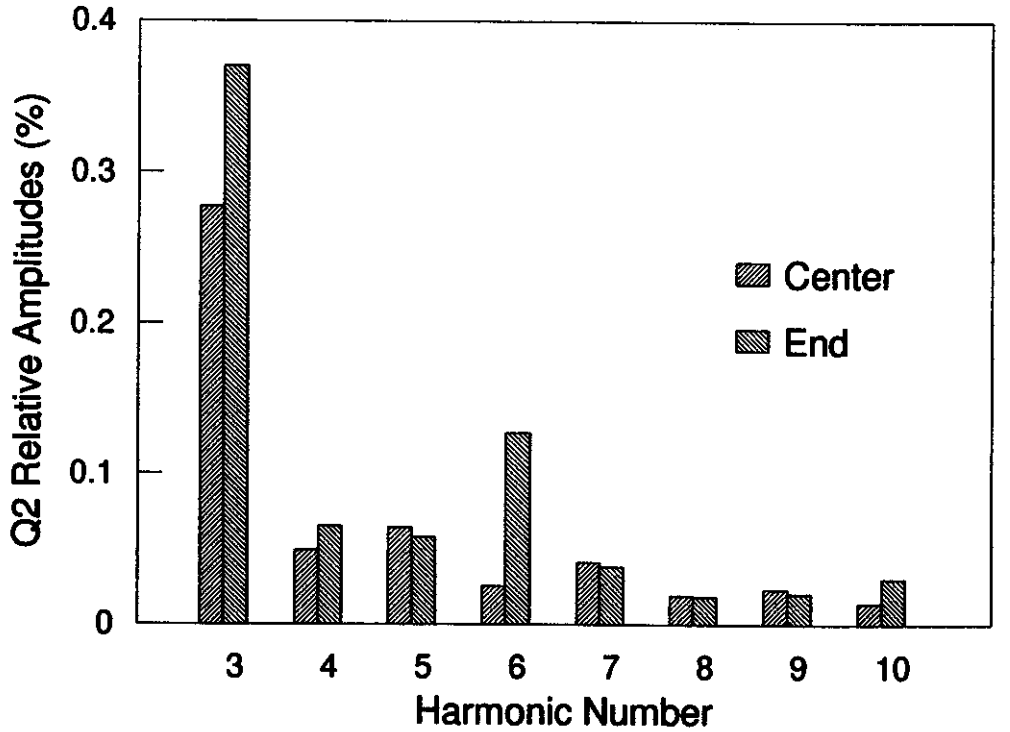


Figure 2: Fourier analysis of the radial component of the field at the center and end of Q2 at I = 45 A.

structed and mapped. The magnetic field measurements are consistent with our numerical calculations and of sufficient quality for use operation as spectrometer elements.

## References


1. B. Zhang, A. F. Zeller, S. Bricker, R. Berleigh, J. DeKamp, P. Johnson, B. Sherrill, R. Swanson, R. Zink, Performance of the high gradient, large aperture quadrupoles for the NSCL superconducting spectrometer, *IEEE Trans. on Applied Superconductivity,* in press (1997)
2. B. Zhang, P. Johnson, B. Sherrill, A. F. Zeller, R. Zink, S800 beamline quadrupole triplet mapping, *MSU Ann. Report,* (1995) 229-233.
3. F. W. Bell, *Operation Manual,* Series 9900 Gaussmeter, 1.


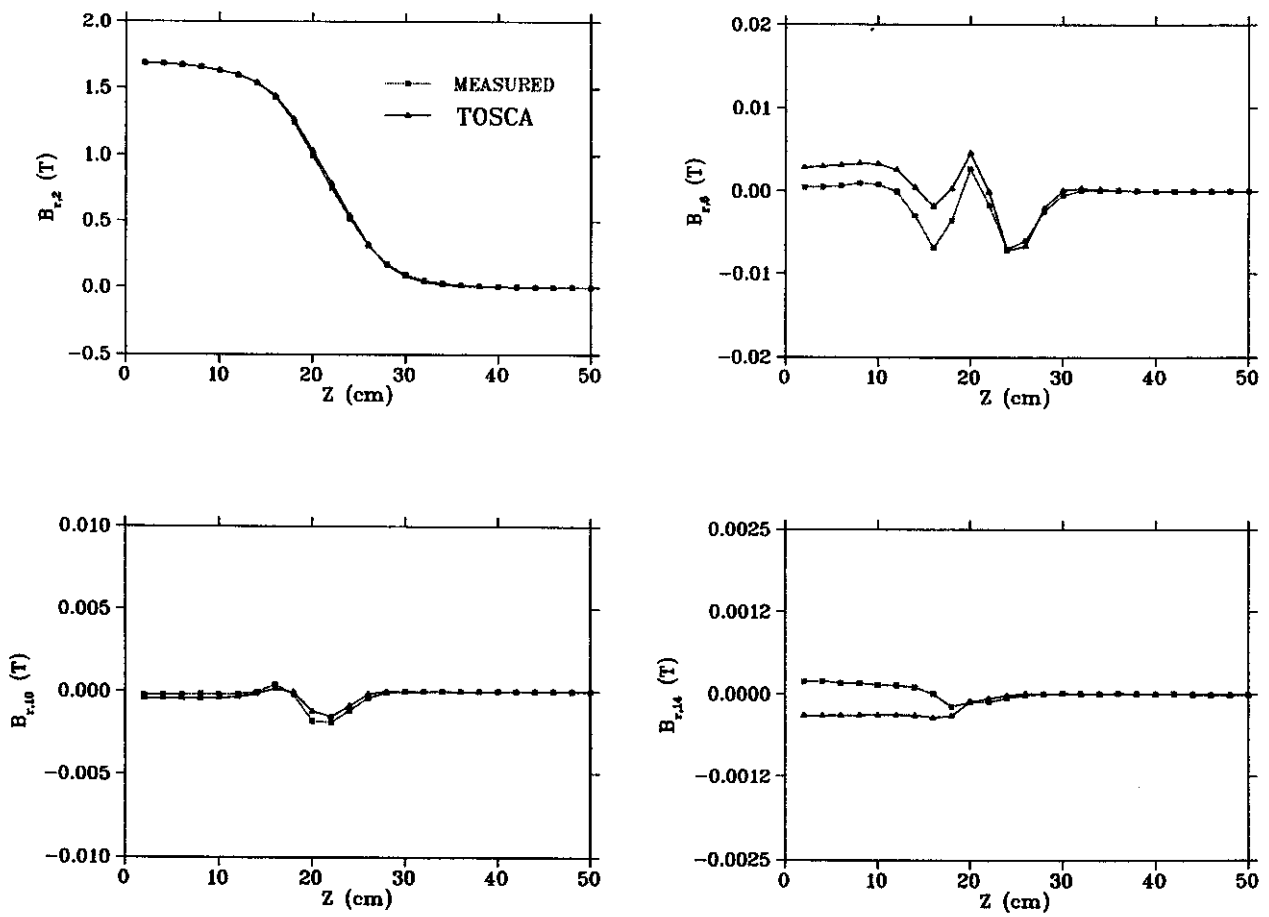


Figure 3: Multipole components of the Q1 radial field for the quadrupole (n=2) term and the first three allowed terms (n=6,10 and 14) are plotted as functions of z, the distance along the beamline axis at r = 8.8 cm and I = 80 A.

# THE PHYSICAL ALIGNMENT OF THE S800 SPECTROGRAPH

D. P. Sanderson and L. Morris

The S800 spectrograph is a large three-dimensional object positioned at the end of a beamline with great precision. This report will describe the techniques used to orient the magnets and detector to their theoretical positions in the S3 experimental vault. The magnetic alignment of the devices has already been described in earlier NSCL annual reports.[1-5]

The beam enters the laboratory's S3 vault at the main floor level and travels downward to the center of the pit through an analysis system composed of superconducting beamline magnets. The positioning of this system has been described previously[6]. At the end of the analysis system is a small scattering chamber with a target located above the center of rotation of the magnetic spectrograph. The products of the reaction in the target are focused by the Q1/Q2 superconducting quadrupole doublet and analyzed upward by two superconducting dipoles, D1/D2. At the exit of the dipoles is a large vacuum chamber housing position sensitive and total energy detectors. The whole assembly is riding on a rotating carriage following a hardened steel track grouted to the floor. A central bearing keeps the radius constant during rotation.

The track is a set of ground hardened steel plates, 38 cm. wide, located 140 cm. below the beam axis. The carriage wheels are not constrained radially at the track, so the radial position of these plates is insensitive. The height and levelness of the track was set by comparing the top surface to a vertical height benchmark on the north wall of the vault. When the beamline benchmarks were originally laid out in the vault, the location of the central pivot was set at the center of the sub-pit. Two jig transits were used to observe this center while the bearing mounts were grouted in. The carriage, both dipoles and the quadrupoles were mounted at this point.

The quadrupoles were aligned as an extension of the beamline. A jig transit was installed at the central pivot point and by viewing upstream and inverting the telescope the carriage could be set to zero degrees. A target was mounted to the carriage for reproducing this position and calibrating the carriage drive system. The beam height benchmark on the north wall of the vault completed the specification of the central axis of the quadrupoles. The height of the magnets was adjusted using wedge-style leveling mounts. The position along the beam axis was set by fixed length standoffs that keep the quads from being pulled toward the first dipole during operation at high magnetic field.

The dipoles D1 and D2 were mounted to the carriage at three points. The adjuster is shown in Figure 1. A large bracket mounts a screw jack with the shaft pointing downward to a ball joint. The cup for the joint sits on two sets of cross-rollers with push screws on three sides. Three of these orthogonal adjusters allow the magnet to be set and locked to any position with balanced loading of the mounts. Alignment mirror targets were mounted to the pole tips at the entrance of D1 and the exit of D2. Known reference locations on the outside of the return yokes were labeled with adhesive targets. The laboratory's CAD system provided theoretical values for the positions of the two magnets. The dipoles were aligned by using a coordinate system where the axes are: beam direction (X), vertically up (Y), and a horizontal axis pointing northward, perpendicular to the other axes (Z).

A jig transit was installed at the central pivot of the carriage. By viewing the mirror target at the entrance to D1, the Y and Z coordinates of this point were set. By autoreflection in the mirror, rotations about the Y and Z axis are observed. These rotations were only used for coarse adjustment since any extraneous material under the mounting plate greatly magnifies the apparent error. Two rotations, about the X and Y axes, were observed using magnetically clamped tooling scales placed against the pole tips.

These scales allowed the rotations to be set to within 10 arc-seconds. Rotations about the Z axis and position along the X axis were not measurable from this position.

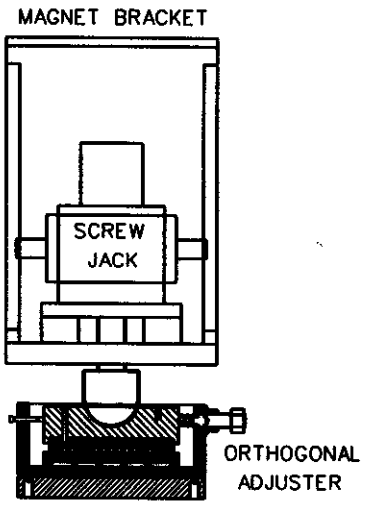


Figure 1: The dipole orthogonal adjusters.

The most cost effective technique using existing laboratory optical tooling hardware to measure these two coordinates was the tooling dock [7]. (Figure 2.) A tooling dock consists of a high precision scale placed parallel to the coordinate to be measured and a transit mounted on a moveable carriage. The scale was fabricated by boring evenly spaced holes along a cold rolled steel bar. A high precision spring-loaded scale is moved from position to position to take a reading. The jig transit is mounted on a sliding carriage parallel to the scale. A autoreflection mirror on the transit is viewed by an alignment telescope at the end of the rail to maintain a perpendicular angle of the transit axis to the scale. The transit views a target on the magnet and plunges down to read the scale value. By mounting the scale and transit carriage vertically, another coordinate can be measured. In the vertical position the alignment telescope is not needed since leveling the transit to gravity keeps it perpendicular to the scale.

Two tooling docks were installed in the vault, one horizontal to the south of the magnets and one vertical clamped to the wall. The two docks allowed the measurement of the X position and Z rotation of D1. Simultaneously, the X,Y positions and Z rotations of D2 were observed. The Z position of D2 was measured by mounting a transit to the north wall at the top of the vault, above the central pivot of the carriage. By rotating the transit to the beam axis, it could view down the exit opening of the magnet. Z position and X,Y rotations were set using the mirror target and tooling scales clamped to the pole tip. These techniques located the magnets to within 0.13 mm of their theoretical positions.

Once the dipoles were aligned, the focal plane detector system could be installed. The mirror target mounted at the exit of D2 was viewed by a transit placed on the roofbeams along an axis defined by the path taken by the beam exiting the dipole. The transit was adjusted via autoreflection to the mirror target. The vacuum vessel for the detector was mounted with the mask drives installed. Once the mask drives were inserted, the position of the beam axis in their pattern was noted. The final alignment task was the adjustment of the mounting plate for the position sensitive and ionization detectors. A set of fixtures with glass alignment targets was installed on the plate and the plate was

adjusted to position them to the axis. With the known relationship between these fixtures and the detectors in the plate, this adjustment locates the detectors.

This report has presented a summary of the techniques used to physically place the S800 spectrograph in its theoretical location in the laboratory. The error level is well within the value required by the beam transport calculations. By using existing optical tooling and fabricating a limited number of fixtures, the capital cost of this operation was kept low.

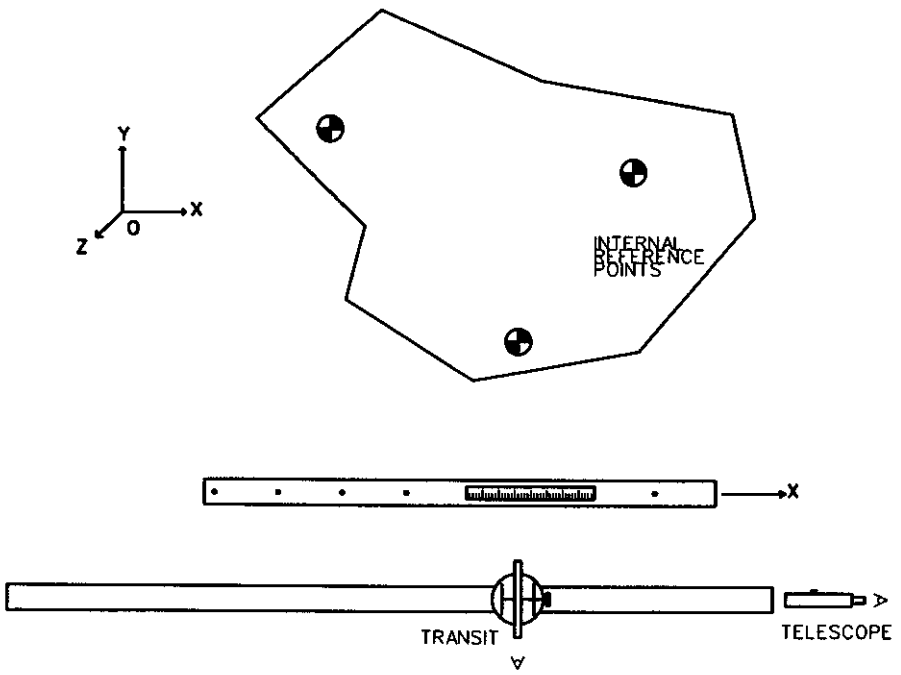


Figure 2: A tooling dock

## References

1. J. A. Caggiano, et al., NSCL Annual Report, (1995) 237
2. J. A. Caggiano and B. M. Sherrill, NSCL Annual Report, (1995) 239
3. J. A. Caggiano and B. M. Sherrill, NSCL Annual Report, (1995) 244
4. D. Bazin and B. M. Sherrill, NSCL Annual Report, (1995) 248
5. D. Bazin and B. M. Sherrill, NSCL Annual Report, (1995) 252
6. D. P. Sanderson, NSCL Annual Report, (1995) 234
7. J. D. McGrae, *Optical Tooling in Industry* (Hayden, New York, 1964), p.72.

# S800 DETECTOR DEVELOPMENT FOR THE S800

J. Yurkon, B. Sherrill, D. Bazin, M. Steiner, D. Swan and R. Swanson

The focal plane detector array for the S800 consists of six detectors as shown in Fig. 1. First are two Cathode Readout Drift Detectors (CRDC), separated by one meter. These are immediately followed by an Ionization chamber. Behind the Ion Chamber is a stack of three scintillators.

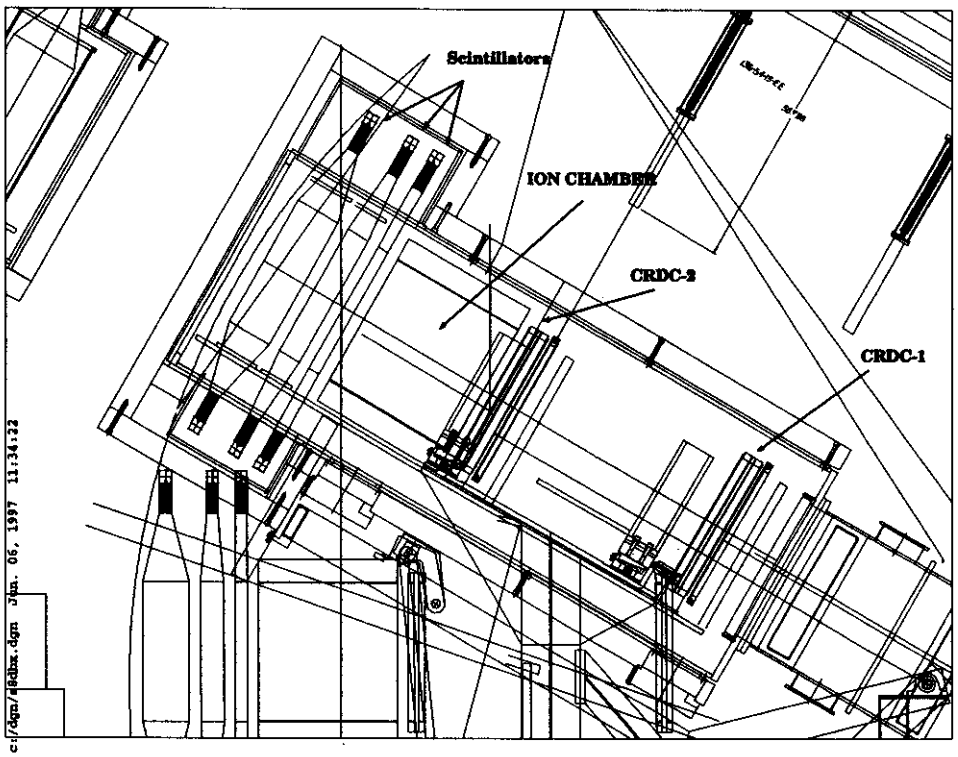


Figure 1: S800 Focal Plane.

The CRDC's have an active region of 59 cm by 30 cm. The active depth is 1.5 cm. The readout mechanism has been described[1] previously. Each counter has seven FEE[2] cards mounted on it. The output of the SAS chips on the card are attenuated, inverted and input into FERA's. For the two detectors this requires 448 coaxial cables to be brought out of the focal plane vacuum box. We are using 3M SCI cables which are grouped into headers of 16 cables. The feedthru's were fabricated out of printed circuit board with 13 connectors per board. The vacuum interface is made by soldering the header connector into the board. The boards were standard 1/16 inch boards with 1/2 oz copper. If these were to be made again, we would use 1/8inch material and make the pads larger to minimize the chance of a fracture from drilling causing a leak.

The windows on the CRDC's are 50 microns thick Poly(p-Phenylene Terephthalamide) film. The gas fill is 80/20 $CF_4$ and $C_4H_{10}$ at 150 Torr.

The ionization chamber has the same active area. The construction is that of a standard Frisch gridded ion chamber. The active depth is 16 inches. There are 16 separate anodes, each 1" wide. The preamplifiers are installed directly on each anode to minimize noise due to cable capacitance. The window

is a Kevlar/Mylar sandwich with a thickness of 14 mg/cm$^2$. The window has been tested to 1 atm, but we have limited the gas fill to 500 Torr of P10. The preamplifier signals are brought out with 3M SCI cables and go to a Silena 761F 16 channel shaping amplifier. The 761F was chosen because of its high density, high gain, low noise and remote control capability.

A 30 cm $x$ 60 cm $x$ 5 cm thick BC408 scintillator was aluminized and forms the exit window of the ionization chamber to reduce the straggling that an extra window would introduce. The scintillator is read out at both ends with an EMI-9807B PMT. These are followed by two additional scintillators of the same geometry, but 10 cm and 20 thick respectively.

The PMT bases are a high standing current (2MA) design for high counting rate stability. These may be replaced in the future with either a Crockcroft Walton or Boosted Base design to reduce the heat generation.

The entire array is in place and has been used in several experiments. The performance will be described in a future report.

## References


1. J. Yurkon, B. Sherrill,D. Morrissey, D. Bazin, J. Brown and D. Swan, NSCL Annual Report, ??? (1995).
2. The STAR Collaboration, LBL Pub-5347 (1992).

# STATUS OF THE K500 CYCLOTRON UPGRADE

T.L. Grimm, J. Bennsinger, S. Bricker, C. Compton, C. Heckman, G. Horner,
F. Marti, J. Ottarson, and R.C. York

An element of the Coupled Cyclotron Project (CCP) is the refurbishing and upgrading of the K500 cyclotron[1]. The K500 was operated from mid-1993 through 1995 to determine the required upgrades, develop beam diagnostics, and measure beam parameters for the injection and coupling beamlines. Many upgrades were implemented during this time including; second harmonic buncher, second harmonic spiral inflector, M4 diagnostic probe, improved extraction optics, and a non-intercepting beam probe. Experimental results showed the extracted beam achieved the CCP requirement for bunch length, and was within a factor of two of the intensity and emittance required[2]. The remaining upgrades will make it possible to reliably achieve all of the CCP specifications for K500 operations.

Construction and commissioning of the new injection line took place during most of 1996. During that time, most of the K500 subsystems were disassembled, and only main magnet operation was maintained to verify the injection line's magnetic shielding and compensation performed adequately[3]. In September 1996 the injection beamline was shutdown and disassembly of the K500 steel began. At that time the vault had been completely stripped with only the K500 steel, cryostat and injection line remaining.

**Work Complete**

Figures 1 and 2 show side and top views of the upgraded K500 cyclotron. The return yoke's median plane was modified to decrease the azimuthal asymmetry in the magnetic field which had forced the coil to operate off-center[4]. The cryostat outer diameter was also modified to decrease any azimuthal asymmetry[5]. The inner diameter of the cryostat was originally nickel plated and had become rusted and pitted. The nickel was stripped, O-ring surfaces polished, and a 0.001" thick copper/gold plate applied. The copper plates more easily than nickel, especially for a damaged piece of steel, and will substantially reduce heating due to rf currents on the cryostat wall. The gold protects the copper from oxidizing.

Vacuum leaks through the liner were repaired. Some of the cooling lines on the liner had been pinched. The lines were replaced, the steel which caused the damage modified, and a new feedthrough to monitor the lines independently was installed. A second O-ring groove was cut in the lower beam chamber seal for increased reliability. In the unlikely event that these seals fail, the design for a return yoke/cryostat lifting system has been completed which will permit servicing of these seals.
Many of the trim coil fittings and all of the trim coil vacuum feedthroughs were replaced. The pole caps have many cracks in the casting which were identified and welded to reduce leaks into the liner vacuum.

**Future Work**

By the end of March 1997 all repairs to the K500 cyclotron were complete and reassembly of the machine started. The vault electrical and lighting was installed, and the low conductivity water distribution was started

New hill extensions were designed to allow shimming of the magnetic field at the extraction radius without disassembling the cyclotron. New center plugs were designed to simplify and improve the vacuum, allow use of the inner trim coil (trim coil zero) without steering the injected beam, and improve axial injection by smoothing the field along the vertical injection line inside the yoke.

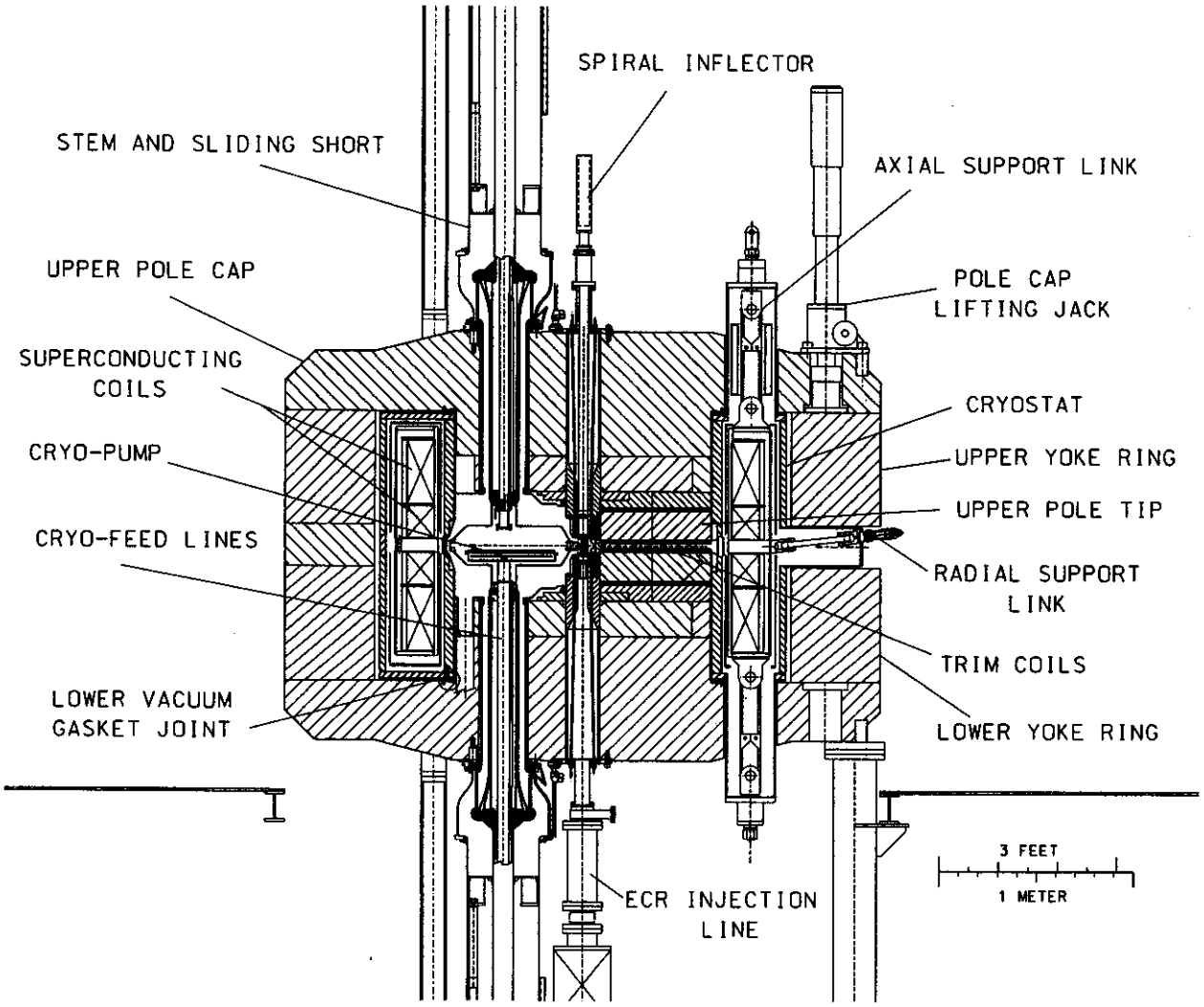


Figure 1: Side View of K500 Cyclotron

A new main magnet power supply and trim coil solid state reversing switches will be constructed. Once the above work is complete, magnetic mapping of the median plane, vertical injection line and extraction line can start. Mapping is planned for the last half of 1997. In parallel with the mapping will be the construction of the rf transmitters and their controls.

In 1998 the resonators, vacuum systems, controls, injection line and extraction elements will be completed with commissioning planned for October 1998. This will allow 9 months for beam development and to debug the system before the K1200/CCP shutdown.

## References

1. York, H. Blosser, T. Grimm, D. Lawton, F. Marti, J. Vincent, X. Wu, and A. Zeller, "Proposed Upgrade of the NSCL", Proc. of the 1995 Particle Accelerator Conference, (1995)
2. Grimm, G. Horner, F. Marti, X.Y. Wu and R.C. York, "K500 Operation for Coupled Cyclotron Development", NSCL Annual Report, p. 157 (1995)

3. Grimm, G. Horner, F. Marti, J. Ottarson, X.Y. Wu and R.C. York, "Commissioning of the K500 Injection Line", NSCL Annual Report (1996)
4. Johnson, "Three-Sector Compensation in K500 Yoke", NSCL-CCP12-1996 (1996)
5. Johnson and F. Marti, "K500 Cryostat Outer Wall Compensation", NSCL-CCP11-1996 (1996)

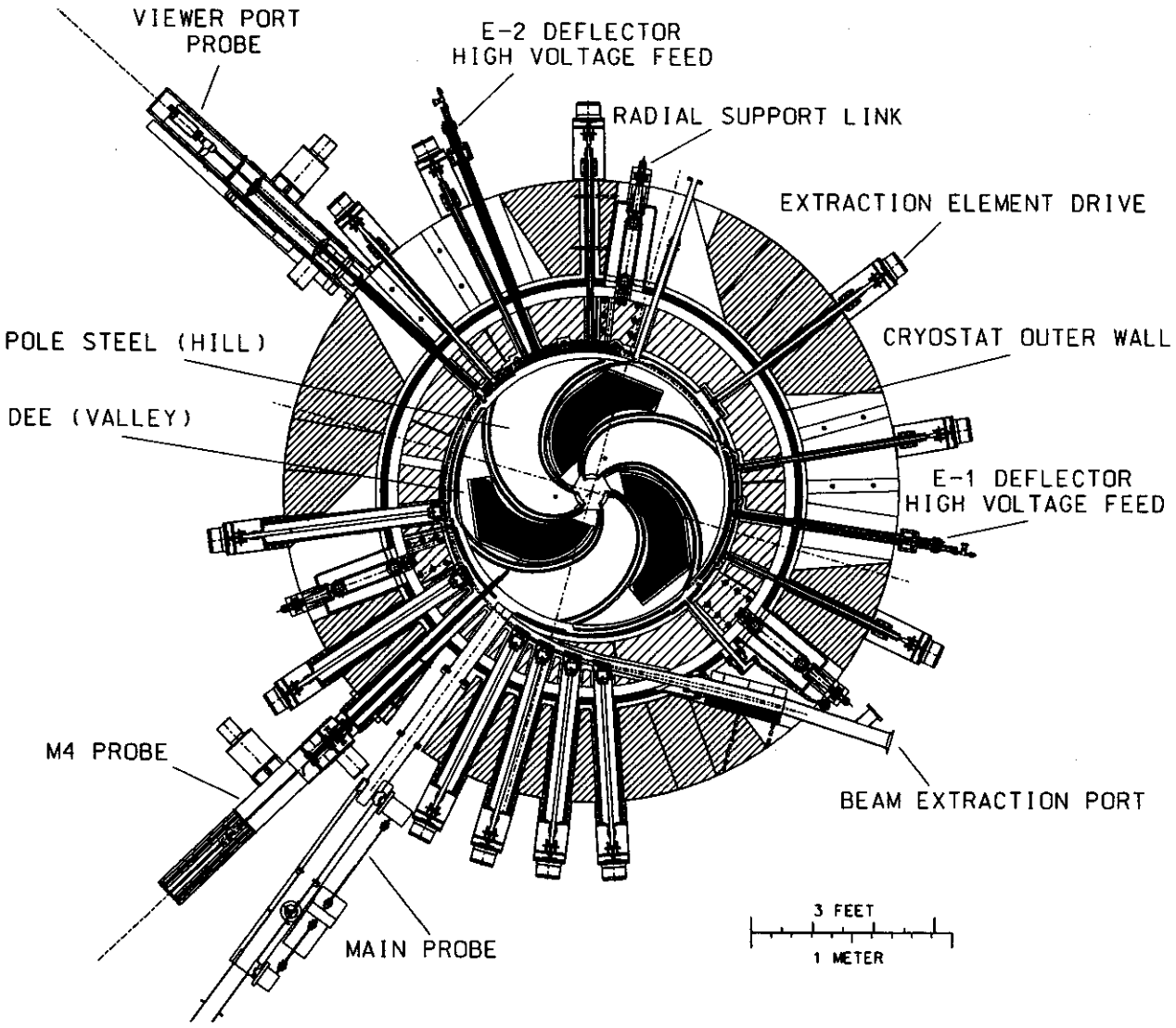


**Figure 2: Top View of K500 Cyclotron**

# COMMISSIONING OF THE K500 INJECTION LINE

T.L. Grimm, G. Horner, F. Marti, J. Ottarson, X.Y. Wu and R.C. York

A new injection line between the superconducting electron cyclotron resonance ion source (SCECR) and the K500 superconducting cyclotron was installed and commissioned for the Coupled Cyclotron Project (CCP) during 1996. The CCP K500 injection line design criteria are Q/A ≤0.2, an ECR voltage ≤30 kV, and a transmission efficiency >50% for a transverse emittance <75 π mm-mrad[1]. During commissioning the design criteria were achieved and for some parameters exceeded.

## Design

Key elements of the design included improvements in the areas of optics, magnetic shielding on the horizontal beamline, and compensating steel on the vertical beamline. The beamline configuration is shown in Fig. 1. From beamline optics studies it was determined that more focusing elements than the previous injection line were required. In particular a quadrupole-doublet at the beginning of the horizontal line to symmeterize the transverse phase space for transport through the solenoid lattice and another quadrupole-doublet near the end of the line to manipulate the transverse phase space for injection were used to improve the transmission.

Operation of the previous injection line had shown that the cyclotron stray fields seriously decreased transmission of the beam. Detailed optics simulations would have been quite complex due to distributed nature of the stray field, and therefore were not done. Instead a shield was constructed to minimize the stray field along the horizontal beamline through the vertical bend until the beam is following the field lines. Continuation of the shield through the 90° dipole under the cyclotron was difficult because of the close spacing of the resonators. Also, the shielding geometry was not axially symmetric which distorts the vertical on-axis field lines and reduces transmission. To regain axial field symmetry while avoiding the resonators, mirror images of the beamline steel were placed at ±120°.

To minimize the amount of steel necessary for magnetic shielding and compensation, especially in the region of the vertical bend beneath the K500 required a new compact electrostatic dipole. This dipole, shown in Fig. 2, operates at voltages ≤ ±10 kV and has a vacuum chamber of one inch thick, nickel plated steel. The one inch thick shielding decreases to 0.5 inch near the vault wall. Along the horizontal beamline, the stray field decreases from 1 kG without shielding to less than 50 gauss inside the shield. The maximum field inside the shield is near the vault wall where the shield thickness decreases. Hot wire tests on the vertical beamline under the K500 showed the compensating steel adequately maintained the central field line on the cyclotron axis.

All elements were aligned to the beamline axis within 0.02 inches using an automatic level or plumb bob. A Faraday cup/viewer screen was place directly above the ES dipole to measure current, beam shape and centering of the beam in the focusing elements. The scintillating material was KBr which has been shown to work quite well at the energies of this injection line.

## Experimental Results

During construction and commissioning of the injection line, the K500 cyclotron was disassembled. Only the K500 magnetic field was maintained to verify that the magnetic shielding and compensation performed adequately. A Faraday cup was placed at the spiral inflector location so the remainder of the cyclotron beam chamber could be vented.

With the cyclotron B-field and correction magnets off, a small fraction of the beam could be transported to the spiral inflector. The low transmission efficiency was expected without the focusing

generated by the cyclotron magnetic field on the vertical line. The cyclotron magnet was then ramped from zero to full field while the beamline elements were held constant. The K500 stray field did not steer the beam off the spiral inflector and even increased the beam current transported to the spiral inflector. This test confirmed that the magnetic shielding on the horizontal line and the magnetic compensation on the vertical line performed as predicted.

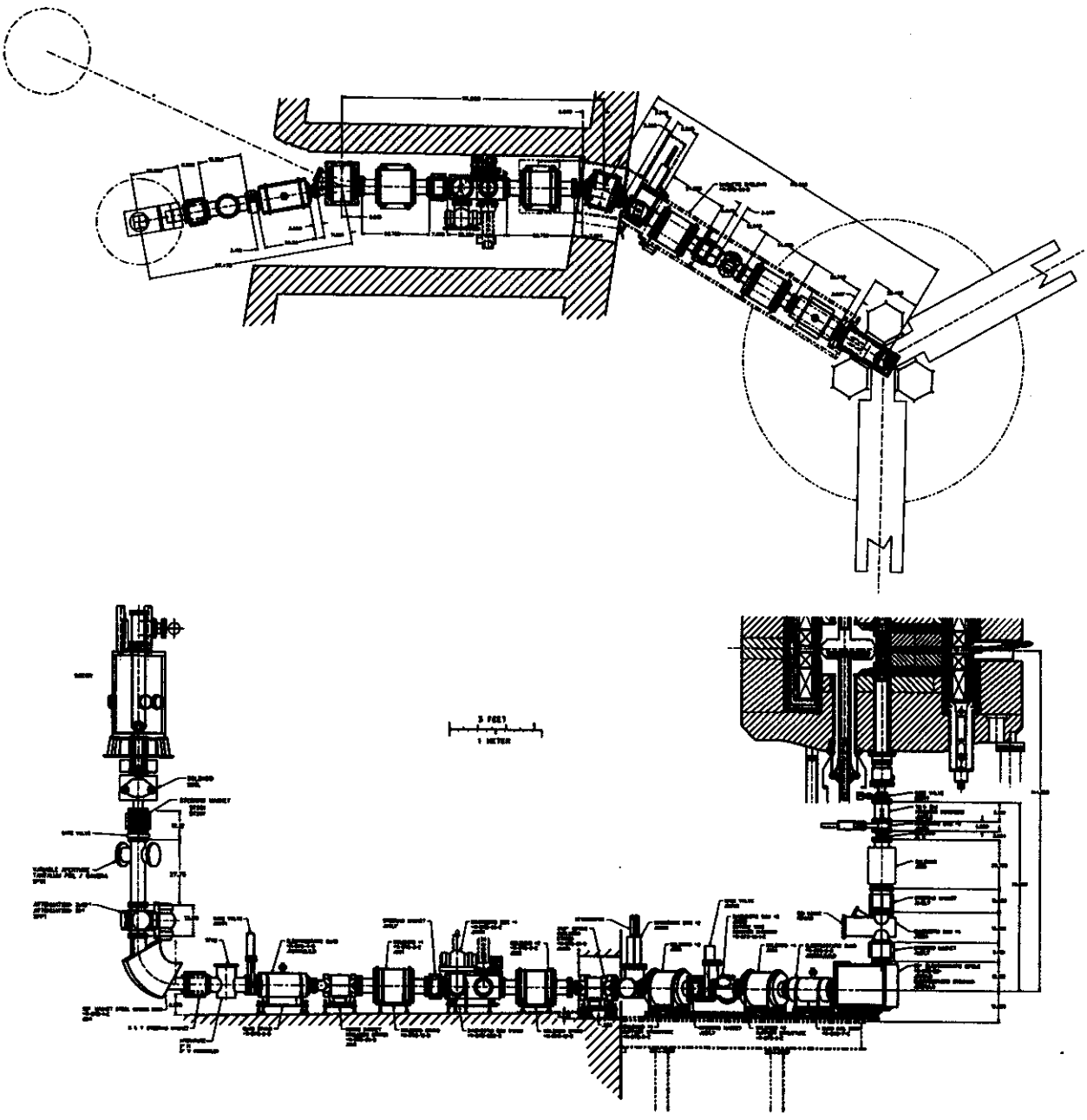

Figure 1: SCECR to K500 Injection Beamline

One of the highest rigidity and current beams required for the CCP was used to maximize current on the spiral inflector. Table 1 shows the results compared to the CCP requirements. During this test a 0.6 inch diameter aperture was placed below the SCECR at the first Faraday cup to limit the emittance

to about 100 π mm-mrad. The first and second harmonic bunchers which block about 10% of the beam were in place. This test confirmed that the K500 injection line can obtain the design specifications and even exceed the design current.

Table 1. K500 Injection Line Performance

| | data 8/27/96 | CCP Reqs. |
|---|---|---|
| Ion | $^{16}O^{3+}$ | $^{16}O^{3+}$ |
| Accelerating Voltage (kV) | 30 | <30 |
| ECR Faraday Cup (pμA) | 96 | 50 |
| Spiral Inflector (pμA) | 51 | 25 |
| Transmission (%) | 53 | 50 |

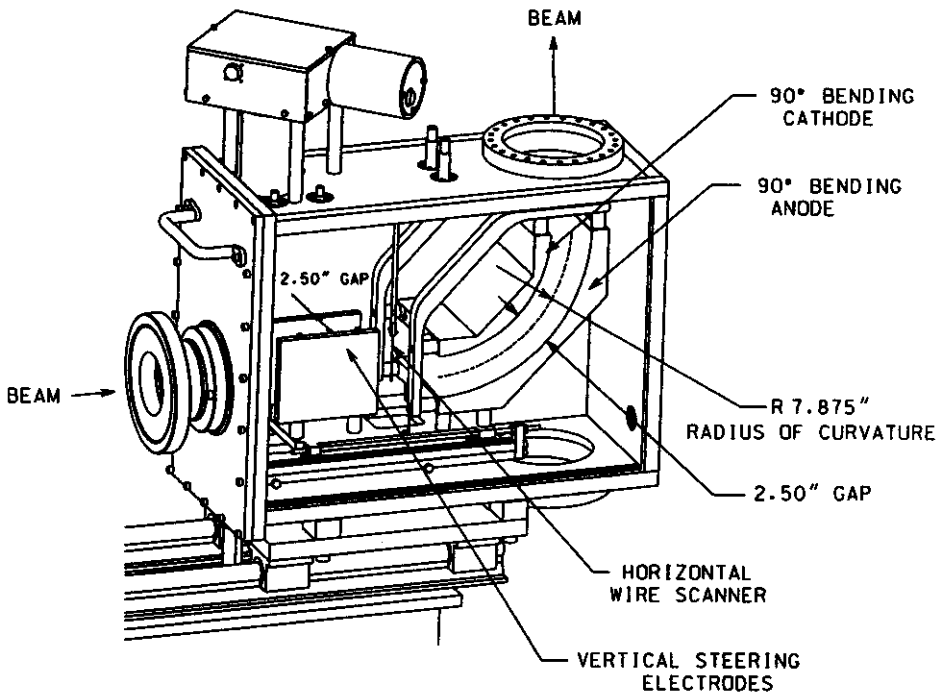


Figure 2: Electrostatic Dipole under K500

## Future Work

In September 1996 the beamline was shut down to remove and refurbish the K500 cyclotron[2]. Some additional beamline work will be completed before the K500 cyclotron is reassembled. The beamline power supplies and controls will be moved to a new balcony to make room for the K500-K1200 coupling line. Improved diagnostics to measure transverse emittance and shape will be installed, and a beamline connecting the Room Temperature ECR will be built.

## References


1. Wu, D. Lawton, F. Marti, R.C. York and T. Grimm, "ECR to K500 Injection Line for Coupled Cyclotron Project", NSCL Annual Report, p. 165 (1995)
2. Grimm, J. Bennsinger, S. Bricker, C. Compton, C. Heckman, G. Horner, F. Marti, J. Ottarson, and R.C. York, "Status of the K500 Cyclotron Upgrade", NSCL Annual Report (1996)

# A1900 QUADRUPOLES DESIGN AND CONSTRUCTION PROGRESS

J. DeKamp, A. Balint, J. Wagner, A. Zeller, and R. Zink

Significant progress is being made on the A1900 analysis line with the funding of the Coupled Cyclotron Project [1,2]. The decision was made in early 1996 to use our standard NSCL type (lower current, iron dominated) superconducting quadrupoles [3,4] for the A1900 analysis line after initial design discussions and optics calculations which considered both cos(2θ) and our standard NSCL quads as options. A drawing of the first half of the A1900 is shown in figure 1. Magnetic design of the quadrupole elements for the A1900 analysis line was completed in July and mechanical design and detailing of the magnet steel assemblies started in August 1996. In September the optimized configuration of the A1900 was finalized with magnet drawings being updated to account for changes in lengths of the various quadrupoles being used. The steel rough shapes were rebid and released to Creusot-Marrel, Inc., in mid December and are due in the spring. In addition bids were solicited on machining of the steel assemblies but have not yet been released. The multipole winding forms have been machined and winding of the multipole coils which lie within the bores of the quads has started. The multipole wire was obtained from the terminated Superconducting Supercollider project, the only cost being to have the varnish insulation applied. The manufacture of the quadrupole wire has been released to Outokumpu Superconductors OY.

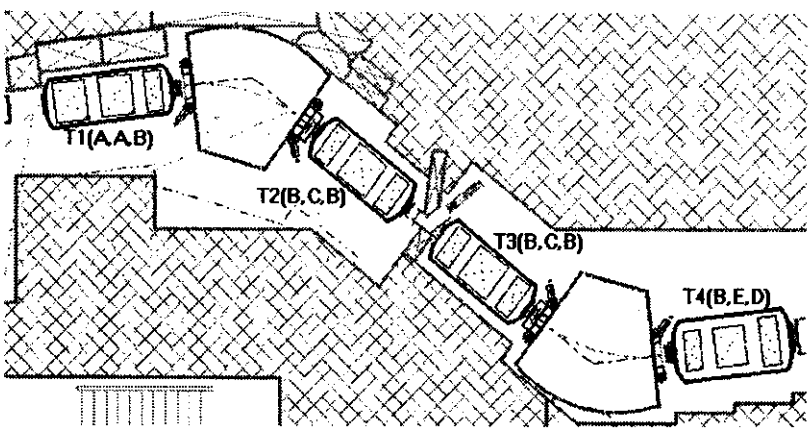


Figure 1: First half of the A1900 analysis line showing quadrupole triplets with quadrupole magnet configurations. Both B and C size quads have multipole sets mounted within their bores. The line is symmetric about the right side.

There are 3 basic quadrupole designs with different size cold apertures, 13.3 cm, 15 cm, and 21 cm, with one design being used in 3 different lengths, making a total of 5 different magnet assemblies designated A, B, C, D, and E. The quads are comparable in size to the Q1/Q2 quad doublet of the S800 spectrograph [5], but longer, the longest being about 0.7 meters (28 inches). Multipole coil sets consisting of octupoles and sextupoles are to be wound separately and mounted around the bore tube of the LHe vessel inside the bore of the quadrupoles. Only the B and C size quads will have multipole sets making their warm bore the same as the A size quads at 10 cm. The warm bore for the E size quad is 11.6 cm and the D size quad 17 cm. There will be 2 different lengths of multipoles such that they correspond to the surrounding quad lengths. Operation parameters for the quads and multipoles are given in a separate report. The quads will be packaged as triplets, 3 quads to a cryostat, in 3 different configurations. A total of 8 triplets are being built. The quad coil winding forms have been designed and are presently being machined. A new heavier duty winding table is being built for winding the coils. The

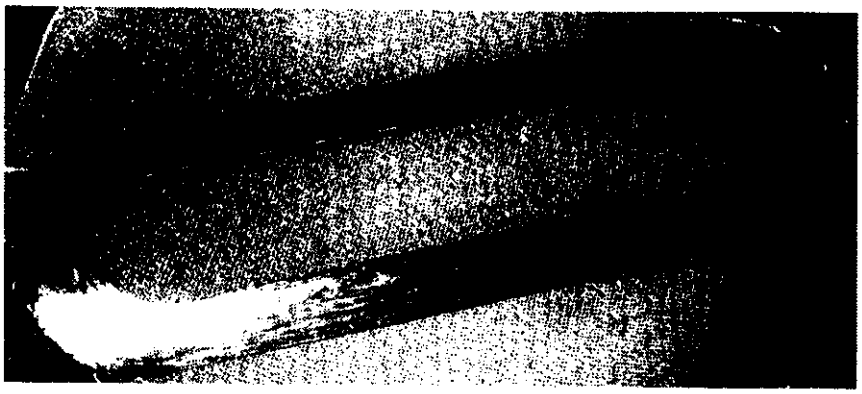

Figure 2: Wet wound superconducting sextupole coil wound from 0.6 mm dia. wire. The coil length shown lies within the bore of the B size quadrupoles.

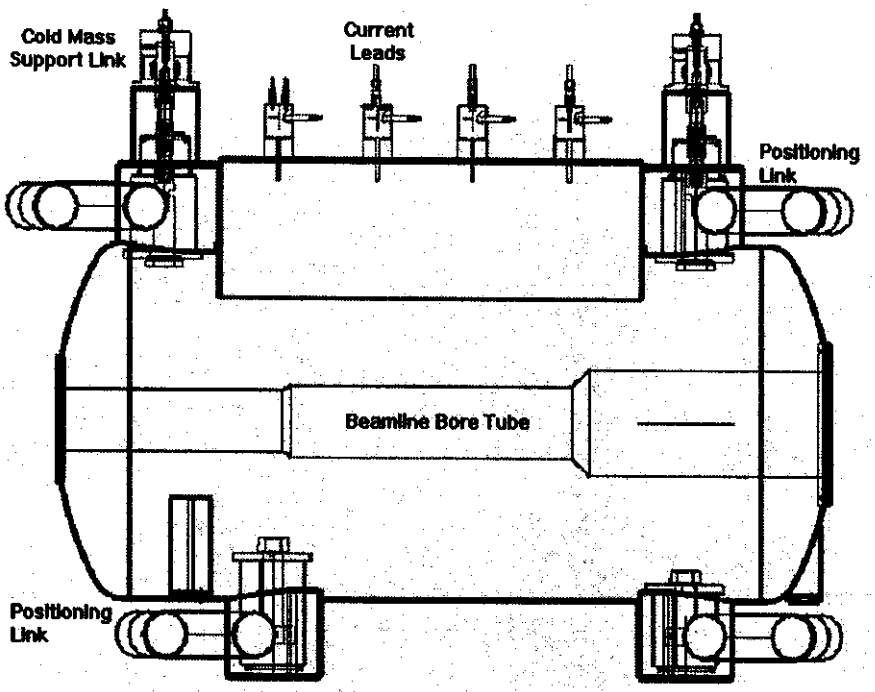


Figure 3: A view of the T4 cryostat. The cold mass is supported by the vertical S-glass link assemblies at each end. The current lead assemblies protrude vertically in the middle section. Positioning links are shown protruding horizontally at an angle.

present winding table is setup for the multipole coils. A picture of one of the coils is shown in figure 2. All coils are wet, random wound and heat cured as in our previous beamline magnets. The first triplets being built, T4 and T5, are the only triplets containing a 21 cm aperture quad. All of the triplets are being designed as batch filled devices with a 3 day holding time. The nominal design heat load is 1.1 W at a temperature of 4K giving a boiloff rate 1.6 liters/hr at the operating pressure of 1.2 atm. The cryostat design is about 40% complete with most of the conceptual design being done for all the cryostats. A conceptual view of the T4 cryostat is shown in figure 3. A rendered view of the T4 triplet magnet assembly is shown in figure 4. Completion of the first triplet assembly is expected in early 1998.

References:


1. Richard C. York, T.A. Antaya, Henry Blosser, Don Lawton, Felix Marti, D.J. Morrissey, B.M. Sherrill, John Vincent, and A.F. Zeller, "Present Status and Future Possibilities at NSCL-MSU", Proc. 4th European Part. Accel. Conf., London, England, June 1994, pp 554-556.
2. "The K500 x K1200 – A Coupled Cyclotron Facility at the National Superconducting Cyclotron Laboratory", July 1994, Michigan State University, East Lansing, Michigan, MSUCL-939.
3. J.C. DeKamp et al., "S800 Beamline Magnets and Spectrograph Quads Progress", MSU Annual Report (1995), pp 224-228.
4. A.F. Zeller et al., "Superconducting Beamline Elements for the NSCL Spectrograph", IEEE Trans. On Applied Superconductivity, Vol. 5, No. 2, June 1995, pp1032-1035
5. B. Zhang et al., "Performance of the High Gradient, Large Aperture Quadrupoles for the NSCL Superconducting Spectrometer", IEEE Trans. On Applied Superconductivity, (in press).


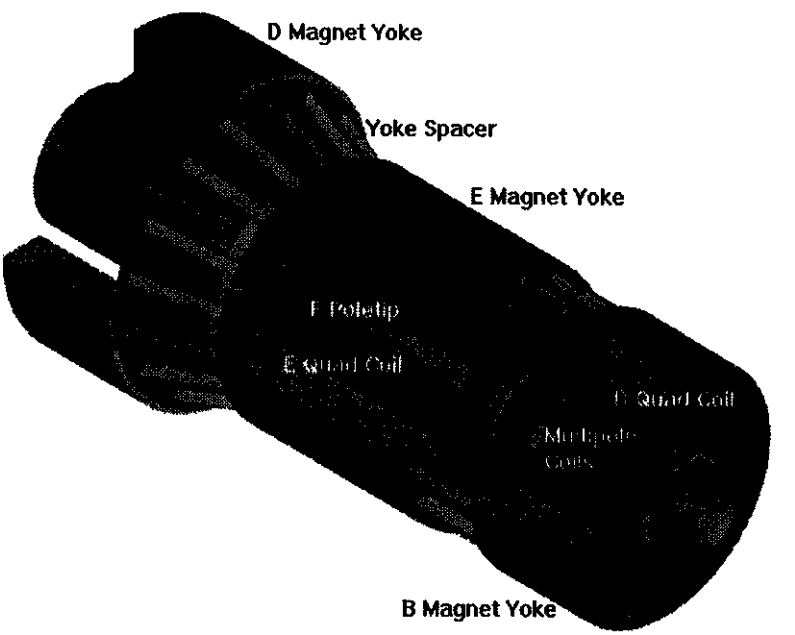


Figure 4: A rendered view of the T4 magnet assembly showing the 3 quadrupole rigidly connected to maintain alignment. The sextupol coil set can be seen beneath the circular bands, which clamp them inside the first quad. The octupole coil set lies underneath the sextupole coil set.

# A1900 BEAMLINE DIPOLE DESIGN PROGRESS

J. Wagner, J. DeKamp, A. Zeller, D.A. Johnson, and F. Marti

In April 1996 magnetic calculations [1] were completed for the A1900 dipoles. Dimensions from these calculations were used to begin the layout of the steel yoke and pole tips. This established the coil bobbin cavity in the yoke and the coil bobbin structural design began. The distance between the coils had to be increased from 11 cm in the original calculations to 16.916 cm to allow space for the LN2 shield and cryostat beam line window tubes. Magnetic calculations with the new coil and steel configuration showed an increase in current density from 6000 A/sq. cm to 6450 A/sq. cm for a 2T field in the gap. The field in the coil decreased, giving a 20% decrease in the resultant coil forces. The direction of the resultant forces changed also such that the symmetric forces across the median plane increased 34%, and the forces in the median plane of bending decreased 38%. There is no influence on the support links that are used to center the bobbin vertically, because the coil forces perpendicular to the medium plane are symmetric and relatively insensitive to small changes in coil position. The bobbin also has plenty of area in that dimension to resist the forces so that displacement and stresses are not an issue. The bobbin stiffness and horizontal support links resist the forces parallel to the median plane. The decrease of these forces allows for reduced horizontal link areas making them more cryogenically efficient, as well as smaller bobbin displacements. The bobbin walls will be 1/4 inch stainless steel plates and there will be a LHe space between the two coils. Figure 1 shows a typical cross section of the coil package. The bobbin will have a helium dewar that will have a reserved capacity of approximately 110 liters with an estimated heat load of 0.551 watts and a boiloff rate of 0.887 liters LHe/hr at 1.2 atm. Because the first dipole will be in a high radiation area and may need to be repaired the dewar was placed at one end of the magnet (Figure 2) and could not overhang the upper yoke for this would cause difficulties in disassembly if the magnet ever needed repair. Increasing the distance between the coils meant there had to be an increase in the thickness of the pole tips and center yoke steel. The additional steel brought the total weight of the dipole magnet to approximately 54 tons. Design of the coil bobbin package will be completed early in 1997.

A design for a coil-winding fixture is approximately 50% complete. The coil cross section dimensions are 3 cm by 5 cm and will be wound in an orderly procedure. It will be a potted coil with a layer of epoxy coated paper between each layer. Since the coils are similar in size to the S800 spectrograph dipole coils the same turntable will be used to wind the coils for the A1900 beamline dipoles.

Ten G-10 tension links (8 vertical and 2 horizontal), similar to those used in the S800 quadrupole triplets [1] will be used to support and position the coil bobbin inside the cryostat. The four upper vertical links will carry a load of about 1500 lbs. each with the other six links used primarily for positioning the coil. Four horizontal G-10 tube compression links will also be needed to counteract outward coil forces during magnet operation. Each compression link will need to support 5,000 lbs.

The LN2 shield design is roughly 40% complete. There will be two LN2 dewars brazed to the outside copper plates along the curved and straight sections of the shield. Their construction will consist of three 1" x 3" stainless steel rectangular tubes (Figure 1) and will hold about 20 liters of LN2. Shield design should be completed by July 1997.

The cryostat design is nearly complete except for the upper dewar section where cryogenic lines and current leads will be connected. The final design of the A1900 beamline dipole should be completed by October 1997.

Since the total magnet weight of approximately 54 tons exceeds the weight limit of our crane, the dipole cannot be moved from its assembly area to its place in the beamline in one piece. The first step will be to place and position the lower yoke and lower center yoke slabs in the beamline. Next, the cryostat/pole tip assembly will be positioned on the lower yoke slab. The remaining upper yoke and center yoke slabs will then be installed.

## References


1. D.A. Johnson, F. Marti: "Magnetic Calculations of the A1900 Dipole I." April 1996
2. J. Wagner, J. DeKamp, A. Zeller, S. Alfredson, R. Swanson, R. Zink, B. Zhang: "S800 Beamline Magnets and Spectrograph Quads Progress Report," NSCL 1995 Annual Report


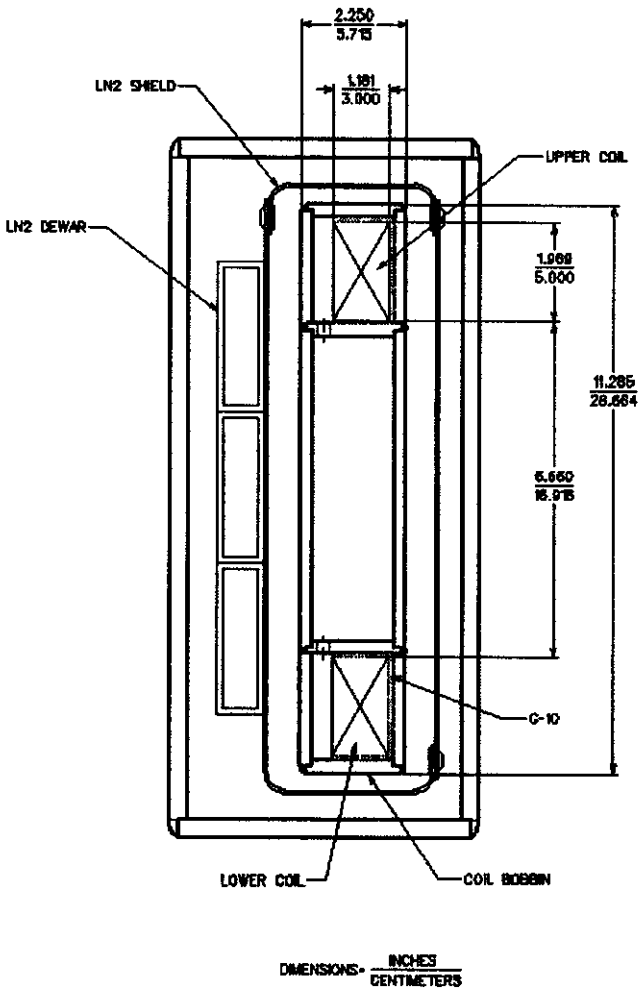


Figure 1: Typical cross section of A1900 beamline dipole cryostat, LN2 shield and coil bobbin.

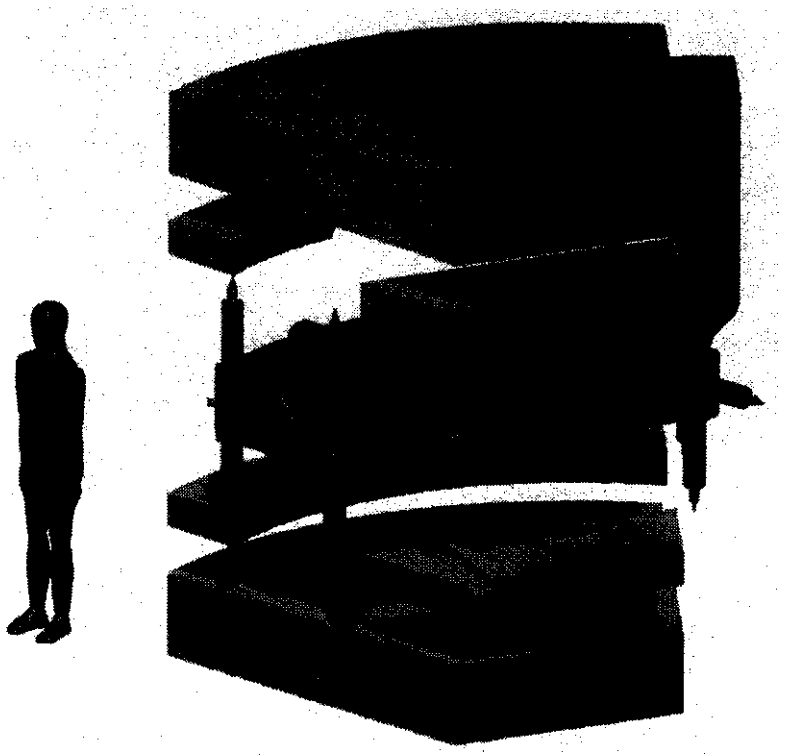

Figure 2: Exploded view of A1900 beamline dipole showing cryostat assembly and steel yoke slabs.

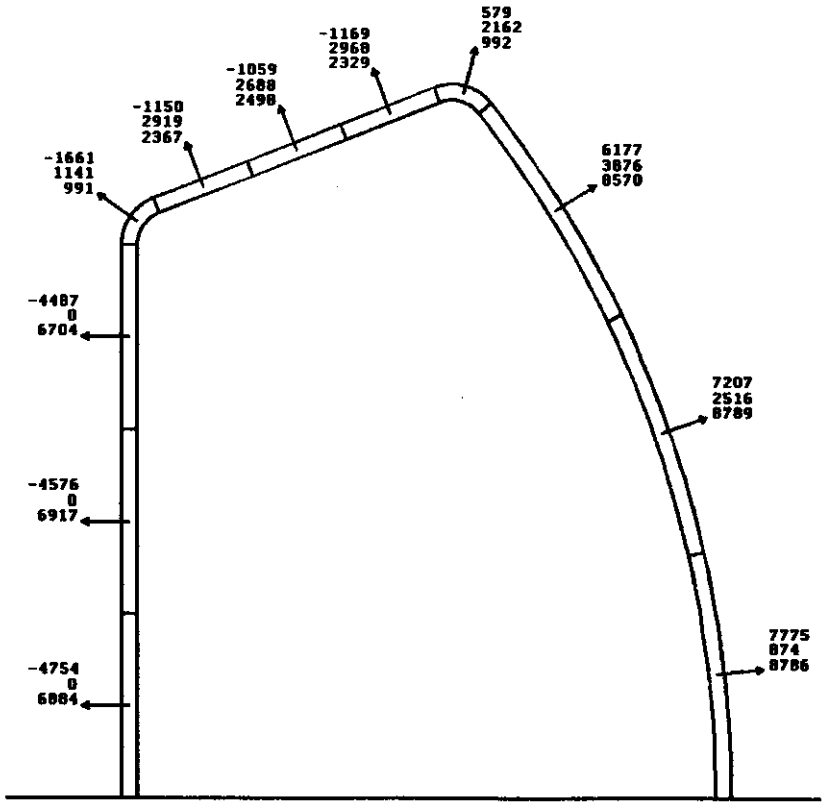


Figure 3: Top view of the dipole coil with forces in Newton's. The three numbers correspond to Fx, Fy, Fz with the z axis vertical coming out of the plane and x pointing to the right.

# TRACKING STUDIES AND PERFORMANCE SIMULATIONS OF THE NSCL A1900 FRAGMENT SEPARATOR

X. Wu, D.J. Morrissey, B.M. Sherrill, R.C. York, and A.F. Zeller

**Abstract**

At the National Superconducting Cyclotron Laboratory (NSCL), secondary beams of often short-lived radioactive nuclei are produced by the technique of projectile fragmentation where a primary beam impinges on a thin target to produce a broad spectrum of isotopes with near-beam velocity. As a major element of a recently funded upgrade of the NSCL facility, an increased capacity fragment separator used to select a particular isotope will be constructed. The key features of the new fragment separator include a high rigidity (6.3 T-m) and large acceptance with a solid angle of 8 msr, momentum acceptance of ±3%, and an energy resolution of 0.1%. Tracking studies and machine simulations have been done to verify the optical stability and performance of the lattice. The results of these studies, including simulations of magnet misalignment and magnetic field errors, are presented in this paper.

## Introduction

World-wide there are significant physics programs which use ion beams of radioactive species as a unique tool to support research in nuclear structure and nuclear astrophysics research. Two complimentary processes are used to produce the radioactive beams. A technique called Isotope Production On-Line (ISOL) stops a primary, non-radioactive beam in a thick production target. The radioactive species produced are then transferred to an ion source where they are ionized and accelerated to final energy. A second technique called Projectile Fragmentation uses a primary, non-radioactive beam on a thin ($\Delta E/E \cong 10\%$) production target. In this case, the radioactive species produced have nearly the velocity of the primary beam and a downstream magnetic transport system (fragment separator) is used to select a particular radioactive species. The Projectile Fragmentation technique is used at the NSCL [1,2].

The projectile fragment separator is used to select the specific radioactive species by a two step process. Downstream of the production target, the mixture of primary and secondary ions is selected for Br with an aperture system at a high-dispersion point. (See Figure 1.) Since energy loss is proportional to the square of the projectile atomic number, the isotopic selection is achieved by passing the Bρ-selected and dispersed ions through a wedge-shaped energy degrader. The remainder of the separator optics is then used to complete the isotopic separation. The nature and thickness of the production target and the energy degrader, as well as the sizes of the momentum apertures are parameters that are adjusted to control the secondary beam intensity and purity.

## Optics

The fragment separator rigidity requirements are set by the primary beam energy and the fact that even fully stripped neutron-rich ions lighter than the primary beam will require a higher rigidity than that of the primary beam. At the NSCL, the K1200 cyclotron and the capacity of the following beam switch yard have set the design rigidity at 6.3 T-m or ~30% greater than that of the K1200 cyclotron.

In addition, the kinematics of the secondary beam production require a large solid angle and momentum acceptance to achieve efficient capture of the radioactive species. A small magnification and large dispersion are desirable in the dispersive, horizontal plane (x) to achieve a high momentum

resolution for the Bρ selection. A small beam size and resulting larger angular spread are desirable in the vertical (y) plane to minimize the effect of multiple scattering in the energy-degrading wedge used for isotopic separation. The configuration of the planned, A1900 fragment separator is shown in Figure 1. Basic design specifications are given in Table1.

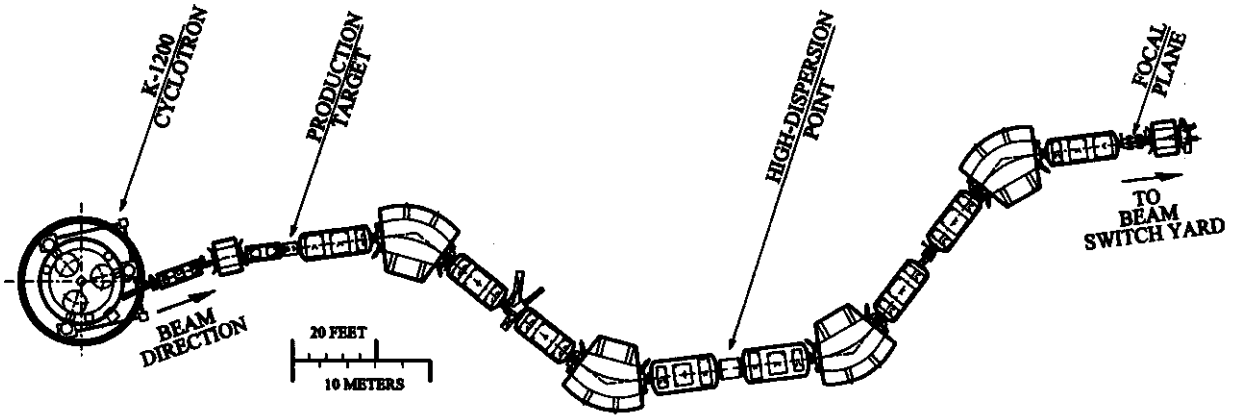


Figure 1. Layout of the proposed A1900 fragment separator.The overall system (production target to focal plane) is a unit transfer.

The initial secondary beam emittance at the production target position compatible with the A1900 admittance will be 25 π mm-mrad (0.5 mm x 50 mrad) and 20 π mm-mrad (0.5 mm x 40 mrad) for the horizontal (dispersive) and vertical planes respectively. These values provide the 8 msr solid angle specified in Table 1.

The first-order lattice functions are given in Figure 2. The lattice uses 24 quadrupoles configured in eight triplet packages, and four 45° dipoles in a reverse bend geometry so that the incoming and outgoing beams are coaxial.

## Simulations

Since many of the quadrupoles will have a relatively poor aspect ratio (length:aperture = ~2.2:1) a 6$^{th}$-order map generated by COSY INFINITY [3] was used to evaluate higher-order correction schemes and to track particles to determine transmission, resolving power, beam phase space, and error sensitivity.

Table 1. First-order, A1900 design parameters.
*Resolving power = dispersion/(initial spot size x magnification).

| Parameter | Specification |
|---|---|
| Solid Angle | 8 msr |
| Rigidity | 6.3 T-m |
| Momentum Acceptance | ±3% |
| Intermediate Image (2) | |
| Magnification R11/R33 | 2.04/0.75 |
| Resolving Power* | 2915 |
| Dispersion | 5.95 m |
| Focal Plane | |
| Magnification (R11/R33) | 1.0/1.0 |

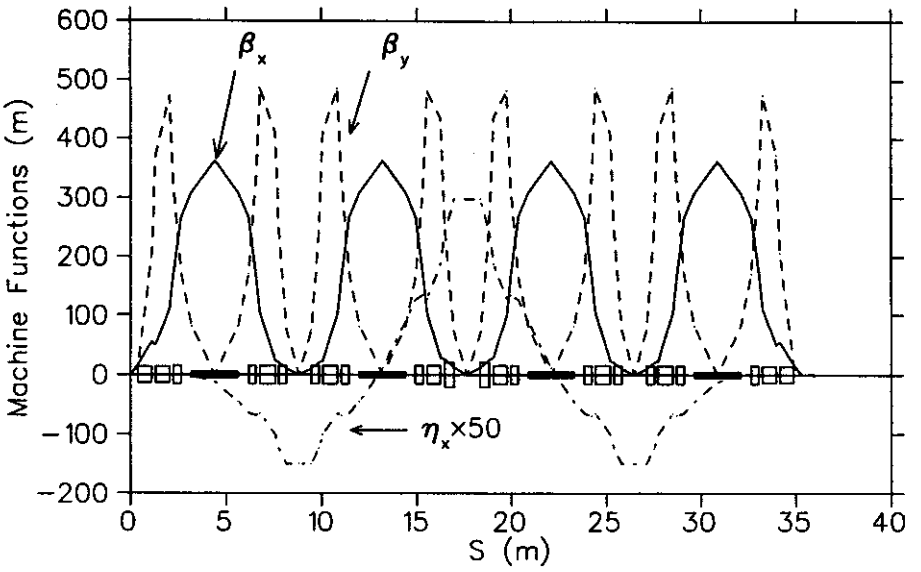


Figure 2. Lattice functions of the A1900.

The optical properties were evaluated by tracking 3,600 particles consisting of 400 particles uniformly populating the initial phase space for nine momenta values (±3%, ±2.5%, ±2%, ±1%, and 0%). Particle loss was considered at each magnet aperture and the phase space of the surviving particles was evaluated at the lattice mid-point and at the focal plane. Of the phase space delineated (8 msr and $\Delta p/p = \pm 3\%$), ~94% and ~92% survived to the lattice mid-point and the focal plane, respectively. The energy-degrader isotopic separation was not modeled in these simulations.

Due to the large momentum spread (±3%) and divergence (±50 mrad (x) and ±40mrad (y)) of the secondary beams, the higher-order aberrations are significant. The dominant 2nd-order aberrations are the chromatic terms x|x'd and y|y'δ. Six families of sextupoles were used to minimize all 2nd-order geometric and chromatic terms. The phase space generated by using the corrected 2nd-order map is given in Figure 3 for the lattice mid-point and Figure 4 for the focal plane. The maximum sextupole magnetic field required was 2 kG. Effort is now underway to provide a similar 3rd-order correction scheme.

Magnet alignment and mispowering errors were evaluated by applying the appropriate errors assuming a Gaussian distribution (±2s) for each error and using particle tracking to determine the performance degradation as a function of the s value. A degradation of 5% in the resolution was taken as the criteria for these specifications. As a result, the full-range, misalignment specifications have been set at ±0.5 mm for the transverse positions, ±0.5 mrad angular rotation about the beam axis, ± 5 mm longitudinal position, and ±10 mrad angular rotation about an axis perpendicular to the beam axis. Similarly, the full-scale ripple specifications have been set at $\pm 10^{-4}$ for the dipole and quadrupole and $\pm 10^{-3}$ for the multipole power supplies.

**Hardware**

Of the 24 quadrupoles, 16 have multipole packages consisting of a sextupole and octupole pair. The half-lattice, symmetric about the mid-point is: (QA-QA-$QB^M$) - B - ($QB^M$-$QC^M$-$QB^M$) - ($QB^M$-$QC^M$-$QB^M$) - B - ($QB^M$-QE-QD) where QX represents a quadrupole type, $^M$ denotes those quadrupoles with multipole packages, ( ) delineates the triplet package, and B specifies a bend. Table 2 lists the primary magnetic specifications for the quadrupoles. For all magnets, the magnetic field shapes are determined by the iron configuration and the current coils are superconducting. The dipoles have a length of 2.5 m, a maximum pole-tip field of 2 T, and a good-field region of ±10 cm (x) and ±4.5 cm (y).

## References


1. "The K500⊗K1200 – A Coupled Cyclotron Facility at the National Superconducting Cyclotron Laboratory", July 1994, Michigan State University, East Lansing, Michigan, MSUCL-939.
2. York et. al., "Proposed Upgrade of the NSCL", IEEE Particle Accelerator Conference, Dallas, TX, p. 345, (1995).
3. Berz, "User's Guide and Reference Manual for COSY INFINITY", MSUCL-977, Michigan State University, 1995


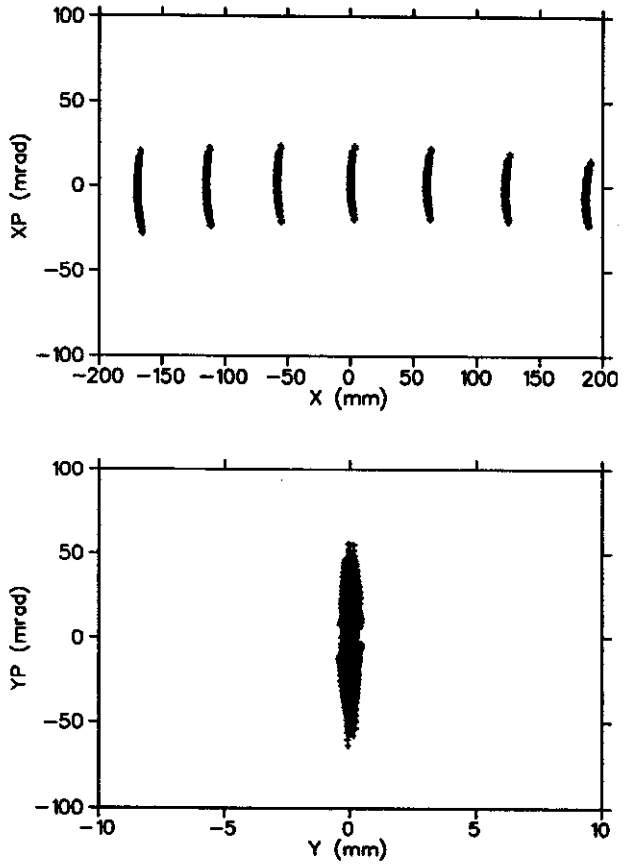


Figure 3. Transverse phase space for particles tracked through the corrected 2nd-order A1900 lattice from target to the high-dispersion mid-point.

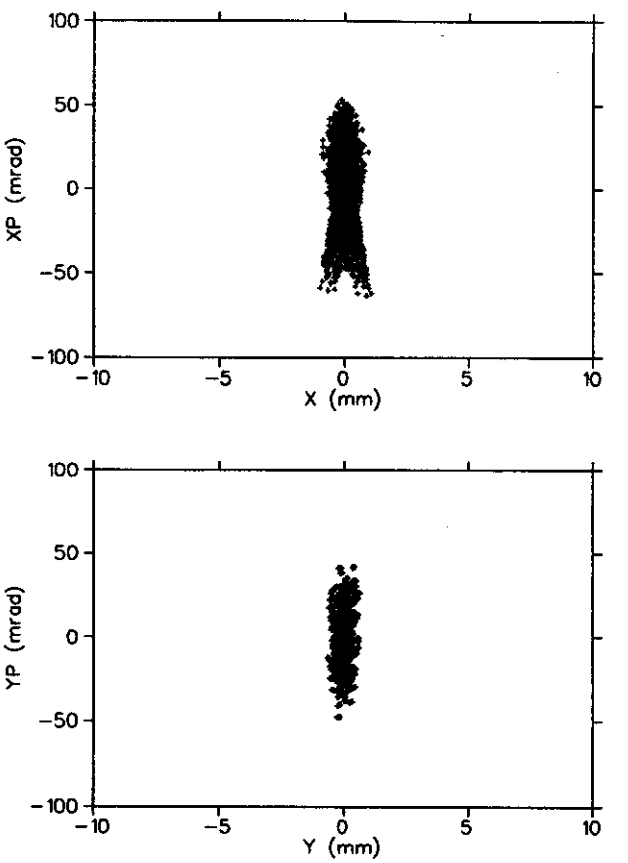


Figure 4. Transverse phase space for particles tracked through the corrected 2nd-order A1900 lattice from target to the focal plane.

| Type | # | Effective Length (cm) | Pole Tip Radius (cm) | Warm Bore Radius (cm) | Max. Pole-Tip Field (kG) |
|---|---|---|---|---|---|
| QA | 4 | 72.3 | 13.3 | 10.0 | 22.1 |
| QB | 12 | 40.0 | 15.0 | 10.0 | 20.7 |
| QC | 4 | 79.0 | 15.0 | 10.0 | 22.1 |
| QD | 2 | 48.6 | 21.0 | 17.0 | 23.1 |
| QE | 2 | 70.0 | 15.0 | 11.6 | 24.1 |

Table 2. A1900 quadrupole parameters.

# RECENT DEVELOPMENTS IN ECR ION SOURCE TECHNOLOGY AT THE NSCL

R. Harkewicz and D. Cole

A summary of recent developments in ECR ion source (ECRIS) technology taking place at the NSCL is reported here. New techniques have been put into operation at the NSCL for the efficient production of ECRIS beams from solid materials. This includes the design and construction of a miniature, low-power ECR oven and a new technique for the efficient production of rare and costly isotopically enriched calcium beams from calcium oxide material. Also, further investigation and use of the direct ion sputter technique is reported. In addition, we report on (1) improved source performance through the implementation of new source hardware; (2) continuing developments in accelerator mass spectrometry (AMS) studies at the NSCL using ECR ion sources; (3) collaborative research and work in ECRIS technology with other laboratories; and (4) planned ECRIS upgrades and R&D during the next few years.

## I. New Techniques for the Production of Ion Beams from Solid Materials

During the past year major time and effort has been devoted at the NSCL to increasing our capabilities for developing new and higher intensity ion beams from solid materials. The importance of having this capability is very apparent considering that at standard temperature and pressure (STP), of the eighty-three stable elements eleven of these exist as gases, four as liquids, and the remaining sixty-eight as solids. Clearly, having the capability to produce high quality, high intensity ion beams from the solid elements is vital to continuing a strong NSCL nuclear science program. Most notably, we have recently succeeded in producing high quality ion beams from Be, Ti and $^{48}$Ca.

During the recent past, two new methods have been implemented at the NSCL for producing ion beams from solid materials and with much success. The first method, the direct ion plasma sputtering technique [1], has proven to be a very simple and successful method for producing ion beams with the NSCL room temperature ECR (RTECR) ion source from a variety of solid elements. Basically, it consists of placing a negatively biased metal sample, introduced through one of the RTECR source's radial ports, just outside of the ECR plasma boundary (the sample is biased typically from -500V to -1200V). Positive ions on the edge of the inside plasma boundary (supplied by a support gas) are accelerated into the sample and sputter a small quantity of the metal sample into the plasma where it is ionized through the ECR process. It has been used, to date, at the NSCL to produce very stable and relatively intense beams of Ti, V, Cr, Mn, Fe, Co, Ni, Mo, Pd, Ag, Cd, Au and U. Small samples of isotopically enriched material (for example $^{46}$Ti and $^{110}$Cd), placed within a containing holder, have also been successfully sputtered. It should be noted that the direct ion sputter technique may prove useful for developing beams from additional solid elements not listed above. These will be attempted when the experimental needs arise.

As a second method for producing ion beams from solid materials, a miniature, low-power oven capable of reaching temperatures of 1400 C has been designed and built for use with the RTECR [2]. Fig.1 shows a detailed cross-sectional view of the RTECR oven. Compared to the direct ion sputter technique, the oven is especially useful for producing beams from materials that do not sputter well and for very small isotopically enriched samples. The oven is an adaptation of the very successful micro-oven designed and used by the Grenoble group in their Caprice ECR ion source [3,4]. The small size of the RTECR oven allows it to be placed entirely within one of the RTECR source's radial ports which

results in excellent coupling of solid vapors into the ECR plasma and thus minimal material usage rate. The oven and its orientation with respect to the source is shown in Fig. 2.

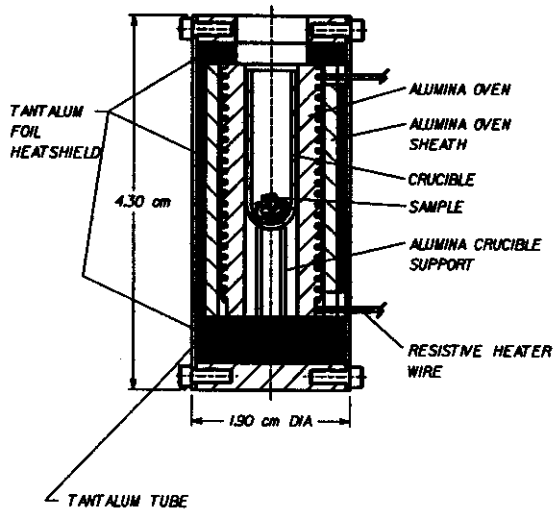


Figure 1: Detailed cross-sectional view of the miniature RTECR oven.

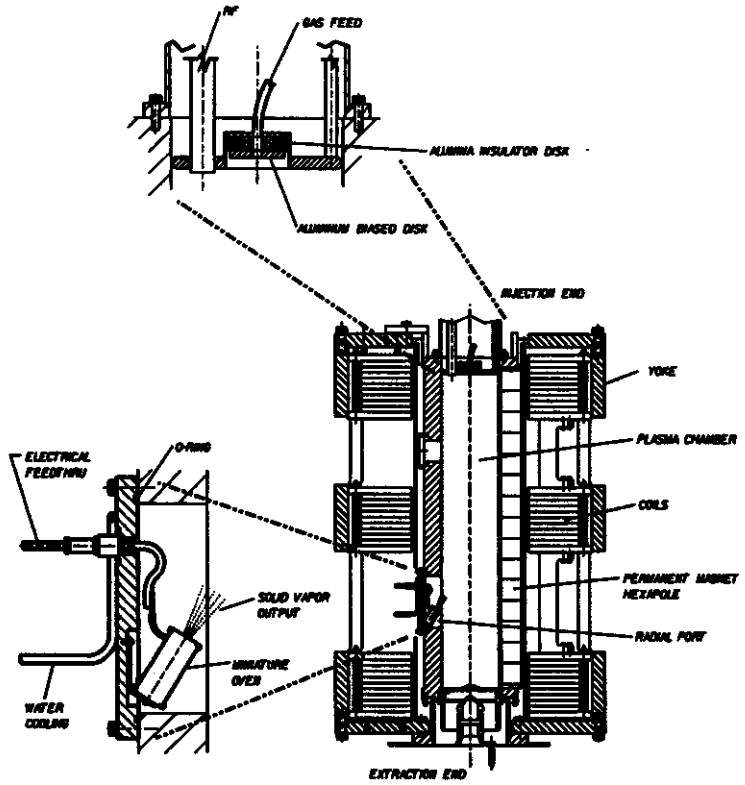


Figure 2: Cross-sectional view of the MSU-NSCL RTECR ion source showing the miniature oven mounted within one of the source's radial ports. Figure also shows aluminum biased disk which replaces original first stage.

To date, the oven has been used at the NSCL to produce beams from Li, Be, B (using $B_2O_3$), Au, and isotopically enriched $^{48}Ca$, $^{58}Fe$, and $^{110}Pd$. The oven design allows the use of very small sample sizes

and very small material usage rates. For example, the costly $^{58}Fe$ sample was below 10mg in size and its material usage rate was approximately 0.03mg/hr. Most notably, the oven has been used to produce excellent $^{48}Ca$ beams employing a new technique [2]. The technique involves the on-line reduction, by zirconium, of isotopically enriched $^{48}CaO$. This technique has resulted in very stable and longterm (run times of over one week) $^{48}Ca$ beams with intensities as high as 25pnA being extracted from the K1200 cyclotron (70MeV/A using $^{48}Ca^{12+}$) with a material usage rate of below 0.1mg/hr. This technique is especially useful considering the high cost of isotopically enriched $^{48}Ca$ and the difficulties associated with handling small quantities of calcium metal (rapid oxidation).

A similar oven has been built and successfully tested for solid beam production with the NSCL superconducting ECR (SCECR) ion source. Since the SCECR has no radial ports, the oven has been designed to be mounted axially in the injection region of the source as shown in Fig. 3. Since the ion source is "vertical" in its spatial orientation, the design of the oven demands that samples which liquify before reaching required vapor pressure temperatures, such as Pb and Au, be adequately contained in a small oven crucible without spilling down into the ECR plasma chamber and still allow vapors from the solid to freely enter the plasma. Our "inverted" SCECR oven and square shaped crucible designs, shown in Fig. 4, have successfully met these demands. A recent high-energy Au development run using the SCECR successfully produced 50MeV/A ($^{197}Au^{42+}$) and 55MeV/A ($^{197}Au^{44+}$) beams being extracted from the K1200 cyclotron with intensities of approximately 1.5ppA.

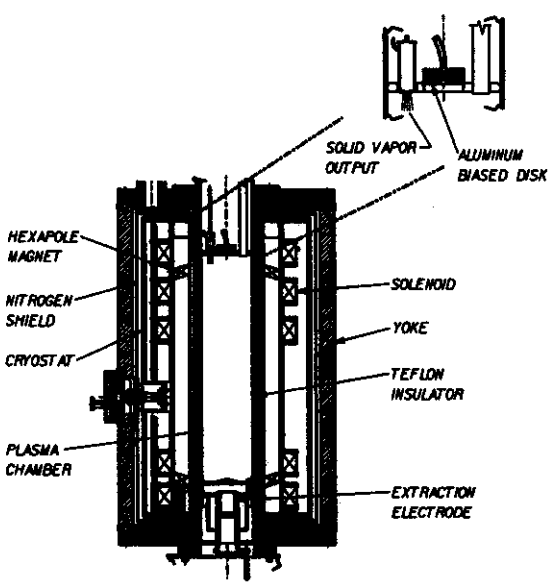


Figure 3: Cross-sectional view of the MSU-NSCL SCECR ion source showing the "inverted" oven mounted axially in the injection region of the source. Figure also shows aluminum biased disk which replaces original first stage.

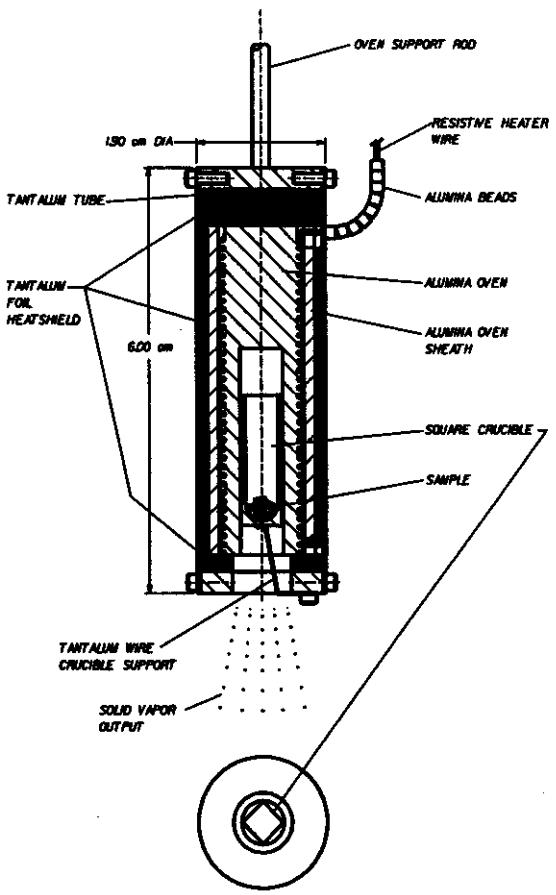


Figure 4: Detailed cross-sectional view of the miniature "inverted" SCECR oven.

Presently, the direct ion sputter technique is also being investigated for use with the SCECR. One option is to have the sputter samples introduced axially in the injection region of the source. We have

observed that finding the correct location of the sputter sample relative to the plasma in this axial orientation is more of a challenge as compared to the RTECR radially introduced sputter samples. A second option is to simulate a radially introduced sample by running an insulated (using $Al_2O_3$ tubing) wire down the side of the plasma chamber then terminating the wire with a 90 bend to which a sputter sample is attached. The insulated wire is oriented to minimize plasma interaction. This second option appears to be more promising and has already been used to develop Ag and Au beams. Presently, we are still perfecting the sputter technique for use with the SCECR.

**II. Improvements in Source Performance Through the Implementation of New Hardware**

In an effort to improve performance, new hardware has been installed in the RTECR and SCECR ion sources during the past year. It has been demonstrated [5] that an enhancement of ECR ion source performance can be achieved through the application of plasma chamber aluminum coatings. At the NSCL we have designed evaporation hardware which has allowed us to coat (online, without removing the chamber from the ion source) both the RTECR and SCECR plasma chambers with a very thin layer of aluminum. Some evidence of improved source performance has resulted from these coatings. In addition, the copper extraction orifice of the SCECR ion source has been replaced with an aluminum one in an effort to further take advantage of this technique.

Also during the past year, both on the RTECR and SCECR ion sources, first stage hardware has been removed and entirely replaced with an aluminum biased disk. This is shown in Figs. 2 and 3. Since the placement of the disk and removal of the first stage hardware, performance of both sources appears to be as good, and better, as compared to the past. In addition, this modification allows for simpler source operation and is more compatible with the SCECR oven hardware described above.

**III. Continuing AMS Program at the NSCL Using ECR Ion Sources**

We are continuing to develop an accelerator mass spectrometry (AMS) program using ECR ion sources at the NSCL [6,7] in collaboration with W. Kutschera *et al.* from the University of Vienna, Austria. The SCECR is being used, along with the K1200 cyclotron and A1200 separator, in a series of measurements which are currently determining and comparing the amount of $^{81}Kr$ in present-day atmospheric krypton (estimated to be approximately one part in $10^{13}$) and $^{81}Kr$ in samples of pre-nuclear testing (*pnt* ) atmospheric krypton. This is very exciting research as $^{81}Kr$ is a cosmogenically produced radionuclide (the recent tests comparing present day and *pnt* samples will determine if any is anthropogenically produced), having a half-life of 210,000 years, which has the potential of developing into a reliable absolute chronometer for dating old ice in polar ice caps and ground water in the age range from 50,000 to 1,000,000 years. In order to meet the demanding constraints required to perform these AMS measurement successfully, a special gas handling system has been designed and built at the University of Vienna for use with the SCECR. The system includes a cryogenic trap for eliminating unwanted trace contaminants (specifically $^{81}Br$). In addition, the system allows for the rapid change of multiple samples via computer control. The most recent AMS measurement at the NSCL was carried out in December 1996 and data collected during that time period is presently being analyzed.

**IV. Collaborative Research and Work in ECRIS Technology with Other Laboratories**

In the recent past, collaborative ECR ion source research has been carried out between the NSCL and a number of other laboratories.

The SCECR has been used to further investigate frequency and magnetic field scaling in ECR ion sources with our collaborators from INFN Catania, Italy [8]. Specifically the High-B mode of operation [9], where a much higher axial and radial magnetic field than is required for electron cyclotron resonance is used and which has resulted in the impressive performance of the SCECR and

other ECR ion sources [10,11], has been investigated in greater detail. The SCECR was operated at a microwave frequency of 2.45GHz (the source typically operates at 6.4GHz) in an effort to determine the degree to which the High-B mode can be extended. The conclusion of these most recent tests indicates that improvements can be achieved with a radial magnetic field four to five times higher than is needed for resonance. In addition, increasing the source microwave frequency is beneficial provided that a high enough magnetic confinement field can be maintained. These tests indicate that even higher performance can be expected from the 6.4GHz SCECR if the field of the source's hexapole magnet can be increased. Presently, the hexapole magnet can only achieve one-third of its design field before quenching. Plans to rebuild the hexapole are underway and the above tests indicate that we can expect much improved performance from the higher field hexapole. Due to the success of the High-B mode, plans are presently underway to upgrade the NSCL RTECR to match the high mirror and hexapole fields of the SCECR, as was done with the Texas A&M ECR ion source [10,11].

During the past year, the NSCL has also been very actively involved with other laboratories in the development of ECRIS beams from solid materials. Our miniature oven technology, described above, has been introduced to and adopted by ion source groups at Argonne ATLAS, the Texas A&M Cyclotron Institute, and the University of Jyväskylä Accelerator Laboratory.

We are currently developing a working collaboration with The Institute of Nuclear Science (ATOMKI), Debrecen, Hungary. It is the goal of this ATOMKI / NSCL collaboration to bring about a mutual exchange of ideas and technology from which both laboratories will benefit. In the very near future, we hope to introduce and help put into operation NSCL oven and sputter technology for the production of beam from solid materials in the new ATOMKI ECR ion source [12]. We also hope to study and better understand ECRIS plasma phenomenon, particularly related to the direct ion sputter technique, using the ATOMKI developed TrapCAD code [13]. The TrapCAD code will also be used to optimize the design of the NSCL upgraded RTECR ion source.

## V. Future Plans

As was stated above, plans are underway to rebuild the superconducting hexapole magnet on the SCECR. In addition to allowing us to further explore the High-B mode of operation at the present operating frequency of 6.4GHz, the new hexapole will allow us to investigate operating the SCECR at 14GHz (for which an RF transmitter already exists).

We are also presently in the design phase of a new RTECR ion source that will operate in the High-B mode. Fabrication of source parts should commence in 1998. This new source should have both the high performance of the present SCECR and the versatility, for example with ovens and sputter hardware, of the present RTECR.

## References


1. Harkewicz *et al.*, Rev. Sci. Instrum. **66**, pp. 2883-2887 (1995).
2. Harkewicz, Rev. Sci. Instrum. **67**, pp. 2176-2178 (1996).
3. Hitz *et al.*, Proceedings of the 11th International Conference on ECR Ion Sources, KVI-Report 996, Groningen 1993, pp. 91-96.
4. Hitz *et al.*, Proceedings of the 12th International Workshop on ECR Ion Sources, RIKEN Report INS-J-182, Saitama 1995, pp. 126- 130.
5. Xie *et al.*, in Ref. 4, pp. 24-28.
6. Kutschera *et al.*, Nucl. Instrum. Methods B92, pp. 241-248 (1994).
7. Collon *et al.*, Nucl. Instrum. Methods (in press).
8. Gammino *et al.*, Rev. Sci. Instrum. **67**, pp. 4109-4113 (1996).
9. Ciavola *et al.*, Rev. Sci. Instrum. **63**, pp. 2881-2882 (1992).
10. May *et al.*, in Ref. 4, pp. 170-173.
11. May *et al.*, Proceedings of this workshop.
12. Biri *et al.*, Nucl. Instrum. Methods (in press).
13. Vámosi *et al.*, Comp. Phys. Comm. **98**, pp. 215-223 (1996).

# A K1200 PROBE FOR 1 kW BEAMS

Peter Miller and Jim Moskalik

## Introduction

A new probe for measuring the internal and external beam current was placed in service. The probe tip is a solid copper water cooled beam stop. The probe is designed to operate at 1 kW beam power.

The main advantage of this probe is that it may be scanned through high intensity beams. It is several inches longer than the previously used 1-Finger probes in order to prevent exposure of the support insulators to the particles while scanning between internal and external beam. This makes measurement of extraction efficiency easier and safer. The operator now can optimize the tuning of the beam at high power, correcting for thermal deformations of the deflector, etc.

When the probe cooling water is not present and the probe is stationary the background noise and offset current are below 10 pA. When water is flowing the background current is 3 to 5 nA, and effective operation is limited to beam currents above about 10 nA.

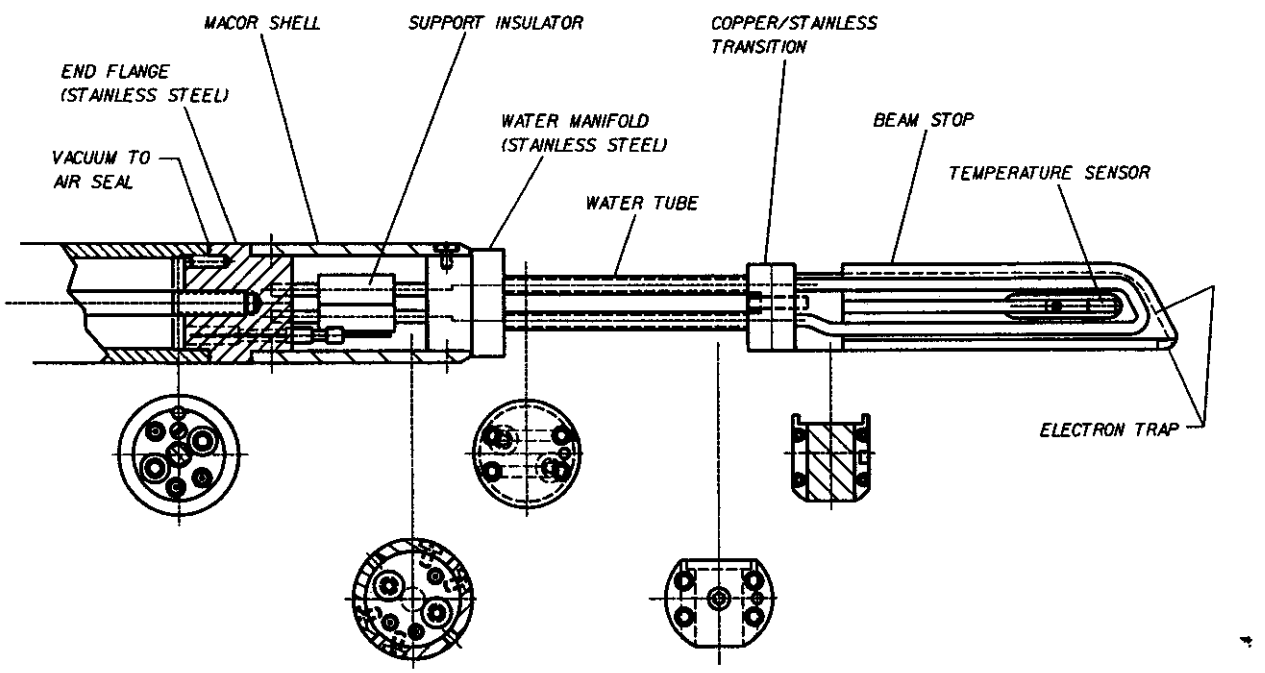


## Probe construction

The top view of the probe is seen in Fig. 1. Several cross sections are shown as well. Secondary electrons are trapped by the recessed face of the beam stop. The water cooling tubes (copper) are soldered into grooves in the top and bottom faces of the beam stop and into holes in the copper-to-stainless steel transition. The 4 tubes from this transition back to the water manifold are stainless steel.

The support insulators are ceramic tubes with stainless steel ends. They are displaced horizontally and vertically from the center axis to accommodate the tension rod and other components. All joints between stainless steel parts are welded. The Macor shell supports the bending moment of the beam stop. Otherwise the support insulators might be damaged by dynamic loads. The support insulators entirely support the weight of the probe when the clamshell halves are removed, such as for assembly and cleaning. Each half of the clamshell is secured by 4 pan head screws.

The four tubes connecting the water manifold to the beam stop leave a clear space for the beam to pass through the probe. This was done so the measured internal beam current will go to zero well before the extracted beam impacts the beam stop.

An RTD temperature sensor is held by a flat spring on the top surface of the beam stop in a groove. The sensor is about 0.75 in. from the end of the beam stop.

**Summary**

A long finger copper probe has been assembled and is providing useful data for cyclotron tuning and deflector development. It can stop 100 MeV/u $^{4}$He and 200 MeV/u N ions. The predicted power capability of 1 kW has been demonstrated with a beam.

# BEAM-VIEWING-SCINTILLATOR DEVELOPMENT

J. Yurkon and P. Miller

Transporting a heavy ion beam of appropriate quality requires the ability to visualize the beam at various points in the beamline, in some cases even within the cyclotron itself. Many phosphors have been used for this purpose, but only a few possess the required efficiency for low intensity beams and still be sufficiently resistant to radiation damage. Holland et. al. [1] have measured the efficiency and radiation hardness of phosphors in a proton beam. We have taken the results and plotted the light output in two ways. First as a function of dose with an equal beam intensity as shown in Fig. 1 and as a function of time with the beam normalized to give the same initial light output as in Fig. 2. In viewing the slopes of

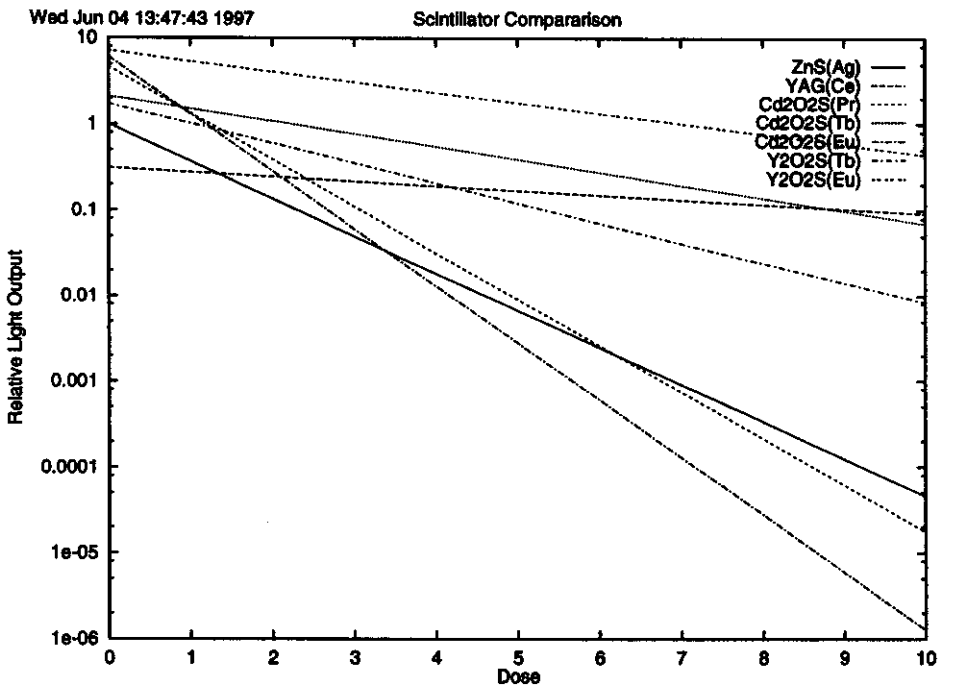


Figure 1: Light Output as Function of Dose.

the light output curves in Fig. 1 it is apparent that YAQ:Ce is the most radiation resistant. Yet its light output is the lowest of all the scintillators. It is therefore more informative to view the light output as a function of time assuming a beam current for each scintillator to normalize the initial light output. This is in fact how the scintillators are used since we can easily adjust our beam current. The results in Fig. 2 demonstrate that $Y_2O_2S$:Eu[3] is the best choice, even though it ranks second in radiation resistance.

We fabricated viewing scintillators by following the recipe of Hollerman[2]. First a 50/50 by weight solution of GR950F[4], a polysiloxane resin, and Butanol was made. Then 30% by weight of $Y_2O_2S$:Eu was added and mixed in a ball mill. This solution was then sprayed on to an aluminum plate and air dried. It was then placed in an oven and baked at 160 C for one hour. The resulting plate was then examine with a UV light source. The resulting plate did not appear as bright as we expected so the concentration of $Y_2O_2S$:Eu was increased to 60%. This yielded a bright uniform scintillator. The polysiloxane binder has proven to be easy to handle and is very radiation resistant.

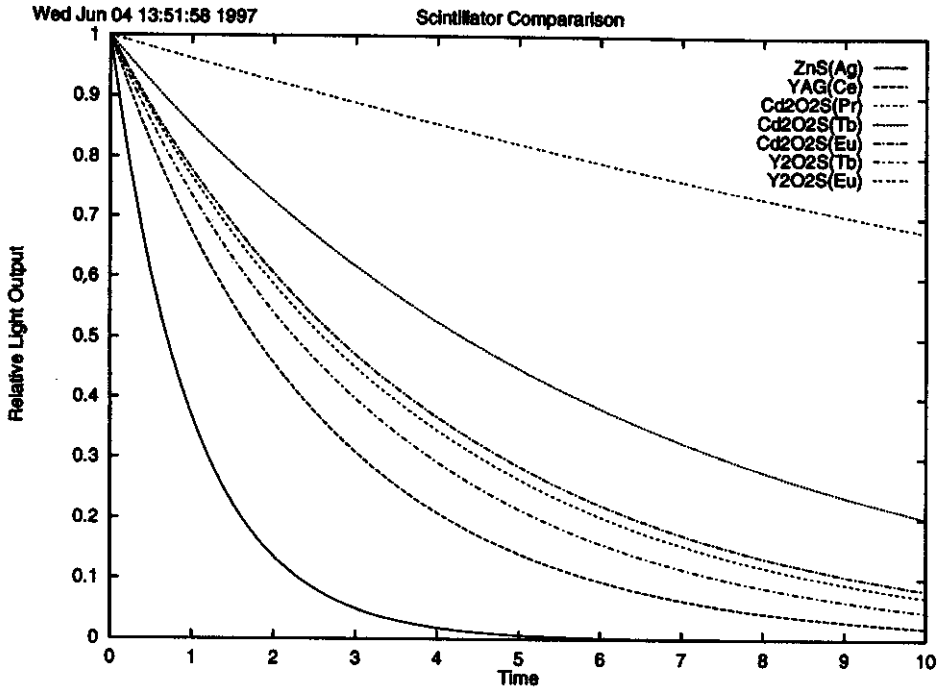


Figure 2: Light Output as Function of Time.

The scintillators have been used in beams up to Gold with little noticable degradation. Further quantitative comparisons need to be made against our standard beam viewing plates.

$Y_2O_2S$:Eu is a red phosphor which is a good match for our cameras which use CCD technology. Further tests also need to be done to see if it works as well as a blue phosphor for an Image Intensifying camera which has a standard S11 response.

## References

1. L. Holland, G. Jenkins, J. Fisher, W. Hollerman and G. Shelby, NIM (1991) 1239.
2. W. Hollerman, Investigation of Proton Induced Fluorescence from Yttrium and Gadolinium Compounds, (Disertation, Alabama Agricultural and Mechanical University, 1995).
3. Nichia America Corp., 1006 New Holland Ave., Lancaster, PA 17601.
4. TECHNEGLAS, Inc., 25875 S. R. 25 - LDP 52, Perrysburg, OH 43551.

# ESTIMATES OF RESIDUAL RADIOACTIVITY IN A 250 MeV 200 MICROAMP SUPERCONDUCTING PROTON CYCLOTRON

H. Blosser, D. Johnson, R. Ronningen, and T. Stammbach[a]

A recent paper[1] has summarized results of an extensive computer study of extraction efficiency in a 250 MeV superconducting cyclotron operating in a "multi-turn" extraction mode. This study indicated that an extraction efficiency of 97.6% could be achieved in such a cyclotron with a deflector septum of thickness 0.13 millimeters. Exploration of settings for operating values were moderately explored in this study but some additional improvement is likely with additional study; on the other hand the study did not include allowances for fabrication errors, time instabilities, etc. which would act to reduce the extraction efficiency. Noting the off-setting factors in the incomplete or neglected aspects of the study we take 97.5% as a present best estimate of the transmission efficiency of such an extraction system. The purpose of the present note is to assess the levels of radioactivity which might result from such beam loss and the difficulties which this radioactivity would pose from the perspective of necessary maintenance operations in the cyclotron.

The cyclotron which most closely resembles the compact superconducting cyclotron considered here is the original 72 MeV injector cyclotron [2]-- "Injector I"--at the Paul Scherrer Institute. This cyclotron served as the main injector for the 590 MeV meson-factory cyclotron at PSI until mid-1985 (when a new separated sector cyclotron -- "Injector II" -- took over as the ring cyclotron injector). Injector I, in the latter part of its injector years, delivered beams of up to 200 microamps to the ring cyclotron, i.e. the same current as considered here but at lower energy. In view of the extensive similarity between Injector I and the 250 MeV cyclotron considered here, we adopt a strategy of estimating radiation exposures from the 250 MeV machine by making scaling comparisons with Injector I. (A direct calculation of radiation dose from an intricate structure such as a cyclotron would be both extremely difficult and only marginally reliable.)

DOSE FOR MAINTENANCE INJ. I 1982 - 1987

| Year | Dose (mSv/a) | Operation (annual integrated charge 72 MeV) extracted | loss |
|---|---|---|---|
| 1974-81 | | | 146mAh |
| 1982 | 114 | 7510h 514mAh | 30mAh (4μA) |
| 1983 | 87 | 7384h 536mAh | 28mAh (4μA) |
| 1984 | 77 | 7477h 610mAh | 41mAh (5μA) |
| 1985 | 115 | 6251h 130mAh | 15mAh (2μA) |
| 1986 | 68 | 5595h 110mAh | 7mAh (1μA) |
| 1987 | 59 | 6272h 60mAh | 5mAh (1μA) |
| 1988 | | 6214h 190mAh | 14mAh (2μA) |
| 1989 | | 6440h 215mAh | 20mAh (3μA) |
| 1990 | | 5800h 50mAh | 5mAh (1μA) |

Table I: Selections from beam current and radiation dose records from the Injector I Operations Department of the Paul Scherrer Institute.

As the starting point of this comparison we give in Table I a summary of abstracted sections of PSI radiation exposure records for the relevant years. This Table shows the dose received by personnel

associated with maintenance operations on Injector I for the years 1982-1984 which are the years when Injector I was principally used for injecting high current proton beams in the ring cyclotron. The table shows annual hours of operation, integrated annual extracted beam, and integrated annual beam loss (as well as an approximate value for loss current). The hours of operation shown in Table I include one week per month for nuclear physics where currents were generally much lower than for the injector mode. (Total extracted charge for the three years divided by the sum of operating hours gives an average current of 74 microamps whereas for a large portion of the injector time, the cyclotron operated at up to 200 microamps extracted current -- particularly in the year 1984).

From Table I we see that the radiation dose received by the operating staff for the three years 1982 through 1984 comes to 278 mSv (total for the 3 years). This total is the sum of doses received by 48 people organized into six groups. Two of these groups received most of the dose namely a 7 person "Inj.1 Service" group and a 3 person "mechanics" group. In the year 1982, as an example, the average dose for the mechanics was 10.3 mSv and 6.1 mSv for the service group; the maximum dose received by any person in the operating staff in this year was 22 mSv. All of these doses are below the present allowed 50 mSv/year tolerance for U.S. radiation workers.

A cyclotron operating at 250 MeV of course produces higher levels of radioactivity per microamp reflecting the much higher neutron yield per microamp due to both higher cross-sections and longer range; the secondary neutrons also produce radioactivity, this latter factor being the principal source of the broadly dispersed radioactivity, which is a main source of radiation exposure to personnel.

Considering first the neutron flux we refer to Figure 7 from the work of Kahto and Nakamura[3] and note neutron yields for protons on copper (the septum material in the Injector I) of 0.101 neutron per incident ion at 72 MeV whereas at 250 MeV the yield on copper has increased to 1.21 neutrons per incident ion, i.e. larger by a factor 12. From the perspective of reduced radioactivity, carbon is a much more attractive septum material since almost no long lived radioactivity results from proton reactions on carbon. Furthermore recent tests at NSCL using a pyrolytic graphite septum have given good performance from the perspective of holding deflector voltage and handling beam power [4]. Referring again to the Kahto/Nakamura study the neutron yield of 250 MeV protons on carbon is 0.357, i.e. higher than the 72 MeV protons on copper yield, but only by a factor of approximately 3 and noting the increased extraction efficiency projected from the numerical study of Ref. 1 which projected a decrease in extraction losses of approximately a factor of 3 relative to the PSI Injector I the total neutron yield is then increased only moderately, i.e. by a factor of about 1.3.

An additional important factor at 250 MeV is the much greater range of the primary beam (63 mm in Cu vs 7.4 mm at 72 MeV); virtually no beam then stops in the septum since the bending radius decreases as the particles lose energy and the orbit then curves out of the septum and back into the internal beam space where it typically then ends up hitting the vacuum tank on the opposite wall as illustrated in Fig. 1, which is from ref. 1 and is for a copper septum, or goes into a lower energy coasting orbit as shown in Fig. 2 for the case of a carbon septum. Tungsten is another widely used septum material; Fig. 3 repeats the same set of rays as in Figures 1 & 2 but with a tungsten septum (250 MeV range of 37 mm); in this case there is increased energy loss in the septum so that 4 rays of the group of 12 actually stop in the septum and two of the escaping rays bend so sharply that they collide with the central region structures of the cyclotron (represented by the small circle in the center of the Figure). The three septum materials are all workable from the point of view of power dissipation and electric field characteristics; they will be very different in the amount of radioactivity produced and in its distribution, the heavier materials giving more radioactivity but more concentrated in the septum, which offer offsetting advantages.

To make a scaling comparison of the radiation hazard created by lost beam in the Injector I vs the 250 MeV machine we refer to the "Danger Parameter" introduced by Barbier [5] to approximately

represent the radiation hazard to personnel by taking account of many factors viz. the lifetime and penetration of emissions of the particular isotopes, the self-shielding benefit from the decaying isotope being imbedded in the stopping material, etc. Referring to Barbier's Figures on pages 339-347, we find Danger Parameter values (published values $\times 10^6$) at 50/500 MeV of 1.5/0.7, 7.0/26, and 1.8/14 for stopping in carbon, copper, and tungsten respectively for a 1 year bombardment followed by a 1 day cooling period. Linearly interpolating in the above values gives a Danger Parameter estimate at 250 MeV of 1.1, 15, and 7.2 for C, Cu, and W, and a value at 72 MeV on Cu of 7.9 for the same bombardment and cooling times. Ratios of the three 250 MeV values to the 72 MeV Cu value are then 0.15, 1.96, & 0.91 again for C, Cu, W respectively.

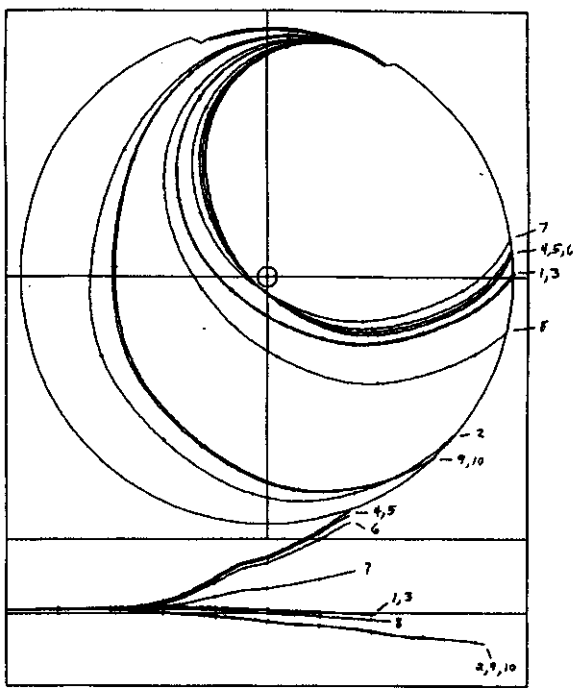


Figure 1: Top - map of selected trajectories which hit and penetrate a Copper septum of 250 micron thickness. The outer circle in the figure is the outer wall of the vacuum tank at 838 mm radius; the inset double line in the 45 degree upper arc shows the aperture of the first electrostatic deflector. Bottom - displacement from median plane vs path length for these orbits. Displacement scale is arbitrary since calculation uses linearized "z" equations; path length is marked with crosses (+) corresponding to similarly marked points in polar map at top.

Taking any of the above ratios, and noting the presumed x3 reduction in the microamps of beam lost, a maintenance radiation exposure of from 1/20 to 2/3 of that at Injector I is inferred depending on whether the lost beam stops in carbon or in copper with tungsten as an intermediate case. Which of the three septum materials is actually the optimum choice is not immediately clear, since as Figs. 1-3 indicate, the lighter carbon septum with its much longer range allows a much larger fraction of the lost beam to penetrate the septum and go on to strike some other part of the cyclotron. If the Danger Parameter advantage of carbon is then to be maintained, graphite beam catchers will need to be provided at all these more distant loss points. Shifting to the heavier tungsten septum has the effect of concentrating radioactivity in the septum vs allowing it to distribute more widely through the cyclotron; if a special device is provided to remove the septum without closeup operator actions, the tungsten septum would become the material of choice.

In conclusion, the calculations and data summarized herein strongly support the inference, that radiation exposures to maintenance personnel can be maintained at levels significantly lower than those incurred in the peak period of operation of the PSI Injector I, and well below current allowed U.S. tolerance levels.

a. Paul Scherrer Inst., Villigen, Switzerland

## References

1. "A Compact Superconducting Cyclotron for the Production of High IntensityProtons", H. Blosser, D. Johnson, D. Lawton, F. Marti, R. Ronningen, J.Vincent, Proceedings of the 1997 Particle Accelerator Conference, Vancouver, BC (in press).
2. P. Schmelzbach, Proceedings 14th Inter. Conf. on Cyclotrons p.750(1995).
3. T. Kahto and T. Nakamura, Nucl. Instr. & Methods A311(1992)548.
4. P. Miller (private communication).
5. M. Barbier, "Induced Radioactivity", North-Holland Publishing Co. (1969).

*Work supported by US National Science Foundation (PHY-9528844) and by Lockheed Martin Energy Systems (22X-SW033V).

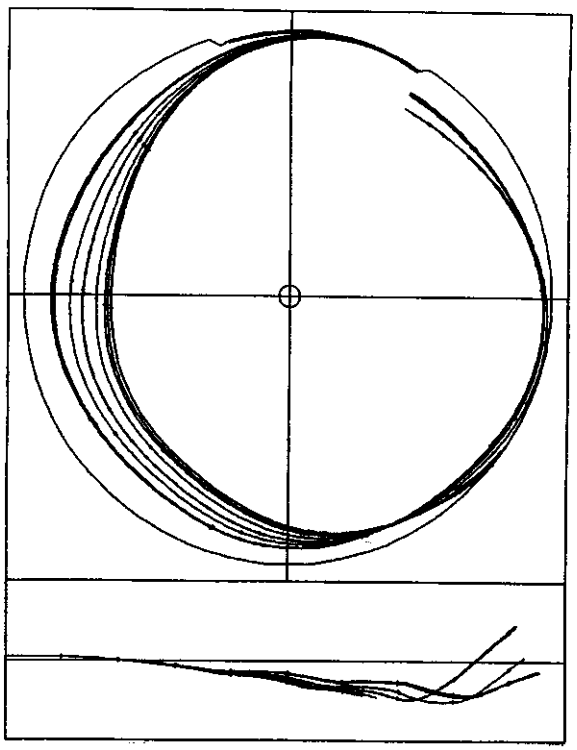

Figure 2: Same as Fig. 1 except the septum is Pyrolytic Graphite.

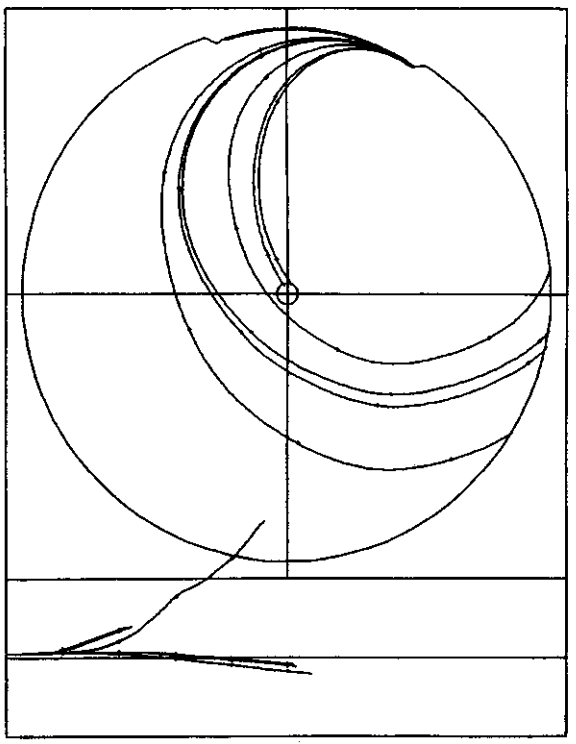

Figure 3: Same as Fig. 1 except the septum is tungsten.

# EXPOSURE AND DECAY RATES OF MOLYBDENUM AND TUNGSTEN FOILS AFTER CYCLOTRON BEAM IRRADIATION

R.M. Ronningen and P. Rossi

The electrostatic deflectors in the K1200 cyclotron currently use molybdenum (Mo) for the septum material. It has happened several times, when accelerating beams having high power densities, a Mo septum has been damaged by melting a portion of it. The vaporized activated material appears to migrate from the local damage site, leading to significant measured exposure rates from this material in several places inside the cyclotron. Personnel protection becomes more difficult because the rates can be high, the areas can be difficult to shield, and the contamination is removable.

For the coupled cyclotron project, because of increased power handling requirements, it was decided to study tungsten as a replacement for molybdenum. Tungsten (W) has the highest melting point of any element, save carbon. However, presently it appears difficult to fabricate a working septum from carbon. Therefore, we measured exposure rates from an irradiated tungsten foil as it "cooled". These data are compared to similar data obtained earlier from a molybdenum (Mo) foil. We previously obtained exposure rate data from a 7.1-hour irradiation of a foil (0.0254 cm-thick) of Mo by a beam of $^{18}O^{8+}$ ions (52 enA) having energy of 100 MeV per nucleon. These data were presented in last year's annual report [1].

A tungsten foil, having a thickness of 0.0254 cm, was placed in the target chamber of the NSCL's A1200 beam analysis system, and was irradiated for 61 hours by a beam of $^{18}O^{8+}$ ions having 80 MeV per nucleon. Its thickness was chosen to be comparable to that planned for the deflector septum. The average beam current of the $8^+$ ions was 102 enA, as measured by a Faraday cup placed directly behind the foil.

After irradiation, exposure-rate measurements were made as the foil "cooled", using a Victoreen model 450B ionization chamber [2]. The data were ported to a computer using the ionization chamber's infrared communications output port. The measured exposure rates, in units of milliRoentgens per hour, are shown in Figure 1. The "Beta+Gamma" measurements were made with the ionization chamber's plastic "beta window" open, and the "Gamma" measurements were made with the window closed. The distances used, 7 cm and 30 cm, are measured from the target to the center of the ion chamber volume. The data at 7 cm represent a near-contact measurement. We note that the Mo measurements were made at 7 cm only. And, only "Beta + Gamma" data were collected but for one data point, which showed the ratio of the exposure rates, "Beta+Gamma" to "Gamma", to be 3.1.

The exposure-rate data were analyzed using equations developed [3] to describe the radioactive cooling of accelerator beam- irradiated materials. The Mo data were analyzed using the equation

$$D(t) = D_0 \ln\left(\frac{T+t}{t}\right),$$

where $T$ is the irradiation time, and $t$ is the "cooling" time. $D_0$ depends upon incident beam flux, target thickness, beam energy, cross sections, etc. The numerical value of $D_0$ obtained by fitting the Mo data is 2.35, to give D(t) units of Roentgens per hour.

The W data, labeled as "BetaGamma-7cm", were analyzed using

$$D(t) = D_0\left[t^{-0.4} - (T+t)^{-0.4}\right],$$

suggested by Sullivan [3] as the most suitable equation for heavy elements. The value of $D_0$ obtained from the fitting the W data is 29.3, to give D(t) units of Roentgens/hr.

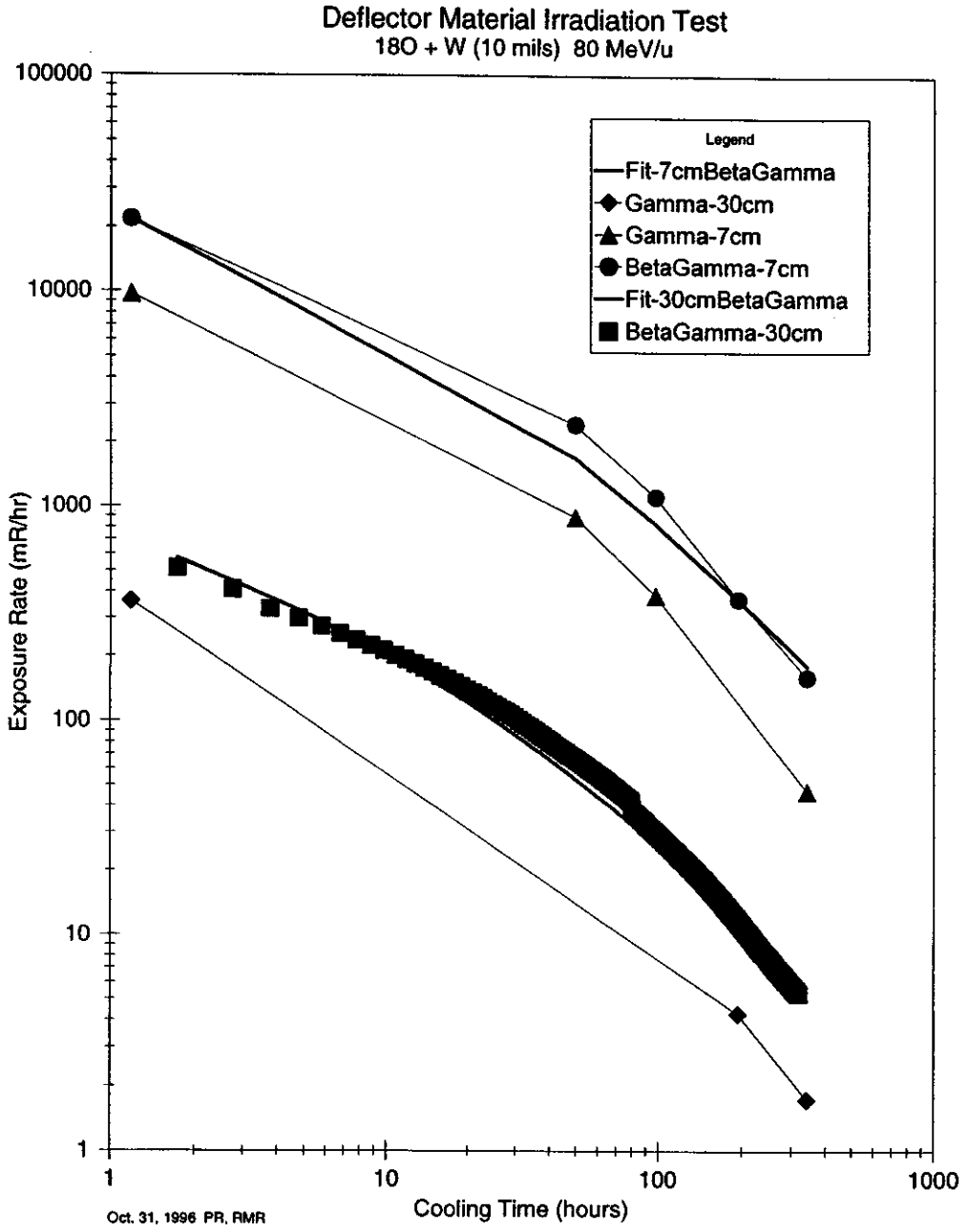


Figure 1: Exposure rates, in milliRoentgens per hour, are shown as a function of time after the irradiation of a 0.0254 cm-thick tungsten foil by a $^{18}O^{8+}$ ion beam (102 enA), having an energy of 80 MeV per nucleon. Data were taken at 7 cm and 30 cm. At each distance, data were taken both with the "beta window" open ("Beta+Gamma"), and with this window closed ("Gamma"). The heavy solid lines are fits of the data, using equations suggested by Sullivan [3], as described in the text.

These equations may be used to predict, for comparison purposes, the expected exposure rates from the two materials, assuming an irradiation time of 100 hours with identical beam conditions, and a cooling time of 1 hour. (The exposure rate calculated using the equation for the Mo data was doubled to account for the factor-of-two difference in beam currents. We ignored the 20% difference in beam energies.) The exposure rate, at 7 cm, is then predicted to be 22 Roentgens/hour for Mo, and 25 Roentgens/hour for W. The predicted exposure rates from Mo and W are similar.

Figure 1 also shows that the cooling time to reach one-tenth the value measured at one hour, is about 50 hours for W. It is about 22 hours for Mo [1].

After obtaining the cooling data, we measured the gamma ray spectrum from the W foil, to identify the long-lived isotopes. The spectrum is complex, with the major full-energy peaks having energies below one MeV. The identified major activities are from 172Lu (7d) and 175Hf (70d). 169Yb (31d) and possibly 177mHf (161d) are also produced.

In summary, the exposure rates from Mo and W deflector septa are predicted to be similar, but the cooling time of W is about twice that of Mo. However, the significantly higher melting temperature of a tungsten septum should minimize the production of volatile activity. After the deflector is removed by remote handling, tungsten's longer cooling time should become an issue only for its off-line repair.

## References


1. NSCL Annual Report for 1995, page 167.
2. The exposure rates from the molybdenum foil were measured using a Victoreen model 470A ionization chamber. Sullivan, "A Guide to Radiation and Radioactivity Levels Near High Energy Particle Accelerators", Nuclear Technology Publishing, Ashford, Kent, England, 1992.
3. Sullivan, "A Guide to Radiation and Radioactivity Levels Near High Energy Particle Accelerators", Nuclear Technology Publishing, Ashford, Kent, England, 1992.

# DESIGN AND SIMULATION STUDIES OF A ONE-TENTH SCALE FINAL FOCUS SYSTEM FOR HEAVY ION FUSION

X. Wu, R.C. York, A. Faltens[a], D. Judd[a], E. Lee[a], and Enrique Henestroza[b]

**Abstract**

A scaled test of a final focus lattice for Heavy Ion Fusion (HIF) is planned at LBNL. The test parameters have been set by scaling the length dimensions of the envelope equation by one tenth while maintaining the generalized perveance. The values to be scaled were taken, in large part, to be those of the HIBALL-II final focus system [1]. The tenth-scale test will focus a 120 keV $Cs^+$ beam to a radial spot size of 0.25 mm. Tracking studies of the tenth-scale system have been performed using a version of COSY INFINITY [2] modified to include a linear space charge force. A description of the planned experimental system, the beam parameters, and simulation results are presented.

**Introduction**

The HIBALL-II parameters were chosen for scaling since it represents one of the more comprehensive designs of a final focus system for heavy ion fusion. The HIBALL-II final focus system specifies a 10 GeV, 1.25 kA, $Bi^+$ beam. The beam emittance at the entrance to the final focus system was assumed to be 30 p mm-mrad with a momentum spread $\Delta p/p$ of $\pm 1\%$. Under these conditions, simulations predict a radial beam spot size of 3.5 mm at the final target position. The HIBALL-II lattice consists of two magnetic quadrupole triplets between which are two dipoles. (Note that the dipole elements are not significant relative to the transverse optics [~3° each], and were not included in this analysis.) Shown in Figure 1 are the HIBALL-II lattice and the beam envelopes predicted with a modified version of COSY INFINITY.

The beam envelope equation for a uniform, isolated beam of elliptical cross-section with semi-major and semi-minor axes of a and b respectively, and a beam emittance of e is given by:

$$\frac{d^2X}{dz^2} = -\frac{B'X}{B\rho} + \frac{\varepsilon^2}{X^3} + \frac{2K}{a(a+b)}$$

where X is the physical size of the beam envelope and K is the generalized perveance given by:

$$K = \frac{I}{I_0}\frac{2}{(\beta\gamma)^3} \text{ with } I_0 = 31\frac{A}{Z}\times 10^6 (\text{A}) .$$

Table 1. Tenth-Scale Final Focus Experiment beam parameters.

| Ion | $Cs^+$ |
|---|---|
| Energy | 120 keV |
| Beam Current | 63 mA |
| K | $1.13 \times 10^{-5}$ |
| Emittance | 3.0 p mm mrad |
| Momentum Spread | ±0.2% |
| Final Radial Beam Size | 0.25 mm |

Following the philosophy of scaling the length dimensions of the beam envelope equation by a factor of 0.1 while maintaining the generalized perveance K, the HIBALL-II parameters result in those given in Table 1 for the tenth-scale final focus experiment [3]. (Note that the momentum spread does not result from scaling, but rather from specific experimental test issues.)

**Code Development**

COSY INFINITY is a beam physics code, which uses differential algebraic (DA) methods to provide systematic calculations of particle trajectories resulting from passage through arbitrary optical elements. Since COSY INFINITY allows the computation of dependencies on system parameters and has the ability to compute and use high-order maps, it was considered an appropriate tool for the analysis of the final focus system. However, the generally available version of COSY INFINITY does not have a provision for the inclusion of the space charge force. The initial effort was to include a simple (linear) space charge force in COSY INFINITY.

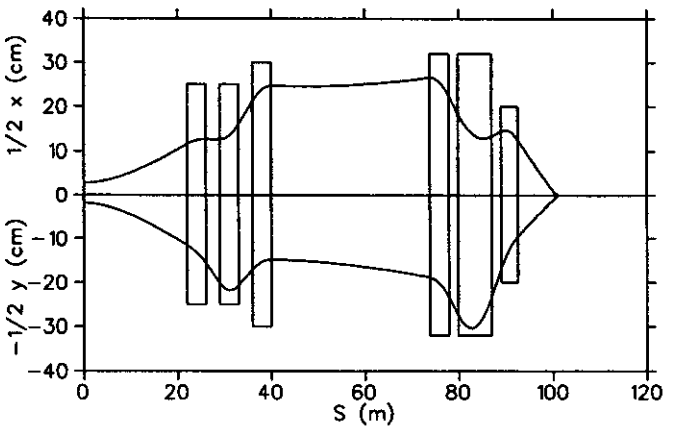


Figure 1. Lattice and beam envelopes of HIBALL-II.

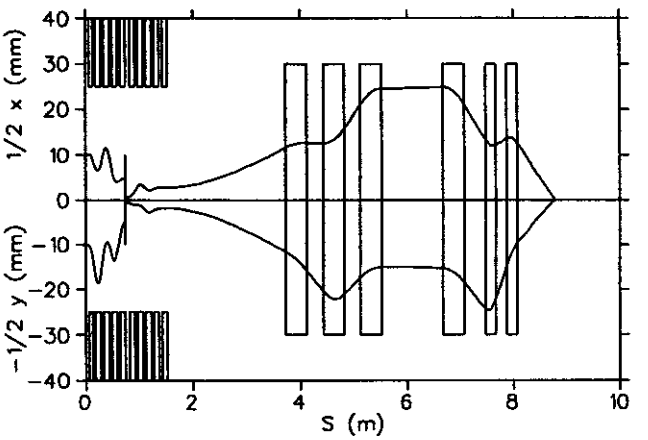


Figure 2. Lattice and beam envelopes of the Tenth-scale Final Focus experiment system.

The implemented space charge model assumes a uniform, isolated beam of elliptical cross-section with semi-major and semi-minor axes of a and b respectively, beam current I, and beam Lorentz factors $\beta$ and $\gamma$.

The combined electric and magnetic fields generated by the beam space charge distribution acting on a particle at transverse position (x,y) are given by:

$$E_x = 2F\frac{I}{\beta\gamma^2}\frac{x}{a(a+b)}\ ,\ E_y = 2F\frac{I}{\beta\gamma^2}\frac{y}{b(b+a)}$$

where:

$$F = \frac{1}{2\pi\varepsilon_0 c}.$$

The potential is then given by:

$$\Phi(x,y) = -F\frac{I}{\beta\gamma^2}\left(\frac{x}{a(a+b)} + \frac{y}{b(a+b)}\right).$$

This space charge induced potential $\Phi$ is used in the modified version of COSY INFINITY to calculate the transfer matrices and maps.

**Tenth-scale final focus experiment system design**

The tenth-scale final focus experiment system will consist of a gun module, a matching section, and the tenth-scale final focus magnetic quadrupole lattice. Figure 2 shows the system configuration of the tenth-scale final focus experiment and the beam envelopes predicted with the modified COSY INFINITY.

The gun module consists of the LBNL 120 keV $Cs^+$ gun and a lattice of five electrostatic quadrupoles followed by a circular aperture. The gun parameters provide for a 6.3 μA beam with an emittance 30 π mm-mrad. To create the beam required for the final focus experiment (63 μA in 30 π mm-mrad), five electrostatic quadrupoles will be used to focus the source image (10 mm radius) to a spot 5 mm in radius at the position of an emittance truncation aperture plate. The emittance truncation aperture will be a circular hole of 0.5 mm in radius. Therefore, the beam current and emittance will be truncated by a factor of 0.01 and 0.1 respectively, providing a beam of 63 mA in 3.0 π mm-mrad.

Following the aperture plate, an additional five electrostatic quadrupoles will be used to match the phase space of the truncated beam to that required for the tenth-scaled final focus lattice. Note that the electrostatic quadrupoles were modeled as hard-edged with the pole voltages symmetric about ground. (Adjacent poles were assumed to have equal and opposite voltages.)

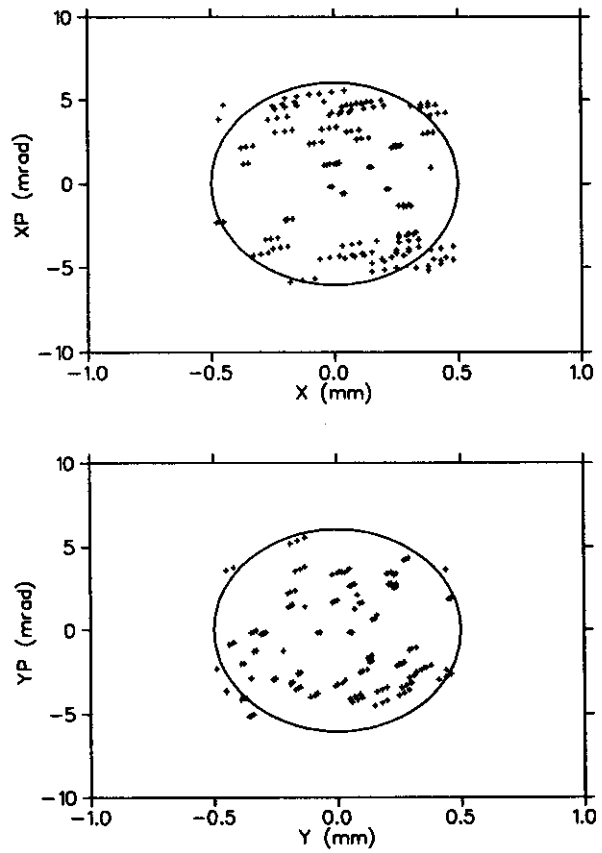


Figure 3. Transverse phase space of surviving particles for the gun to aperture plate tracking.

The tenth-scale final focus magnetic quadrupole lattice will use two magnetic quadrupole triplets to focus the 120 keV $Cs^+$ beam to a radial spot size of 0.25 mm at the target position. The length dimensions and quadrupole settings of the module have been modified slightly from the scaled values of HIBALL-II lattice to reduce the number of quadrupole types required. In addition, the drift space between triplets has been reduced to bring the overall length to 8 m.

**Hardware requirements**

A total of 10 electrostatic quadrupoles are required to match the beam phase space from the gun to that required for the tenth-scaled final focus module. The maximum voltage required is 10 kV with a

radial aperture of 2.5 cm. The first quadrupole following the gun has an effective length of 0.0762 m with the remainder having an effective length of 0.1016 m. The electrostatic quadrupoles as well as the 120 keV $Cs^+$ gun have been constructed and successfully operated at LBNL.

For the tenth-scaled final focus module, a total of six of magnetic quadrupoles with a radial aperture of 3 cm and an integrated strength of 2.3 $m^{-1}$ are required for the two triplets. Four of the quadrupoles will have an effective length of 0.4 m and a maximum pole tip field of 1.0 kG. The other two will have an effective length of 0.2 m and maximum pole tip field of 2.0 kG. The quadrupoles are located within existing vacuum tanks and powered with nominal 1.0 ms half-sine, pulsed waveforms. As such, they are easy to modify or reposition, and other configurations could be tried.

**Simulation studies**

The system was evaluated by particle tracking using a $5^{th}$ order map generated by the modified COSY INFINITY. Due to the large intensity reduction (0.01) at the emittance truncation aperture, the tracking was done in two steps; from the gun to the emittance truncation aperture and from the plate to the final target.

For the gun to aperture plate tracking, ten random seeds were used to populate 4,000 particles within an initial transverse phase space of 30 p mm-mrad for each of three momentum values ($\Delta p/p = 0$ and $\pm 0.2\%$) giving 12,000 particles. Of these 12,000 particles, 165 particles shown in Figure 3 fall within the phase space defined by the 0.5 mm radial aperture. The number of surviving particles (165) is statistically consistent with that predicted by the 0.01 reduction in beam current (120 particles).

For the emittance aperture to final target tracking, 400 particles within an initial beam emittance of 3.0 $\pi$ mm were tracked for each of three momentum values ($\Delta p/p = 0$ and $\pm 0.2$ %) giving 1,200 particles. Figure 4 shows the phase space of these particles at the target position. The real space area at the target position is 0.056 p $mm^2$ for the case of $\Delta p/p=0$ and 0.069 $\pi$ $mm^2$ including particles with momenta of $\Delta p/p = \pm 0.2$ %. The final beam spot area at the target position as function of momenta ($\Delta p/p$) is given in Figure 5. For the tenth-scale final focus experiment lattice, the tracking results indicate that the chromatic effects do not generate any significant increase in the final beam spot size, and therefore, higher-order correction will not be necessary.

**Summary**

The Tenth-scale Final Focus design evaluations predict that this test will provide a cost-effective, experimental basis for future full-scale design evaluations.

a. University of California, Berkeley, CA 95616
b. University of California, Davis, CA 95616

References

1. Wollnik, "HIBALL-II, An Improved Heavy Ion Beam Driven Fusion Reactor Study", KfK-3840, Kernforschungszentrum Karlsruhe, 1985.
2. Berz, "User's Guide and Reference Manual for COSY INFINITY", MSUCL-977, Michigan State University, 1995.
3. Lee, et. al. "Workshop on Scaled Final Focus Experiments", HIFAN-831, LBNL, 1996.

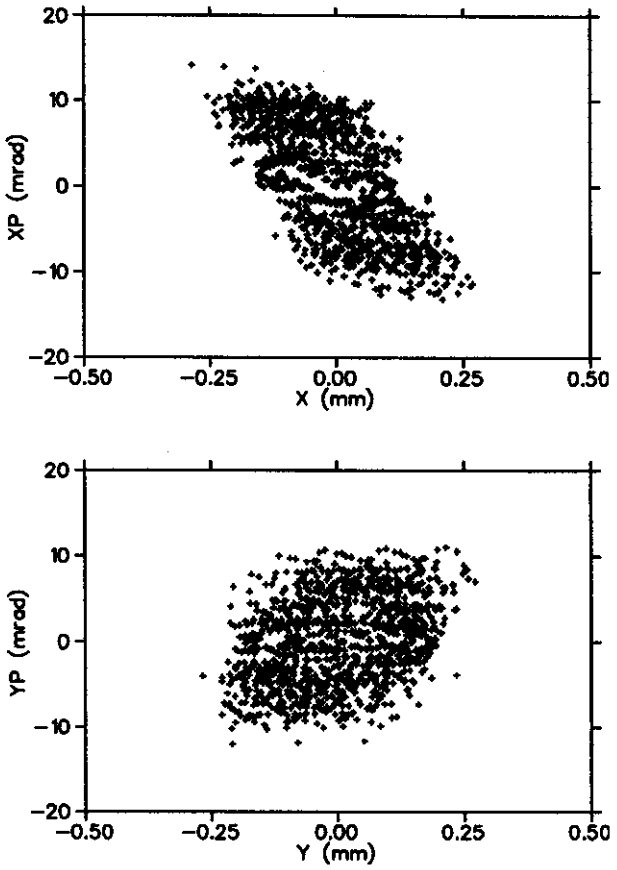


Figure 4. Transverse phase space for particles tracked from the aperture plate to the final target position.

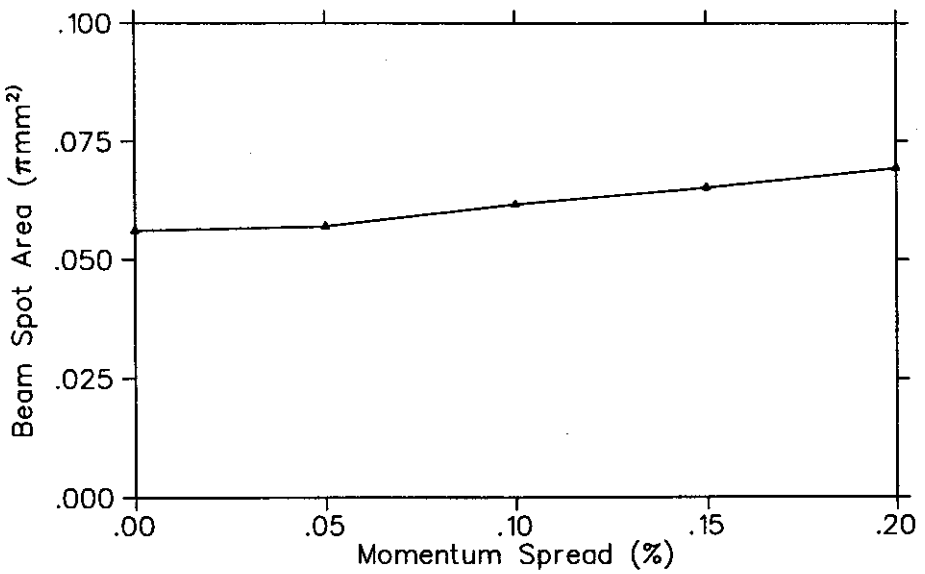


Figure 5. The final beam spot area at the target position as a function of momentum spread.

# DEVELOPMENT OF A $\beta$-NMR SYSTEM FOR THE DETERMINATION OF GROUND STATE MOMENTS OF EXOTIC NUCLEI

P.F. Mantica, R.W. Ibbotson, D. W. Anthony, M. Fauerbach, D.J. Morrissey, C.F. Powell, J. Rikovska,[a,b] M. Steiner, N.J. Stone,[a] and W.B. Walters[b]

Ground state magnetic dipole and electric quadrupole moments provide important information on the extent to which single-particle and/or collective features dominate the low energy structure of nuclei. Such measurements, however, are difficult for nuclei far off the line of stability due to low production cross sections and relatively short ($T_{1/2} < 1$ sec) half-lives. The pioneering experiments by Asahi *et al.* [1], in which they measured the polarization of secondary fragments produced at small angles to the central beam axis by intermediate-energy, heavy-ion reactions, offer a unique opportunity to measure ground state moments for a variety of light, exotic nuclei. The $\beta$-NMR technique can be applied to measure the nuclear hyperfine splitting resonance curve corresponding to the appropriate nuclear moment, where, for the case of a dipole interaction only in an applied magnetic field $B$, the peak in the resonance curve (given as the Larmour frequency, $\nu_L$) is directly related to the nuclear $g$ factor through the relation $h\nu_L = gB$.

We have developed a $\beta$-NMR system at the NSCL that is similar in many respects to that described by Asahi *et al.* [2]. The system resides between the pole faces of a large dipole magnet (pole gap of 10.2 cm), which provides the nuclear Zeeman splitting and the directional holding field for the spin-polarized secondary beams. The detectors consist of two $\beta$ telescopes, located at 0° and 180° with respect to the direction of the holding field of the dipole magnet. The telescopes are each composed of a 4.4 cm × 4.4 cm × 3 mm thick $\Delta E$ plastic scintillator and a 5.1 cm × 5.1 cm × 25 mm thick total energy plastic scintillator. Each scintillator detector is coupled to a long (> 56 cm) acrylic light guide to place the photomultiplier tube of each telescope element beyond the fringe field of the dipole magnet. The telescopes are placed 9 mm from the point of secondary beam implantation, and cover approximately 33% of the $4\pi$ solid angle. A schematic drawing of the $\beta$-NMR system is shown in Figure 1.

A catcher foil was mounted between the two $\beta$ telescopes to collect the secondary fragments, and tilted at an angle of 45° relative to the direction of the magnetic holding field. Surrounding the catcher foil is a set of radiofrequency (RF) coils, which provide the oscillating magnetic field for the resonance measurements. The RF coils are two 30-turn loops (diameter 2.3 cm) of 28 AWG magnet wire, arranged in a Helmholtz-like configuration, with a separation distance of 3.0 cm and a coil inductance of 77 $\mu$H. The RF signal is provided by a Hewlett Packard HP 33120A Function Generator/Arbitrary Waveform Generator and is amplified using an EIN Model 406L RF Power Amplifier. The RF coils are configured as part of an $RCL$ circuit, which also included a 50 $\Omega$ resistor and a variable capacitor to provide the maximum alternating magnetic field by matching the impedance of the $RCL$ circuit to the output impedance (50 $\Omega$) of the RF source. The strength of the RF field is monitored continuously by measuring the voltage drop across the 50$\Omega$ resistor of the $RCL$ circuit using a Pomona Model 6106 Micro-$LC$ RF detector probe.

To test the proper operation of the $\beta$-NMR system, and also to confirm the observed polarization of fragments following intermediate-energy heavy-ion reactions, we have measured the resonance curve for $^{12}$B ($T_{1/2}$ = 20 ms, $I^\pi = 1^+$, $Q_\beta$ = 13 MeV) produced in the fragmentation of a primary beam of $^{18}$O at 80 MeV/A incident on a 216 mg/cm$^2$ $^{93}$Nb target. The secondary fragments were selected by the A1200 fragment separator. Two steering magnets located upstream of the A1200 target position allowed the collection of fragments at +2.5° relative to the primary beam axis. The full angular acceptance of

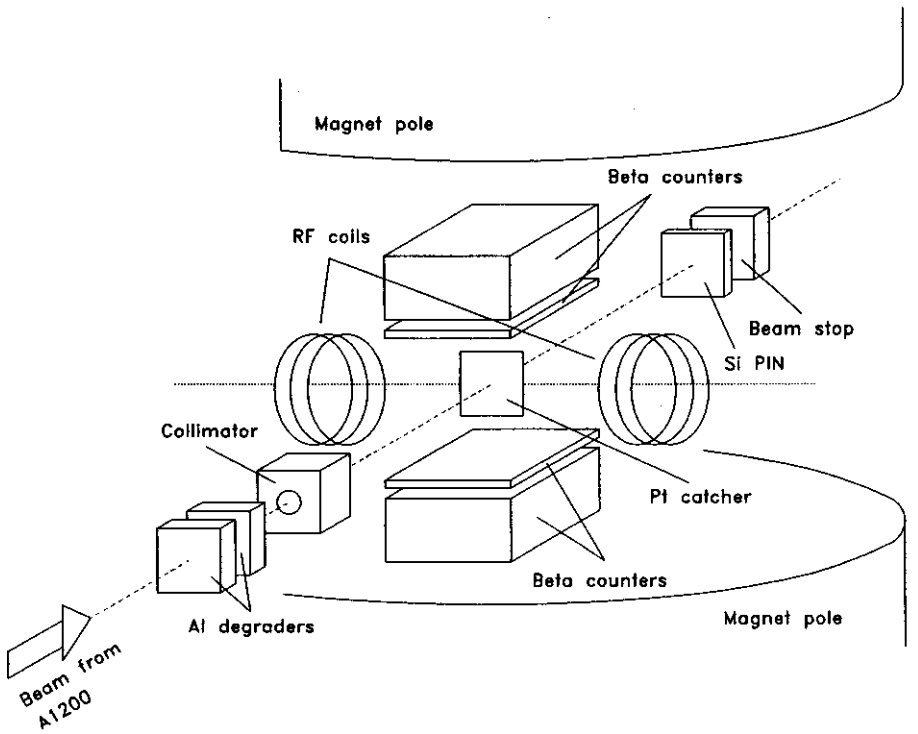


Figure 1: Schematic of the $\beta$-NMR system at the NSCL.

fragments in the deflection plane at the target position was approximately 1°. Fragments were also accepted within 1% of the chosen central momentum of the A1200 as defined by momentum slits placed at the first momentum-dispersed image of the device. The identification of $^{12}$B fragments was accomplished at the A1200 focal plane and the $\beta$-NMR endstation using the energy loss of the fragments measured in a 300 $\mu$m Si PIN detector and the fragment time-of-flight (TOF) referenced to the K1200 Cyclotron radiofrequency.

Data acquisition for the $^{12}$B resonance measurement required pulsing of the K1200 cyclotron beam [3]. The time sequence was controlled by the data acquisition computer. The implantation time (beam on) was chosen to be 20 ms and the data collection time (beam off) was 40 ms. During the beam-on cycles, the 35 MeV/nucleon $^{12}$B fragments were energy degraded to $\approx$ 13 MeV/nucleon using Al foils, collimated, and implanted into a 250 $\mu$m thick Pt catcher foil, which was annealed for 10 h at 630° C in air. $\beta$ particles which produced signals above threshold in both elements of either $\beta$ telescope were recorded in the event stream during the beam-off cycles only. On alternating beam-off cycles, a frequency-modulated (FM) RF signal was introduced to the implanted sample for the duration of the beam-off period. The ratio of the counting rates in the 0° and 180° $\beta$ telescopes for both RF-on and RF-off conditions

$$R = \frac{(\mathrm{Up/Down})_{\mathrm{RF-on}}}{(\mathrm{Up/Down})_{\mathrm{RF-off}}} \tag{1}$$

is the observed NMR effect, and is related to the magnitude of the fragment polarization.

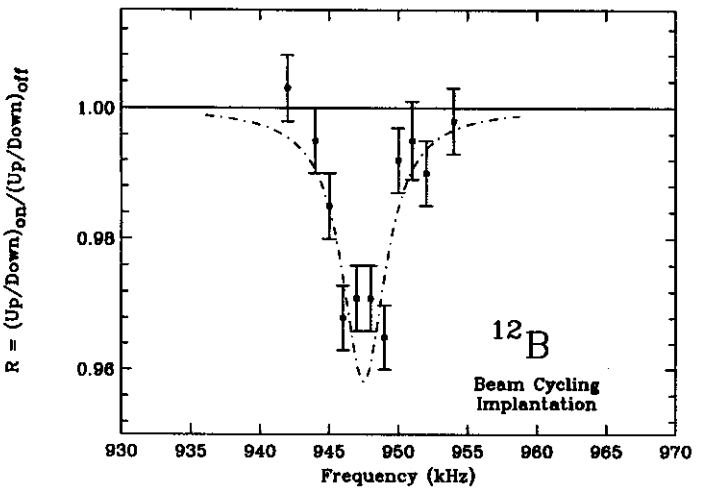


Figure 2: Resonance curve for $^{12}$B using multiple AFP and beam cycling. The frequency modulation was ± 2 kHz. The dot-dashed line is a Lorentzian fit to the data, which resulted in a peak centroid of 947.5 kHz and a linewidth of 2 kHz.

The resonance curve measured for polarized $^{12}$B fragments is shown in Figure 2. For this resonance, the applied magnetic field was 0.124 T. The RF signal was frequency modulated using a triangle waveform with a deviation of ± 2 kHz from the central frequency at a rate of 500 Hz. The best fit to the data using a Lorentzian peak shape required a peak centroid of 947.5 kHz and a width of 2 kHz. From the peak centroid, we deduce a value of $1.003(1)\mu_N$ for the ground state magnetic dipole moment of $^{12}$B, which agrees well with the adopted value [4] of $+1.00306(^{+15}_{-14})\mu_N$.

We chose to use a "multiple" adiabatic fast passage (AFP) technique for NMR as opposed to the single-pass AFP technique [5] in these initial experiments as we were interested in testing an alternative data acquisition method for future $\beta$-NMR measurements. In the multiple AFP technique, the FM signal will cause multiple spin-flips of the polarized nuclear state if the resonance falls within the FM band and if the modulation rate is significantly faster than the decay half-life and spin-lattice relaxation time. The net effect of the multiple AFP for a particular nucleus will depend on where the resonance frequency for that nucleus occurs with respect to the FM frequency range. This is shown schematically in Figure 3. Should the resonance occur at the center of the frequency sweep (position A), then the successive spin flips cause the average spin polarization of the nucleus to be reduced to zero with complete destruction of the $\beta$ asymmetry. When the nuclear resonance is at frequency B, towards an extremum of the frequency range, two situations can occur as the intervals between successive occurences of such a frequency are unequal (see Figure 3). If the initial polarized spin (defined here as spin UP) is produced during the longer time interval, two spin flips will occur in rapid succession, resulting in only a small reduction in the average $\beta$ asymmetry. If, however, the initial production occurs in the shorter time interval, the spin will spend most time DOWN, with consequent average inversion of the asymmetry. A weighted sum of the two possibilities for frequency B will result in a net decrease in the asymmetry, i.e. a net resonance signal. Thus all nuclei having resonant frequencies within the FM sweep range contribute to the total observed resonance signal.

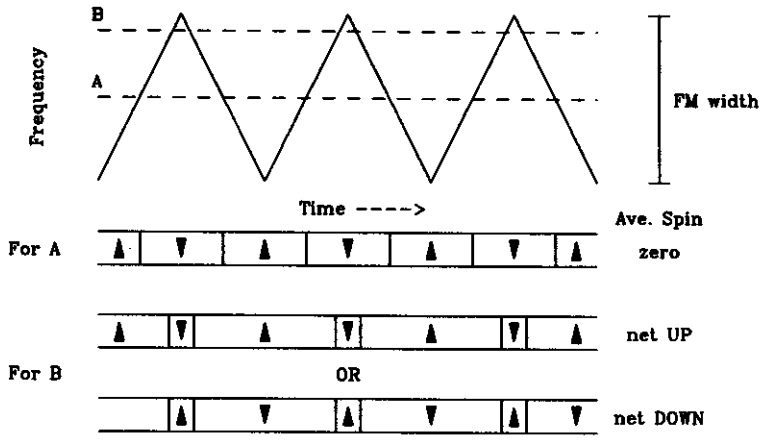


Figure 3: Schematic of the effect of mulitple AFP on the spin of a polarized system. The frequency modulation is in the form of a triangle wave, and of interest is the effective spin of the system at positions corresponding to the center of the frequency sweep (position A) and near the extremes of the frequency sweep (position B). The filled arrows indicate the direction of the spin of the polarized ensemble. Details of the multiple AFP method are discussed in the text.

By applying the multiple AFP technique, it was then possible to collect a continuous sample of $^{12}$B fragments for a given run with a frequency-modulated RF signal constantly applied to the implanted sample. Normalization of the NMR data was then accomplished by continuously collecting $^{12}$B fragments in a second run, this time with no RF signal applied to the sample. The resonance curve obtained for $^{12}$B fragments using multiple AFP and continuous implantation is shown in Figure 4. Again, the goal of this measurement was not to obtain the best precision nor the best resonance, but to confirm that a resonance measurement is possible using this new technique. The only difference in the experimental conditions for this resonance curve and the resonance curve determined for $^{12}$B using multiple AFP and beam cycling was the modulation width of the RF signal, which for continuous implanation was $\pm$ 10 kHz. This larger frequency modulation will lead to a broader resonance peak than that observed in Figure 2, as the asymmetry will be averaged over a wider frequency range. This is reflected in the fit to this data which, when using a Lorentzian peak shape, resulted in a peak centroid of 947 kHz and a linewidth of 7 kHz. The magnitude of the NMR effect for the continuously implanted $^{12}$B sample is not significantly different from that measured using the more conventional beam-on/beam-off data acquisition mode. This result suggests that the polarization of the $^{12}$B fragments is not affected by the application of an RF field during fragment implantation.

The multiple AFP technique with continuous implantation is expected to provide more efficient data collection for long-lived species. However, it may be inferior to techniques involving beam pulsing in dealing with time-dependent errors. The multiple AFP technique may not be as sensitive to small fragment polarization as single-pass AFP with beam-on/beam-off acquisition. When considering the critical role spin-lattice relaxation plays in determining the feasibility of any polarization measurement [5], techniques involving continuous implantation should be favored. Whereas data are only collected

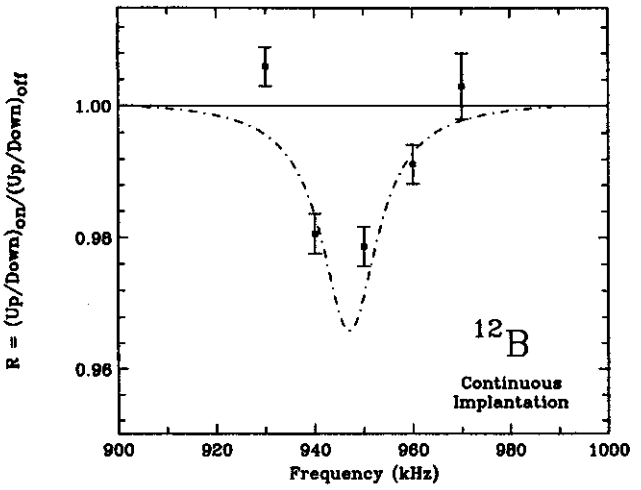


Figure 4: Resonance curve for $^{12}$B using multiple AFP and continuous implantation. The frequency modulation employed was ± 10 kHz. The dot-dashed line is a Lorentzian fit to the data, which resulted in a peak centroid of 947 kHz and a linewidth of 7 kHz.

after a fixed beam-on period to allow for sample implanation during beam pulsing, all times following implantation are included when employing the multiple AFP and continuous implantation.

a. Department of Physics, Oxford University, Oxford OX1 3PU, United Kingdom.
b. Department of Chemistry and Biochemistry, University of Maryland, College Park, MD 20742.

## References

1. K. Asahi *et al.*, Phys. Lett. B251, 488 (1990).
2. K. Asahi *et al.*, Nucl. Instr. and Methods Phys. Res. 220, 389 (1984).
3. D. Mikolas *et al.*, Phys. Rev. C37 766 (1988).
4. P. Raghavan, At. Data Nucl. Data Tables 42, 189-291 (1989).
5. A. Abragam, *The Principle of Nuclear Magnetism* (Clarendon, Oxford, 1961).

# CAN SPECTRAL ARTEFACTS BE THE SOURCE OF MANY SUPERDEFORMED BANDS?

C.V. Hampton, W. A. Olivier, Wm. C. McHarris

The surprising results of the application of the Segmented Fast Fourier Transform (FFT) technique on published Superdeformed (SD) data show an unusual phase shift that we believe will have significant impact on the search for SD bands.

For the past ten years, researchers have been searching for patterns of peaks in $\gamma$ ray data that they believe represent, what has been termed, superdeformed and hyperdeformed bands in nuclei. In this time, 161 superdeformed bands have been reported [1] in over 80 nuclei, many of which are multiple bands within the same nucleus or identical bands among neighboring nuclei that were established from the same experimental reaction. In order to facilitate the search process, computer algorithms were designed to locate SD within complex data arrays. [2,3] The methodology is based on logical tests of multiple detector coincidences [4] found in the data set and results in construction of a series of patterns that have SD potential. Run time for one of these computer experiments can be between 24 hours to 10 days.

The Segmented FFT technique that we reported in last year's annual report[5] is unique in that it does not generate the SD band but rather, it investigates the inherent frequencies of the spectrum in order to find a match with a potential SD band. The method is very fast and an unlimited number of SD patterns can be searched for. Because of this speed, it has been employed as a tool to investigate published SD band data. The search technique is simple: Conversion of a standard, reference band into frequency space provides a pattern, segments, of which, act as a template to be extracted from the frequency spectrum of the original data set. These frequency segments are then retransformed into energy space. The presence of band frequencies in the data set that match those from the reference band provides useful information in identifying and analyzing the band.

In addition to comparing the data search result with the corresponding result from the standard SD spectrum, the following are necessary for a successful search: Match the standard peak FWHM to that of the data set. SNIP the baseline [6] and crop the channel number range of the data file to match the range of the standard SD band. Use a 4K range for the forward transform algorithm. This allows use of wider segment windows. Use as few segment windows as necessary to locate a recognizable band. If necessary, mask out stray harmonics from other (non SD) peaks by adding in a normalized valley sum from the standard spectrum. Do a dose response and a control search on an unrelated spectrum using the same parameters.

The method was performed on published $^{133}$CE SD band 3 data acquired on a large multi-detector array. [7] Fig 1 shows the results of the search. This technique is sensitive enought to find SD bands within the sum of SD gated spectra (Fig 1a) and also within background spectra (Fig 1b). The surprising part is that the peak centroids in the corresponding search results (Fig 1d and Fig 1e) do not exactly match the corresponding centroids in either the standard spectrum or the difference spectrum (Fig 1c or Fig 1f). There is a slight phase shift in the entire peak, indicating that a compression or expansion of the x-axis has occurred between the gated SD spectrum (Fig 1a) and the background spectrum (Fig 1b).

Methodology was devised to investigate the source of the phase shift. Since calibration fluctuations would be an obvious choice, an unrelated data set acquired on the CSS spectrometer at HRIBF was rebinned in four different ways to simulate minor calibration changes. Regression analysis was performed on data

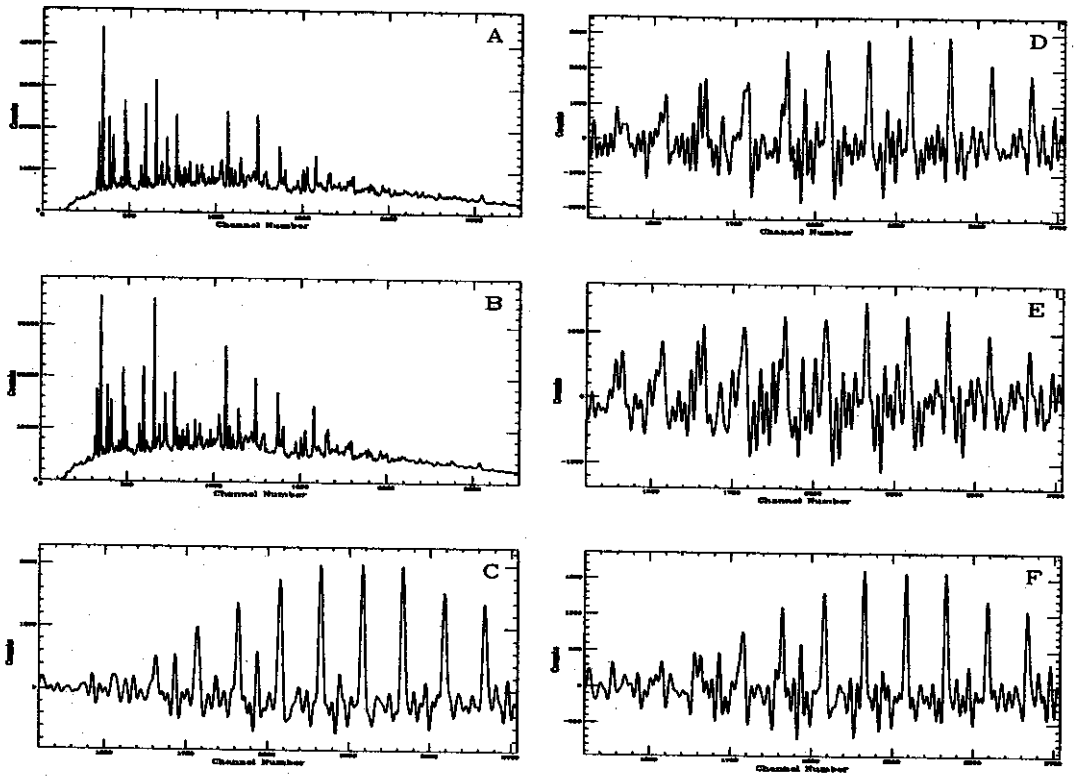


Figure 1: A) Sum of the gated SD peaks. B) Background spectrum. Search results for $^{133}$Ce SD3 in: C) The standard $^{133}$Ce SD3 spectrum. D) Sum of the gated SD peaks. E) Background spectrum. And, F) The difference spectrum formed by subtracting the search results: spectrum E from spectrum D.

points acquired from 20 detectors using $^{133}$Ba, $^{152}$Eu, $^{60}$Co, and $^{88}$Y calibration standards. One test set was a simple linear regression. Another set included four parameters and produced coefficients of $x^0$, $x^1$, $x^2$, $x^3$ or $x^4$. These non-linear terms represent minor fluctuations around a straight line. Since many software programs used to analyze high resolution $\gamma$ ray data only include provisions for two or three coefficients of calibration, two other test sets were included in the study: one included only the first three coefficients from the four parameter test set; the other included only the first two coefficients from the same test set. By comparing spectra from the same detector that differ only by these minor calibration changes, we would be able to observe whether or not spurious, artefact-peaks can be formed during routine data analyses. If these calibration changes were too small to affect the peak energy, then subtracting two test sets would produce an empty set. However, if the calibration changes shifted the peaks out of phase between the test sets, then a subtraction would produce many positive and negative peaks. Fig 1 shows

Table 1: Calibration rebinning experiment:

| | $x^0$ | $x^1$ | $x^2$ | $x^3$ or $x^4$ | Linear Regression |
|---|---|---|---|---|---|
| Test 1 | * | * | * | * | 4 parameter fit / 4 used |
| Test 2 | * | * | * | - | 4 parameter fit / 3 used |
| Test 3 | * | * | - | - | 4 parameter fit / 2 used |
| Test 4 | * | * | | | 2 parameter fit / 2 used |

examples of the results. Many artefact peaks formed during the test comparisons. In fact, none of the 20 detectors produced empty sets. Some, such as the Test 1 minus Test 4 (Test 1m4), would just add to the noise level of the spectrum; however, many have a peak intensity that would be significant, had they been formed in a routine data analysis, such as the background subtraction process. An expansion of the Test 2m3 comparison shows many small peaks of equivalent intensity that are separated by nearly equal distances. Two Phantom SD bands can be observed that are comparable in intensity and spacing to those reported in the A=130 region. This Test 2m3 comparison simulates what would happen if low resolution software were used with data calibrated to three coefficients.

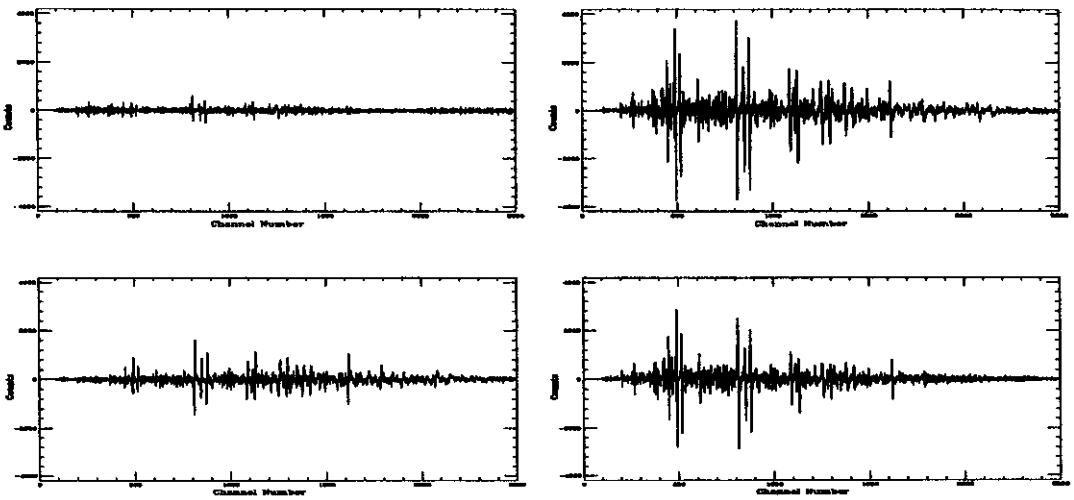

Figure 2: Examples of artefact peaks formed during the test comparisons from the calibration rebinning experiment: clockwise, from the upper left, Test 1m4, Test 2m3, Test 1m2, Test 1m3.

Conclusions:

1) Phantom SD peaks can be generated during data analysis. The calibration experiment shows that peaks with SD spacing and intensities may be formed by any compression or expansion of the x-axis. Some potential sources may be the following:

- Low resolution software (truncation of higher calibration coefficients).
- The use of a background spectrum with a different multiplicity than the gated spectrum.
- The effects of low resolution gain shifting or doppler shifting.
- Linear normalization of all detectors in an array instead of using their non-linear coefficients, also.

2) There may be a need to re-evaluate many SD spectra from this new perspective.

References


1. Singh, B., R.B. Firestone, S.Y. Frank Chu, "Table of Superdeformed Nuclear Bands and Fission Isomers", 2nd Edition, LBL-38004 UC-413, May 1996.
2. J. N. Wilson, *Ph.D. Thesis, University of Liverpool* (1995).
3. D.S. Haslip, et al., Nucl. Instr. and Meth. in Phys. Res.A 345, 534 (1994).
4. C.W. Beausang, et al., Nucl. Instr. and Meth. in Phys. Res.A 364, 560 (1995).
5. C.V. Hampton, W.A. Olivier, Wm.C. McHarris, 1995 NSCL Annual Report, p.274 . Also, presented at the Workshop on Data Analysis, HRIBF, ORNL, February 7-10, 1996 and at the APS/AAPT Meeting, Indianapolis, IN May 2-5, 1996.
6. C.V. Hampton, B. Lian, Wm.C. McHarris, Nucl. Instr. and Meth. in Phys. Res.A 353, 280 (1994).
7. K. Hauschild, et al., Phys.Lett. 353B, 438 (1995).